# Photoinduced Dichroism in Amorphous $As_2Se_3$ Thin Films

A Thesis Submitted to the
College of Graduate Studies and Research
in Partial Fulfillment of the Requirements for the
Degree of Master of Science
in the Department of Electrical and Computer Engineering
University of Saskatchewan
Saskatoon

By

Matthew Kowalyshen

# PERMISSION TO USE

In presenting this thesis in partial fulfillment of the requirements for a Postgraduate degree from the University of Saskatchewan, I agree that the Libraries of this University may make it freely available for inspection. I further agree that permission for copying of this thesis in any manner, in whole or in part, for scholarly purposes may be granted by the professor or professors who supervised my thesis work or, in their absence, by the Head of the Department or the Dean of the College in which my thesis work was done. It is understood that any copying or publication or use of this thesis or parts thereof for financial gain shall not be allowed without my written permission. It is also understood that due recognition shall be given to me and to the University of Saskatchewan in any scholarly use which may be made of any material in my thesis.

Requests for permission to copy or to make other use of material in this thesis in whole or part should be addressed to:

Head of the Department of Electrical and Computer Engineering

57 Campus Drive

University of Saskatchewan

Saskatoon, Canada, S7N 5A9

# ACKNOWLEDGMENTS

I would like to extend my sincerest gratitude towards my supervisor, Dr. S.O. Kasap, and my co-supervisor, Dr. R. Johanson, for their patience, encouragement and leadership throughout the course of this project. I would also like to thank Dan DeForrest for establishing the bulk of the experimental setup which I used on a daily basis. George Belev deserves thanks for not only preparing my samples, but also answering my many questions regarding anything from integrated circuits to nuclear physics. This thesis would not have been possible without the financial support from my supervisor Dr. S.O. Kasap as well as the Electrical Engineering Department at the University of Saskatchewan. Finally, I would like to thank my family and colleagues for their support, encouragement and patience.

# ABSTRACT

The dichroism induced by a polarized beam of near bandgap light was measured in thin films of amorphous $As_2Se_3$. The polarized pump-beam causes a decrease in the absorption coefficient for light polarized in the same direction, and the resulting anisotropy in absorption coefficients is referred to as dichroism. An unpolarized beam of light passing through the sample will be preferentially absorbed in the same direction as the pump-beam polarization direction. That preferential absorption can be measured as a function of time to represent the time dependence of the induced dichroism.

The time dependence of the induced dichroism follows a stretched exponential of the form $A(t) = A_{sat} + (A_{init} - A_{sat})e^{-(t/\tau)^{\beta}}$. Three parameters from the fitting function are of interest; the saturation level $A_{SAT}$, the time constant $\tau$, and the stretching exponent $\beta$. The kinetics of dichroism were extracted from measurements on samples of various thicknesses, samples subjected to various pump-beam intensities, samples doped with small quantities of iodine (0.1%), and for samples in the presence of a DC electric field. It was found that the induced dichroism saturates at a value that depends linearly on sample thickness, but is independent of inducing beam intensity. The time constant ($\tau$) was found to have an inverse relationship with pump-beam intensity and decreases with increasing sample thickness. The stretching exponent $\beta$ has little or no dependence on either intensity or thickness. The addition of iodine (0.1%) increased the time constant ($\tau$) in some but not all cases; meanwhile the DC electric field had no effect on any of the fitting parameters.

Measurement of the kinetics of the induced dichroism in amorphous $As_2Se_3$ can be used to constrain models of the phenomenon in Chalcogenide glasses. The results of the intensity dependence study fit well within the framework of the current theoretical models; however, the iodine doping and electric field measurements do not. The model predicts a decrease in the rate for samples doped with iodine, and those subjected to a transverse electric field; neither effects were observed.

Providing a framework for photoinduced dichroism is important if device level applications are to be realized using the effect. In order for any material to be used in commercially viable applications it needs to be cheap and easy to produce; and it needs to be completely described from an optical and electrical standpoint. A better understanding of photoinduced dichroism in amorphous $As_2Se_3$ may lead to the realization of optical switches, optical memory, polarizers, waveguides, and diffraction gratings.

# Table of Contents

# List of Tables

# List of Figures

# List of Abbreviations

a-$As_2Se_3$..... Amorphous Arsenic Triselenide

a-Se..... Amorphous Selenium

a-Si:H..... Hdrogenated Amorphous Silicon

$As_2Se_3$..... Arsenic Triselenide

$As_2Te_3$..... Arsenic Tritelluride

CB..... Conduction Band

CFO..... Cohen, Fritzsche, Oshinski

CMOS..... Complimentary Metal Oxide Semiconductor

CRN..... Continuous Random Network

DC..... Direct Current

DOS..... Density of States

ESR..... Electron Spin Resonance

EXAFS..... Extended X-ray Absorption Fine Structure

FWHM..... Full Width Half Maximum

GeTe..... Germanium Telluride

$GeS_2$..... Germanium Di-sulfide

GPIB..... General Purpose Interface Bus

HeNe..... Helium Neon

HP..... Horizontal Polarization

IVAP..... Intimate Valence Alternation Pair

LD..... Laser Diode

LED..... Light Emitting Device (Diode)

LIA..... Lock-In Amplifier

LRO..... Long Range Order

PB..... Photobleaching

PBi..... Photoinduced Birefringence

PD..... Photodarkening

PDi..... Photoinduced Dichroism

RF..... Radio Frequency

SEM..... Scanning Electron Microscopy

SRO..... Short Range Order

TEM..... Transmission Electron Microscopy

VAP..... Valence Alternation Pair

VP..... Vertical Polarization

XPS..... X-ray Photoemission Spectroscopy

# Chapter 1 Introduction

## 1.1 Introduction

It was originally believed that amorphous materials could not be semiconductors; however, in the mid-50's Nina A. Goryunova and Boris T. Kolomeits discovered that one of their amorphous compositions exhibited activated conductivity [1]. That discovery led to the study of amorphous semiconductors and their potential for use in device applications. Of the amorphous materials studied, it was the chalcogenide glasses which exhibit the most promising properties. Research on chalcogenide glasses led to the first successful copier based on the photoconductive properties of amorphous selenium [2], sparking significant interest and further research, which eventually led to the realization of a digital flat panel x-ray image detector [3]. Chalcogenide glasses are now studied extensively and used in a wide variety of applications.

Current interest in chalcogenide glasses evolved from their potential in optoelectronics and photonics. There is a need for higher transmission rates and larger bandwidth in integrated circuits as well as communications electronics. A possible solution to the current problem is integrated optics, sometimes referred to as microphotonics [4], which involves the integration of optoelectronic and photonic devices with CMOS electronics. There are several attractive properties and characteristics of chalcogenide glasses that make them ideal for use in integrated optics.

From an application standpoint any material that will be used in commercially available optical devices needs to be cheap and efficient to produce. Typically chalcogenide glasses have low melting and glass transition temperatures; therefore, glass fabrication is relatively inexpensive. Some of the current fabrication methods employed are vacuum vapor deposition, sputtering, and pulsed laser deposition.

Chalcogenide glasses are also characterized by high refractive indices, on the order or 2 to 3 [5], which make them ideal for optical confinement devices such as waveguides and

fiber optic cables. Fiber optic communication currently employs the use of conversion stations where signals are flipped from electronic to optical and vice versa. The ideal situation would involve a completely optical system, where all-optical amplifiers eliminate the need for conventional electronics. A requirement of any material used for fiber optics is not only the high refractive index, but good transparency in the mid to far infrared communications wavelengths as well. Chalcogenide glasses meet both of those criteria [5]. A section of rare-earth doped chalcogenide glass is inserted into the fiber optic cable and the rare-earth ions act as luminescence centers, when optically pumped, creating the all-optical amplifier. An Erbium-doped fiber amplifier has already been commercially available for several years.

Upon illumination with bandgap or sub-bandgap light chalcogenide glasses experience a shift in the optical gap. The effect is known as either photodarkening or photobleaching depending on whether the bandgap has decreased or increased, respectively. Photodarkening is useful for creating waveguides [6] and diffraction gratings [7]; while it also changes the material etch characteristics making it useful as an inorganic photoresist [8]. Photodarkening can also be accompanied by other optical changes as well as structural, mechanical, or chemical changes [9]. These changes have led to some significant developments including rewritable CD's/DVD's as well as possible positioning devices. In the case of rewritable CD's/DVD's, heat generated by non-radiative recombination of photo-exited carriers results in a phase change between the crystalline and amorphous phases [10]. The possibility of positioning devices exists because of the opto-mechanical effect, which is related to the reversible photoinduced anisotropy in the nano-contraction and dilatation of a chalcogenide film induced with polarized light [11]. To date the only materials that have the accuracy of nanometer scale precision are piezoelectric and electrostrictive positioning devices both of which use electric fields for positioning. Chalcogenide glasses could offer a nanometer scale positioning device that can operate in electrostatic sensitive areas.

Perhaps the most interesting of all of the photoinduced phenomena in chalcogenide glasses is photoinduced anisotropy discovered by Zhandov et al. in the mid 1970's [12].

Most glasses are initially isotropic and homogeneous, and should not exhibit birefringence or dichroism; however, anisotropy can be induced in certain glasses by polarized light with photon energy near the bandgap. When an amorphous chalcogenide glass absorbs an intense pump beam of polarized light, the absorption coefficient for light polarized in the same direction as the pump beam is less than for light polarized in the perpendicular direction. Therefore, the sample is said to be anisotropic, or dichroic. Induced dichroism is potentially useful in various photonic devices [13] including optical switches, optical memory, polarizers, waveguides, and diffraction gratings.

Since the time of its discovery a vast amount of research has been devoted to determining the underlying mechanisms responsible for photoinduced anisotropy. Although studies have provided insight into the macroscopic properties of the phenomenon, microscopic mechanisms cannot be controlled directly by experiment; therefore, there is not even basic agreement on how macroscopic anisotropy is related to microscopic changes.

## 1.2 Research Motivation and Objectives

Recent interest in chalcogenide glasses has developed out of a need for increased data transmission rates and bandwidth in communication based electronics. Until now fiber optic cables have been the transmission medium of choice because of their large bandwidth capability that far exceeds any other medium. However, the ideal system would be completely photonic, eliminating the need for an intermediary between conventional electronics and the fiber optic cable. In order to make this a reality, cost efficient optoelectronic and photonic devices that can handle the large potential bandwidth need to be developed.

The goal or purpose of this research is to find high performance materials for optoelectronic and photonic devices that will have a greater level of integration. This would greatly benefit optical networks and potentially lead to an optical computer. Although many advances in research have been made, and there are commercially available devices based on the properties of chalcogenide glasses, there are still

challenges and problems involved creating components in optically integrated form [14]. Specifically; chalcogenide alloys have incompatible thermal characteristics with some substrates [6,15], they lack chemical and mechanical durability [6], some are toxic (tellurium in particular), and the amount of dichroic change between two orthogonal states is low [13] (i.e. a 5% change is regarded as 'giant' photoinduced anisotropy [16]). Despite these drawbacks the numerous unique characteristics of chalcogenide alloys make them very promising materials for optoelectronic and photonic devices.

The research involved in this thesis deals with the photoinduced anisotropy of thin films of near stoichiometric amorphous $As_2Se_3$. The photoinduced anisotropy, or dichroism, was induced using both a Helium Neon laser well as a 658nm laser diode. The time dependence of dichroism follows a stretched exponential function of the form $\exp(-(t/\tau)^{\beta})$. Three parameters from the fitting function are of interest; the saturation level $A_{SAT}$, the time constant $\tau$, and the stretching exponent $\beta$. The most comprehensive studies determined the fitting parameters as a function of pump intensity and thickness. Two materials were studied, a-AsSe, as well as samples doped with small quantities of iodine (0.1%). Also, a setup was developed to measure the effect of an external DC electric field on dichroism.

## 1.3 Thesis Outline

In this thesis the second chapter delivers a basic introduction to amorphous semiconductors and chalcogenide glasses. The chapter first touches on the structure of amorphous materials and explains some of the important similarities and differences between amorphous and crystalline materials. There is a brief explanation of glasses and their structure followed by a discussion of the optical and electrical properties of chalcogenide glasses. The last two sections of the chapter focus on valence alternation pairs (VAP's) and intimate valence alternation pairs (IVAP's), and the preparation techniques involved in creating chalcogenide thin films.

Chapter 3 provides an overview of photoinduced effects in chalcogenide glasses. There is a general introduction to photoinduced changes in chalcogenide glasses followed by several sections discussing each of the changes individually. The distinction between vectoral and scalar photoinduced effects as well as reversible and irreversible changes is made. The last section in the chapter provides descriptions of the currently accepted models for photoinduced changes, specifically photoinduced anisotropy, in chalcogenide glasses.

In Chapter 4 the entire measurement system and measurement procedure is described. The initial descriptions involve light sources used to induce and measure photoinduced anisotropy. That is followed by a complete description of the data acquisition system including signal processing and the computer interface. Lastly, the method used to measure photoinduced linear anisotropy as function of intensity and electric field is described.

Mathematical analysis of the measurement system is the subject of Chapter 5. In this chapter it is shown how photoinduced anisotropy can be derived from measured quantities. The mathematics of the experimental setup are also presented along with the solution for determining the amount of anisotropy from measured results.

Chapter 6 focuses on the results and implications of the measurements that have been made. It begins with a description of the typical procedure used for data analysis. This is followed by a presentation of the experimental data for measurements of photoinduced linear dichroism as a function of intensity, thickness, and electric field. Included are the results for amorphous $As_2Se_3$ and for samples doped with small quantities of iodine.

The thesis is ended with Chapter 7 which presents some general conclusions regarding the work that was the subject of this thesis. Suggestions for future work are also provided.

# Chapter 2 Chalcogenide Thin Films

## 2.1 Introduction

This chapter introduces the concept of an amorphous semiconductor. It describes the structural properties of amorphous materials and how they differ from their crystalline counterparts. Those structural properties lead to various interesting electrical and optical properties which are summarized. The section on amorphous semiconductors is followed by a section focusing on a specific type of amorphous semiconductors which are the chalcogenide glasses. In that section a brief description of chalcogenide materials is given, along with clarification regarding their classification as a glass. Also discussed are valence alternation pairs (VAP's) and intimate valence alternate pairs (IVAP's). Lastly, the preparation techniques used to prepare the samples studied in this thesis are outlined. For further details the reader is referred to Mott and Davis' *Electronic Processes in Non-Crystalline Materials* and Elliott's *Physics of Amorphous Materials* both of which provide an excellent introduction to the physics of amorphous materials [17, 18].

## 2.2 Amorphous Semiconductors

Crystalline solids consist of atoms or molecules arranged in three dimensional arrays, where the structure has well defined symmetry and periodicity. The exact orientation and number of neighbors can be determined from one atom to the next. A representation of the crystalline state is shown in Figure 2-1 (a). It demonstrates the periodic arrangement of atoms or molecules, which extends throughout the whole solid, known as long range order (LRO).

Amorphous solids do not have the long range periodicity of their crystalline counterparts. The amorphous structure, shown in Figure 2-1 (b), instead has disordered bond geometry. Although the structure lacks long range order, the organization of each atom remains well defined because it must fulfill its chemical bonding requirements; therefore, the structure does exhibit what is called short range order (SRO). The SRO applies to distances in the

range from 2 to 5 Å, where there is very little difference between the crystalline and non-crystalline states.

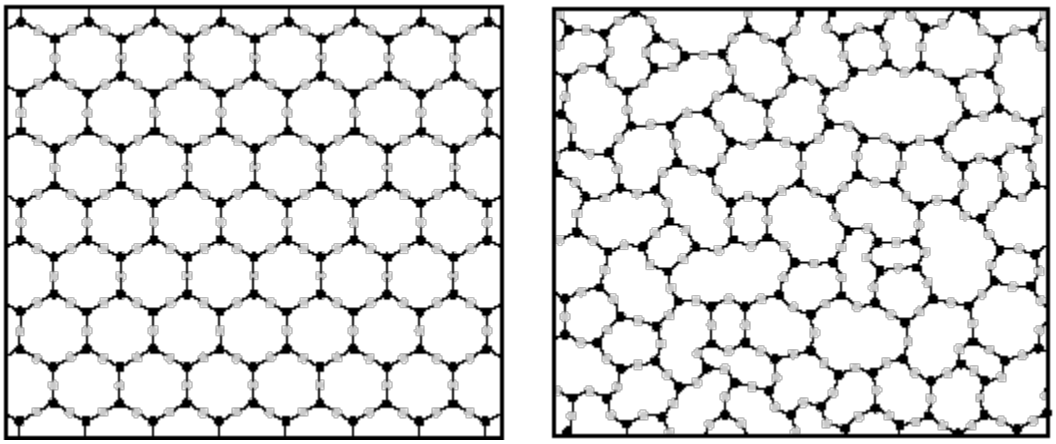

(a) (b)

**Figure 2-1: Two-dimensional diagram of the bonding arrangement in $As_2Se_3$. The diagram (a) shows the crystalline form, and the diagram (b) illustrates the amorphous (or glass) form.**

The bonding involved in amorphous solids can be classified exactly the same as for crystalline solids. There are five major classes: (1) ionic, (2) covalent, (3) metallic, (4) Van der Waals, and (5) hydrogen-bonding. The elements of interest for this thesis are the pnictogens, Group V, and the chalcogens, Group VI, which result in bonding that falls into category 2, covalently bonded solids. The structure of covalently bonded materials is well described by the Continuous Random Network (CRN) model first proposed by Zachariasen [19]. In the CRN model the amorphous structure is created by continually attaching SRO units, where the disorder arises from variations in nearest neighbor bond lengths and bond angles.

A complete structural description of an amorphous solid can be extremely difficult if not impossible to construct. For years the mathematical complexity and lack of long range order long excluded amorphous materials from being considered semiconductors; however, in 1955 Goryunova and Kolomiets discovered that one of their amorphous compositions demonstrated the semiconductor behavior of activated conductivity [1]. From that time on a great deal of research has gone into understanding their properties

and behavior. Although the microscopic structure may not be known, the electronic structure has been investigated heavily and well described.

A description of the electronic structure begins with the case of two atoms brought sufficiently close to each other such that they interact. The interaction will cause a bond to form provided that the overall energy of the combined system is lower than if the two atoms remain isolated. Figure 2-2 shows the potential energy ($E$) of two atoms as a function of the interatomic separation ($r$) between the atoms. The figure displays the net energy of the system, as well as both the attractive energy ($E_A$) and the repulsive energy ($E_R$) which together result in the total energy. As the atoms are brought together from infinity the energy is continually lowered due to the attraction of the electrons and protons dominating the overall energy. It is only when the atoms get very close that the repulsive energy of the electron-electron and proton-proton interactions dominate, causing the total energy to increase. The minimum energy point corresponds to a balance of the attractive and repulsive forces and is referred to as the bond energy. At that minimum energy bonding occurs and the interatomic separation becomes the bond length ($r_0$).

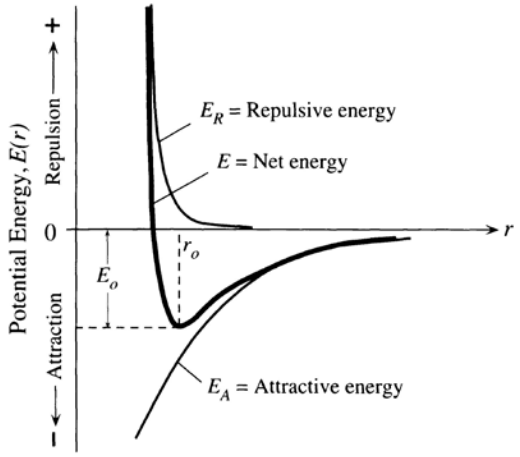


**Figure 2-2: Potential energy, E(r), versus the interatomic separation (r) [20].**

When a bond forms it is a result of the energetically favorable interaction of the outer electrons of each atom. If we consider only a single atom, quantum theory tells us that only a discrete number of states are possible for the electrons in any given atom. These states are grouped into shells which contain a range of allowable energies that an electron can

have. The electrons in the outer most shell are known as the valence electrons and are responsible for bonding between atoms.

The possible energy states in an atom are filled according to selection rules based on the allowable principal, orbital angular momentum, magnetic, and spin magnetic quantum numbers. The four quantum numbers define an electronic state for the electron; however, the Pauli Exclusion Principle prevents any two electrons in an atom from occupying the same state, so the number of electrons and the number of states in each shell become crucial to determining the properties of an atom.

In the case of a chalcogen element the outermost shell contains six of a possible eight electrons. Its configuration, shown in Figure 2-3 (a), results in two lower energy electrons in the s state and four higher energy electrons in the p state. The s states have only one possible value of orbital angular momentum; meanwhile, the p states have three. All electrons have only one of two possible values of spin magnetic quantum number, which correspond to either spin up or spin down. The two paired s-electrons are located closer to the atom in a deep energy state preventing them from participating in bonding. Of the p-electrons, two of them are available to form covalent bonds (coordination number is 2) and the remaining two form what are called a lone pair. The distribution of electrons is shown in Figure 2-3 (b), where we see that the lone pair electrons are at a higher energy level than the other four p-electrons.

If we once again consider the case where two atoms are brought sufficiently close the result is the interaction of the outer electrons. That interaction leads to a shift in the energy states of the atoms, where some states increase in energy, and typically an equal number of states decrease in energy. The states for which there is a reduction in energy to an energetically more favorable state are called bonding states ($\psi$), and the states for which there is an increase in energy to an energetically less favorable state are called anti-bonding states ($\psi^*$). The bonding and anti-bonding states for a chalcogen element are shown in Figure 2-3 (b). The bonding states are always filled by pairs of electrons of opposite spin while

the anti-bonding states are empty. In the case where all of the bonding states are filled the solid is said to be maximally bound.

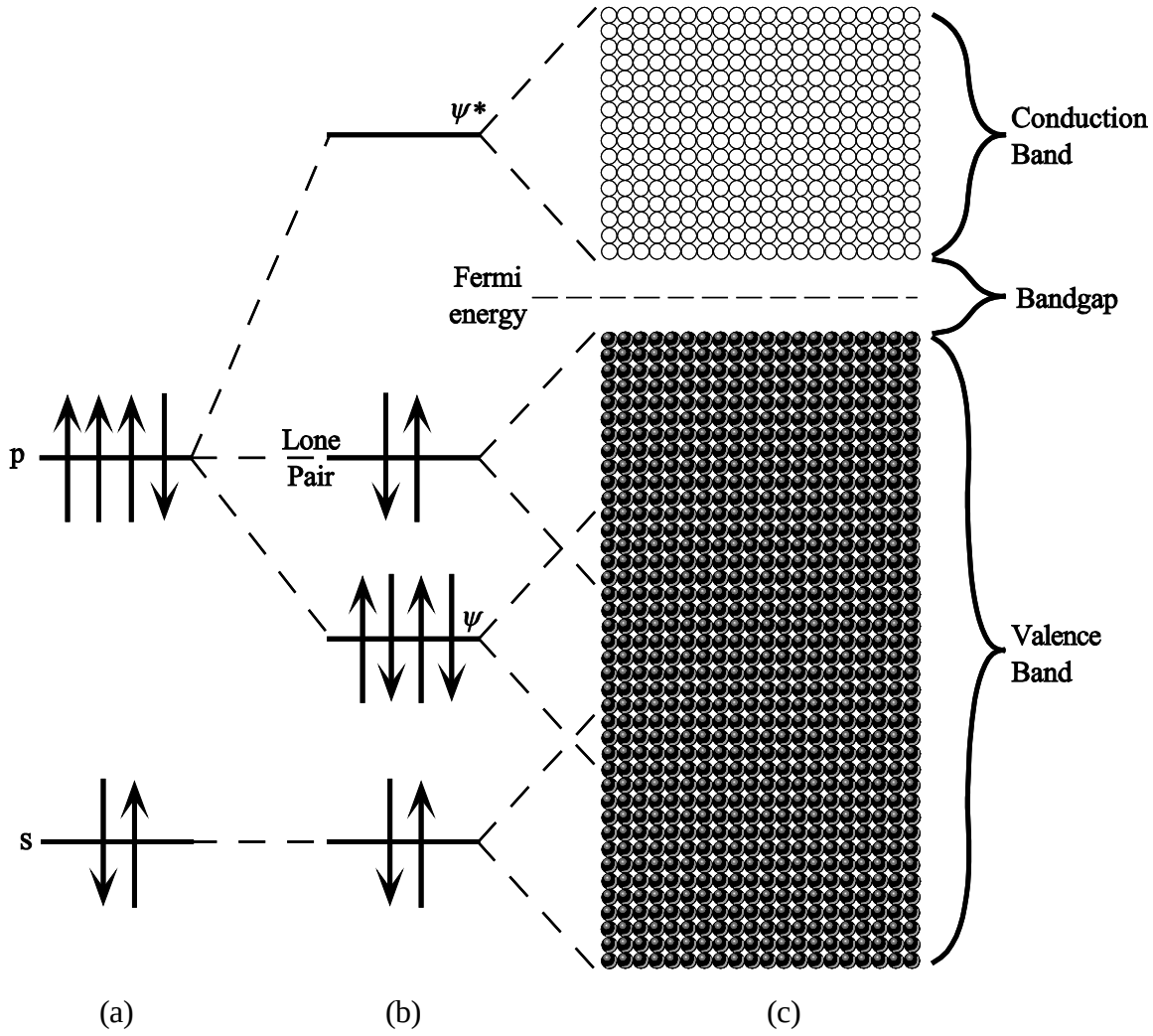


**Figure 2-3:** **(a) Schematic view of the electron configuration of an isolated chalcogen atom with six valence electrons. (b) Two atoms combine to form a solid in which two of the four p-state electrons form covalent bonds. The other two p-state electrons do not participate in bonding and form a lone pair. Also, shown are the bonding, $\psi$, and anti-bonding, $\psi^*$, states. (c) Bonding interaction of several atoms broaden the atomic levels into bands.**

Now, we must consider the interaction of atoms in an entire solid using quantum mechanics. The case where only two atoms are interacting is over simplified as normally solids consist of approximately $10^{24}$ atoms. Although the large number of interactions creates some mathematical complexity, the theory was first derived for crystalline materials

where the long range periodicity allowed for a number of important simplifications. The result was the band theory of solids.

When the entire solid is considered, the result is that an enormous number of states fall within a small energy range; therefore, the states can be treated as a continuous distribution in energy over a given range. The electronic states of each atom combine in such a way to form almost continuous regions of energy where electrons can exist. These regions are called bands and are sometimes separated by regions where no states are possible called gaps. Figure 2-3 (c) shows the solid form of a chalcogen where we see the structure of a typical semiconductor. The highest band of filled energy states is referred to as the valence band (VB), the lowest empty band is the conduction band (CB), and the region between those two bands is called the forbidden gap. The forbidden gap corresponds to the difference in energy from the top of the valence band to the bottom of the conduction band and is most often referred to as the bandgap ($E_g$).

An extremely important level within a material, called the Fermi level, is also shown in Figure 2-3 (c). The Fermi level is a product of the Fermi-Dirac distribution,

$$f(E) = \frac{1}{1 + e^{\left(\frac{E - E_F}{k_B T}\right)}} \tag{2.1}$$

which is the probability of finding an electron in a state with energy $E$. In the distribution $E_F$ is a material constant called the Fermi energy, $k_B$ is the Boltzmann constant and $T$ is the temperature in degrees Kelvin. At absolute zero all states with energies below $E_F$ are occupied, while all states with energies above are $E_F$ vacant, and at any temperature the probability of finding an electron with energy $E = E_F$ is $f(E) = \frac{1}{2}$. Any solid contains a fixed number of electrons and those electrons fill the allowed states up to $E_F$ (at $T = 0K$) according to the Pauli Exclusion Principle. The significance of the Fermi level arises from its location amongst the bands in a solid. Solids where the Fermi level is within the conduction band are metals, and where it is within a gap are insulators. Semiconductors, which are the focus of this thesis, are insulators where the bandgap is small so that the addition of small amounts of energy may promote the electrons from the valence band into the conduction band.

The significance of the band theory of solids lies in its ability to predict both electrical and optical properties of materials. The bands themselves represent the density of electronic states per unit energy per unit volume at energy *E*, which can be described by a function called the density of states (DOS). In the case of a crystalline solid, for which the band theory was first developed, the DOS is shown in Figure 2-4 (a). The long range periodicity of the crystalline structure results in two consequences. First, there are definite energies called band edges where the DOS drops to zero as a function of $E^{1/2}$. Second, all the electronic wavefunctions within a band extend throughout the entire solid.

The band theory was originally developed for crystalline solids, but after the discovery of an amorphous semiconductor [1] it was clear that it would need to include amorphous materials as well. Amorphous materials lack long range order and significant changes to the DOS were needed in order to account for the disorder present in the structure. It was Anderson [21] who was the first to show quantitatively that the effects of a sufficiently large amount of disorder on the Schrödinger equation resulted in a localization of all states in the band. That meant that unlike in a crystalline material, an electron in an amorphous material was localized in space and not free to move throughout the whole solid. He further suggested that the localized states are a direct result of degree of disorder in the lattice, and the magnitude and energy spread of the localized states are proportional to the amount of disorder in the atomic structure.

The sharp band edges present in crystalline materials are due to long-range order and in amorphous materials those sharp edge disappear [22]. In [22] Mott stated that changes in the Bloch wave functions at the conduction and valence band edges would produce extended tails that would enter the forbidden gap region. The model, shown in Figure 2-4 (b), can apply to alloy glasses with compositional as well as positional disorder therefore including the pnictogen-chalcogen compounds, and in the case where the tails overlap in the gap region the result is a model that resembles a metal.

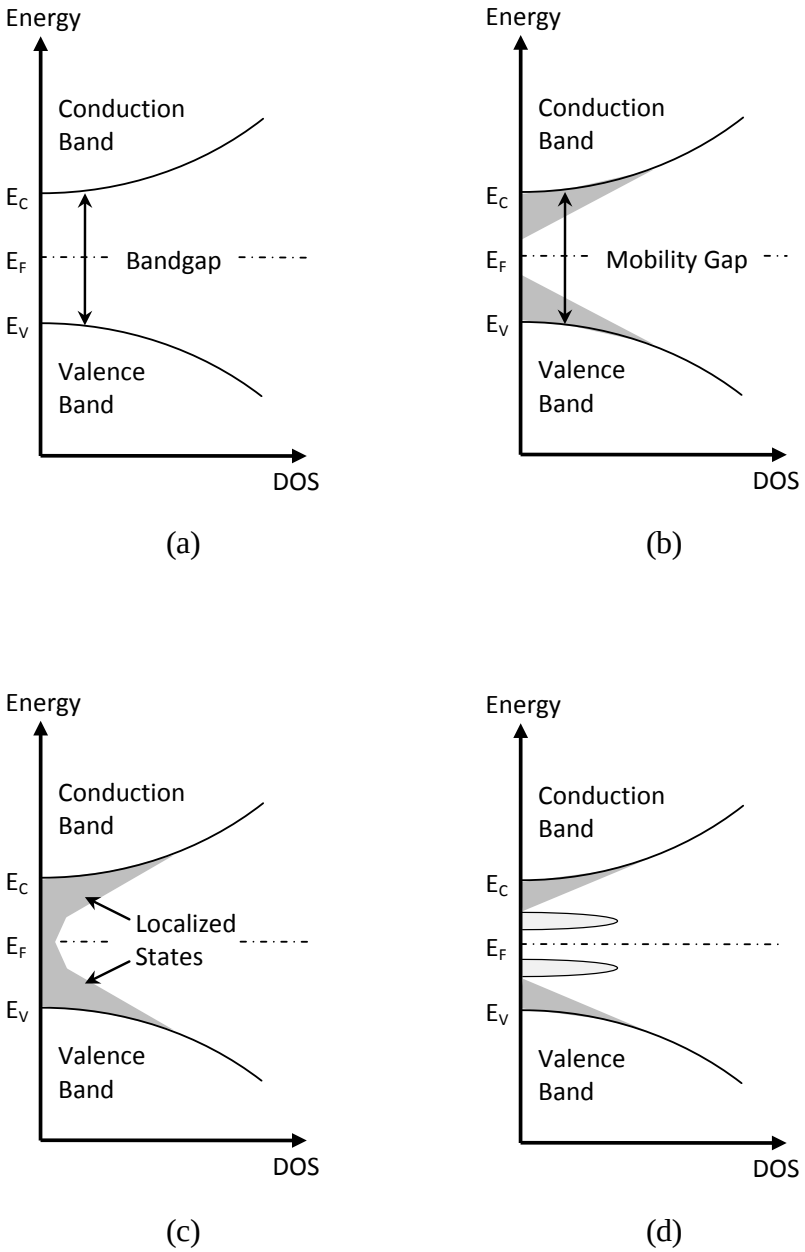


**Figure 2-4:** **Parabolic Density of States (DOS) models for semiconductors. (a) Classic crystalline case showing the well defined edges for the two extended state bands separated by a bandgap. (b) Mott's initial proposed DOS model for amorphous semiconductors showing the smearing out of the band edges caused by local variations in the lattice parameters. (c) Cohen, Fritzsche and Ovshinski (CFO) model showing the localized states extending across the forbidden gap. (d) Marshal – Owen DOS model containing deep donors below acceptors.**

The tail states proposed by Mott directly affect the carrier conduction within amorphous semiconductors. In a crystalline structure the carriers travel in the conduction or valence band through energy states that extend throughout the entire crystal. Mott argued that from a certain energy on the electronic states in an amorphous material become extended, and those extended states lead to transition energies in the conduction and valence bands. The transition energies were thought to produce a jump in the mobility, which was later shown to be false, and as such were called mobility edges, which are equivalent to the band edges in a crystalline material. Similarly, the change in the mobility of the charge carriers led to the idea of a mobility gap in amorphous materials that is analogous to the bandgap in crystalline materials. The mobility gap explains how it is possible for amorphous materials to behave as semiconductors.

After Mott's postulates in [22] a model was put forth by Cohen, Fritzsche, and Ovshinsky known as the CFO model [23]. The CFO model, shown in Figure 2-4 (c), is basically an extension of Mott's model which states that Mott underestimated the amount of disorder in the amorphous solid. That assumption is based on four principles not included in Mott's model. First, the band tails of amorphous materials depend on the degree of divergence from perfect periodicity. Second, there are sharp mobility edges in each band that separate the extended states from the localized states. Third, the localized band tails extend across the gap region resulting in an overlap at the Fermi level. This last statement suggests metallic conduction; however, the widened tail states are still highly localized in space as they were in Mott's original model. Lastly, amorphous materials are not bound by the strict constraints on long range order imposed on their crystalline counterparts. The result of the last assumption would be that each atom would be expected fulfill its valence requirements locally, known as the 8-N rule, removing any distinct structure in the density of localized states in the gap region. This last point results in contention with the CFO model because it does not show a structure in the gap region due to defects in the amorphous lattice.

The contention with the CFO model led Marshall and Owen to propose the DOS model [24] shown in Figure 2-4 (d). The two noted that both crystalline and amorphous solids

would contain defects such as dangling bonds, vacancies, interstitials, and impurities. The defects lead to additional localized states within the mobility gap in the form of electron and hole traps. The new trap states are in addition to the disorder induced tail states. It was previously assumed that the disorder induced states would cover up these defect states; however, Marshall and Owen proposed that there would be significant mid gap states caused by the defects. They concluded that there are acceptor-like hole traps about 0.43 eV above the valence band [25]. They also surmised that the position of the Fermi level is determined by donor-like and acceptor-like traps in the mobility gap, where the concentration of traps would self-adjust to ensure that the Femi level remained near the center of the mobility gap. Predicting electronic properties of amorphous materials became much more difficult as even small concentrations of these mid gap states can render doping of the semiconductor with donors or acceptors ineffectual.

## 2.3 Chalcogenide Glasses

Until now our discussion has been on amorphous materials in general; however, the focus of this thesis is photoinduced anisotropy in chalcogenide materials. Chalcogens are atoms occupying column six of the periodic table namely oxygen, sulfur, selenium, tellurium, and polonium. All the chalcogens have six valence electrons and they are arranged as shown in Figure 2-3 (a). The arrangement in Figure 2-3 (b) shows that the isolated atom has two paired s-electrons, two p-electrons available to form covalent bonds, and two lone pair electrons. It is those outer lone pair electrons which do not participate in bonding that made Kastner [26] point out that the chemical bonding of chalcogenide atoms is fundamentally different than for all other amorphous semiconductors.

In order to define exactly what a chalcogenide compound is, we say that typically any amorphous material containing an abundance of chalcogen atoms can be considered a chalcogenide glass. The exception is that of oxygen rich compounds which fall into a special category of oxide glasses. The term glass or non-crystalline can be used synonymously with the term amorphous material [27], as it is a particular case of the

amorphous state. The glassy state possesses all of the features of the amorphous state, but is characterized by its method of preparation.

To obtain a glass, or amorphous material, the liquid form of the material is quickly cooled or quenched. Melt quenching simply involves cooling the molten form of a material sufficiently quickly; where the cooling rate must be sufficiently fast so as not to allow crystal nucleation and growth. In the case where a liquid is slowly cooled from a melt, the solid is formed by a discontinuous solidification, and the bonds have time to align themselves into the proper orientation; therefore, forming a crystalline material. By rapidly quenching the liquid, atomic motions become so sluggish that the atoms do not have time to align for proper bonding and the result is that of a frozen liquid or glass, shown in Figure 2-1, where an arbitrary viscosity value of at least $10^{15}$ poise is commonly taken to characterize a glass [27].

The cooling rate required is dependent on the materials ability to form a glass and the so called glass transition temperature. This is the point where the transition from liquid to glass takes place, or the temperature at which the liquid has reached a viscosity of $10^{13}$ – $10^{14}$ poise [27]. Not all chalcogenides are good glass formers; however, they all have a glass transition temperature. Although the term glass is typically reserved for amorphous materials prepared by melt quenching, we will expand our definition to include materials that exhibit glass transition phenomena. Therefore, even though all the samples studied for this work were prepared by thermal evaporation or cathode sputtering, they may be called glasses as they do exhibit a glass transition. Throughout the remainder of this work we may use the terms glass and amorphous interchangeably; however, it is essential to recognize that amorphous semiconductors are metastable thin solid films [27], while a glass is also metastable it is essentially a frozen or supercooled liquid [28].

Chalcogenide glasses are fundamentally different from any other amorphous semiconductors; however, they do share comparable electronic structures. The comparable electronic structures result in very similar electrical properties which are outlined briefly in the next section. Following that is a section that outlines the optical

properties of chalcogenides. The second to last section discusses the differences in chalcogenide glasses which make them fundamentally different and lastly, the materials specific to this thesis are discussed briefly.

### 2.3.1 Electrical Properties

In Section 2.2, on amorphous semiconductors, it was stated that any material where the Fermi level lies within the conduction band is a metal and any material where the bandgap is large and the Fermi level is within the gap is an insulator. Semiconductors are technically insulators; however, they are insulators where the bandgap is on the order of a few electron volts. Chalcogenide glasses are by definition semiconductors as they typically have a bandgap of about 1 – 2.5 eV, which is sensitive to material composition. Tellurium and sulfur based compounds have the smallest and largest bandgap respectively, 0.7 eV in GeTe [17] and 3.24 eV in $GeS_2$ [29]; meanwhile, compositions containing selenium tend to be in the middle of those two extremes, 0.96 eV in $As_2Te_3$ [30] and 1.76 eV in $As_2Se_3$ [17]. Oxygen rich compounds typically have a bandgap of 10 eV and are considered insulators.

When we talk about electronic properties of semiconductors we typically mean the conductivity, which can range from $10^{-3}\ \Omega^{-1}cm^{-1}$ to $10^{-15}\ \Omega^{-1}cm^{-1}$ [17, 25] at room temperature. The conductivity is directly proportional to the electron and hole transport properties of the material. In a metal the bands are only partially filled, so the electrons can easily gain energy from an applied electric field and contribute to conduction. Conversely, the bandgap in semiconductors restricts the number of electrons and holes, leading to higher resistances. However, in a crystalline semiconductor electrons in the conduction band and holes in the valence band are able to move in the extended states. The conductivity is then given by

$$\sigma = ne\mu_e + pe\mu_h \tag{2.2}$$

where $n$ and $p$ are the electron and hole densities, $e$ is the electric charge, and $\mu_e$ and $\mu_h$ are the electron and hole drift mobilities.

The free electrons and holes are created by thermal vibrations of the crystal lattice and their mobilities are limited by scattering events. The scattering events in a crystalline semiconductor are a result of impurities, defects, and lattice vibrations, which limit the drift mobility of carriers and ultimately lower the mobility. Amorphous semiconductors tend to have lower mobilities than crystalline semiconductors because of the disorder inherent in their structure. That disorder results in localized states in the gap region which create band tails that extend into the gap and act as trapping centers. An electron or hole that would otherwise contribute to conduction may become trapped in a localized state, to be released sometime later. Thus, the traps effectively reduce the amount of time that a carrier can contribute to conduction.

The actual mechanism behind conduction in amorphous semiconductors is not well known. It is known that conduction depends directly on temperature – at any temperature greater than 0 K there is a probability of an electron being excited to the conduction band where that probability depends on temperature. At high temperatures the probability that an electron is promoted is much greater than at lower temperatures. At low temperatures, conduction occurs mainly due to electron hopping between midgap states because the hopping current is much larger than the drift current. Hopping is a phenomenon that can occur whenever there is a network of localized states [31], and is an abbreviation for the photon assisted quantum mechanical tunneling of an electron from one localized state to another.

The greatest difficulty in developing a model for chalcogenide glass conductivity is accounting for the disorder in the network. Unlike crystalline semiconductors which are periodic, glasses lack translational symmetry. Therefore, the standard band structure calculations used for determining electronic transport in crystalline materials cannot be applied to glasses. Any model must account for the random disorder which leads to localized states within the gap because the conduction properties of the glass depend on the nature and density of those localized states.

## 2.3.2 Optical Properties

Conduction within semiconductors can also be altered by external stimuli such as light and/or x-ray photons. If the incoming photons possess enough energy they can excite electrons from the valence band to the conduction band thereby changing the conductivity of the material. This photoconductivity is directly related to the energy of the incoming photons, given by

$$E_{ph} = h\nu \tag{2.3}$$

where $h$ is Planck's constant and $\nu$ is the frequency of the photon (i.e. $\nu = \frac{\lambda}{c}$). If the photon energy is greater than or equal to the bandgap energy of the semiconductor the photon will be absorbed, and an electron will be promoted from the valence band to the conduction band. Figure 2-5 depicts the process of a photon being absorbed in a semiconductor. It shows that the location in the conduction band to which the electron is promoted depends upon the photon energy. When the photon energy is on the order $E_g$ the electron is promoted from the top of the valence band to the bottom of the conduction band; however, if the photon energy is much greater than $E_g$ then the electron is excited to a higher level in the conduction band. The excess energy of the electrons which are promoted to higher levels is lost due to lattice vibrations (phonons).

In a crystalline semiconductor any incoming photon with energy less than $E_g$ will not provide sufficient energy to generate an electron hole pair. Therefore, the photon will not be absorbed and for wavelengths corresponding to those photon energies the semiconductor will be transparent. For amorphous semiconductors there are tail states which extend into the gap and effectively alter the ability of the semiconductor to respond to incoming photons. These localized tail states, shown in Figure 2-4 (b), (c), and (d), can allow the creation of electron-hole pairs via sub-bandgap light.

The ability of a material to absorb is a material property; however, the number of photons absorbed is directly dependent on the material thickness. Consider an ensemble of photons of intensity $I_0$ incident on a semiconductor surface, as shown in Figure 2-6.

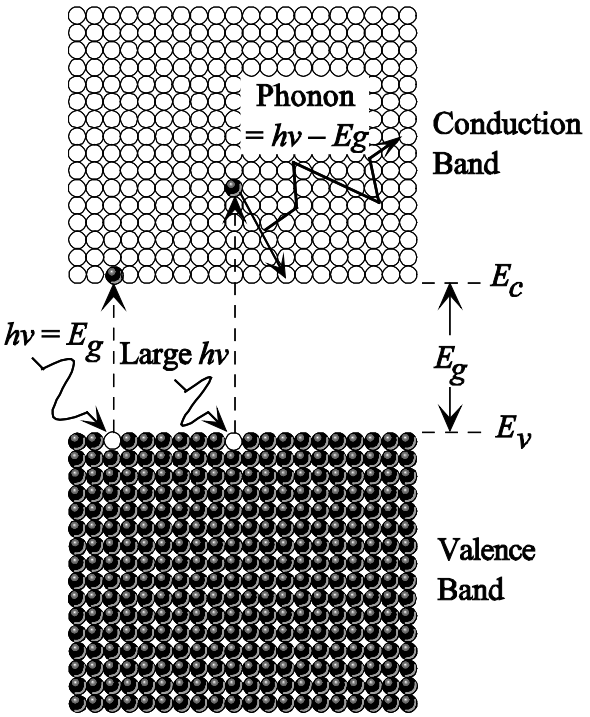


**Figure 2-5: Schematic showing the absorption of a photon in a semiconductor. The process shows the generation of an electron hole pair whereby an electron is promoted to the conduction band and a hole is left in the valence band.**

After some depth in the material $L$, the intensity will have decreased to $I(L)$. If we look at the incremental volume, indicated by the shaded area, then the small decrease in intensity $\delta I$ due to absorption is

$$\delta I = -\alpha I(L)\delta L \tag{2.4}$$

where $\alpha$ is a proportionality constant called the absorption coefficient. The absorption coefficient is a material property which can be defined as

$$\alpha = -\frac{\delta I}{I(L)\delta L} \tag{2.5}$$

The absorption coefficient, which has the units of length$^{-1}$ (i.e. m$^{-1}$), depends on the photon energy and hence, the wavelength of transmitted light; therefore, integrating Equation 2.5 with constant wavelength we can obtain what is known as the Beer-Lambert law,

$$I(L) = I_0 e^{-\alpha L} \tag{2.6}$$

which demonstrates that the transmitted intensity decreases exponentially as the beam passes through the material. The distance over which 63% of the photons are absorbed is referred to as the penetration depth, which is defined as

$$\delta = \frac{1}{\alpha} \tag{2.7}$$

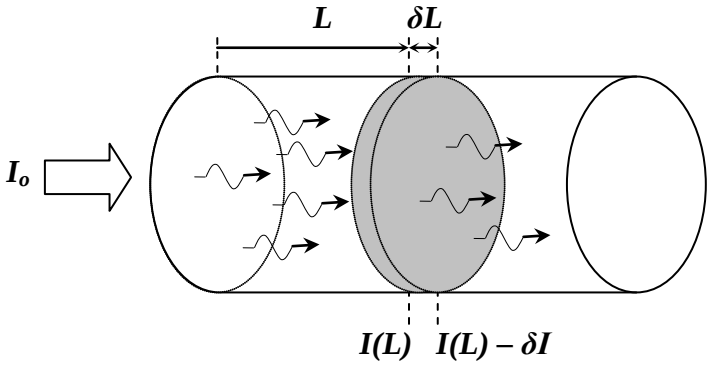


**Figure 2-6: Illustration of the absorption of photons when passing through an incremental volume element of a solid.**

The optical absorption of amorphous semiconductors is different from that of crystalline semiconductors due to the localized states present in the gap region of amorphous materials. The localized states allow for a greater variety of excitation and relaxation processes. A typical response curve showing the dependence of optical absorption on photon energy is shown in Figure 2-7. There are three regions where different processes are responsible for the absorption in each region.

In region 3 of the curve the photon energies are above the bandgap energy. At these photon energies typical absorption coefficients are in the range from $10^4 < \alpha < 10^6$ cm$^{-1}$, due to interband absorption (valence to conduction band). It is normally assumed that the density of states in this region can be expressed as a power law relationship of the form $g_v(-E) \propto E^p$ and $g_c(E) \propto \left(E - E_g\right)^s$ where the zero energy point is $E_v$. The photon energy dependence of the absorption is

$$\left(\alpha h\nu\right)^{1/x} = C\left(h\nu - E_g\right) \tag{2.8}$$

where $x = p + s + 1$ and $C$ is a proportionality constant. If the density of states for both the conduction and valence band are parabolic, then $p = s = 1/2$ and the photon energy dependence of absorption becomes

$$\left(\alpha h\nu\right)^{1/2} = C\left(h\nu - E_g\right) \tag{2.9}$$

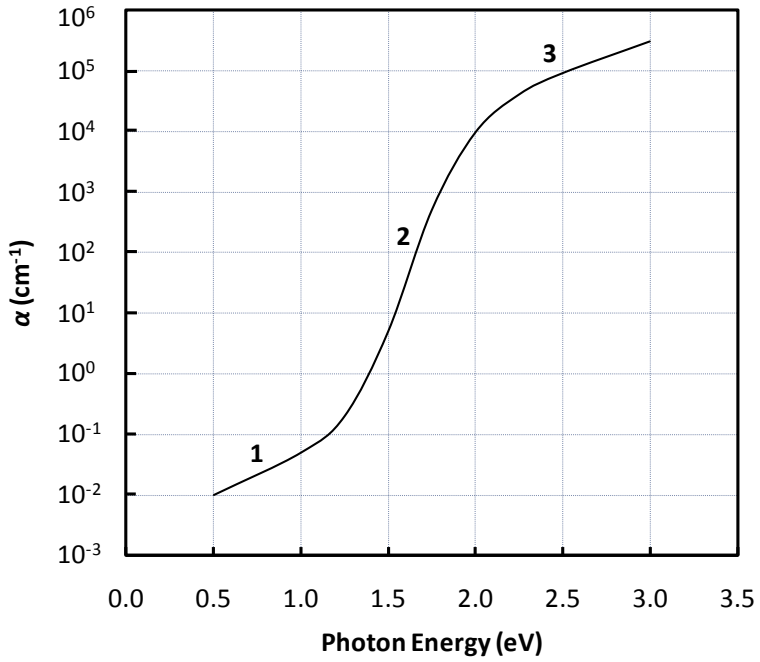


**Figure 2-7: Typical logarithmic absorption versus photon energy curve for an amorphous semiconductor (Data extracted from [16]). Region 1 is the absorption tail, Region 2 is the Urbach edge, and Region 3 is the power law region.**

The form of absorption expressed in Equation 2.9 is observed experimentally in many amorphous semiconductors. Specifically, the absorption as a power law function of photon energy for $As_2Se_3$ is shown in Figure 2-8, which is commonly referred to as a Tauc plot. The majority of the plot scales linearly for $(\alpha h\nu)^{1/2}$ as a function of $(h\nu - E_g)$. If the linear portion of the plot is extended such that it intersects the photon energy axis the resulting intercept is the optical bandgap of the compound, $E_o$, or the Tauc bandgap. Although the behavior shown in Figure 2-8 is typical it is not ubiquitous to all amorphous semiconductors. There are compounds that do not exhibit the power law relationship and as a result it is not possible to obtain the optical gap from a Tauc plot. In that case an alternative method of selecting the photon energy at which the absorption coefficient reaches $10^4$ $cm^{-1}$ as the optical gap, which is then denoted $E_{o4}$.

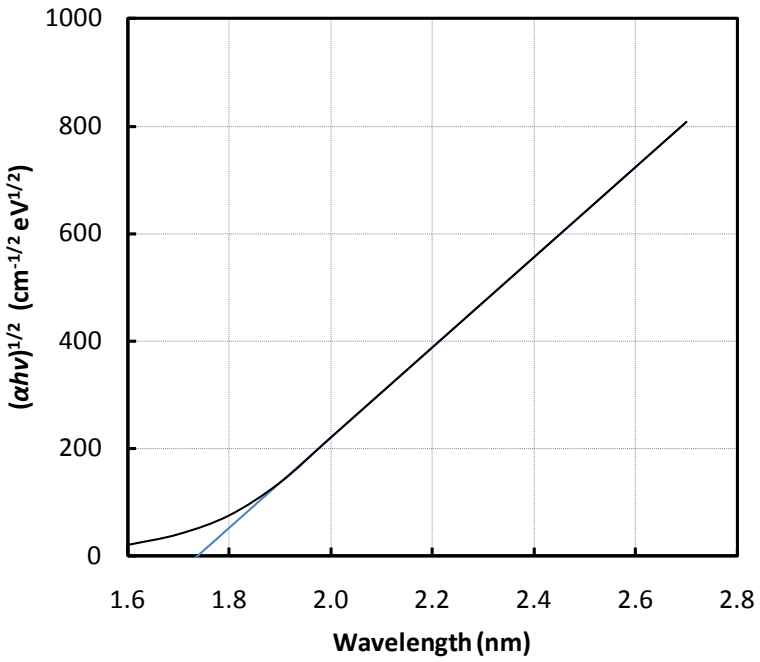


**Figure 2-8:** **A Tauc plot showing the absorption edge of $As_2Se_3$. The functional dependence on photon energy is given by $(\alpha h\nu)^{1/x} = C(h\nu - E_g)$. The intercept on the photon energy axis indicates the $E_o$ (Data extracted from [17]).**

The portion of Figure 2-7 labeled as region 2 is generally called the Urbach edge region, where typical absorption coefficients are in the range of $1 - 10^3$ $cm^{-1}$. In this region the absorption decreases with photon energy at a slower rate than the power law predicts. It has been experimentally demonstrated for most amorphous semiconductors and is a result of the transitions between tail states and the valence or conduction bands. The tail states cause the absorption edge to tail off into the gap region. The Urbach edge region is more accurately predicted by an exponential dependence on photon energy

$$\alpha \propto Ce^{-K(E_O - h\nu)} \tag{2.10}$$

where *C* is a proportionality constant and K is a temperature dependent constant (typical values at room temperature are in the range $10 - 25$ $eV^{-1}$). The exponential relationship is shown in Figure 2-9 for $As_2Se_3$. It is so widespread amongst amorphous semiconductors that it is considered a general feature; however, it also appears in crystalline alkali halides.

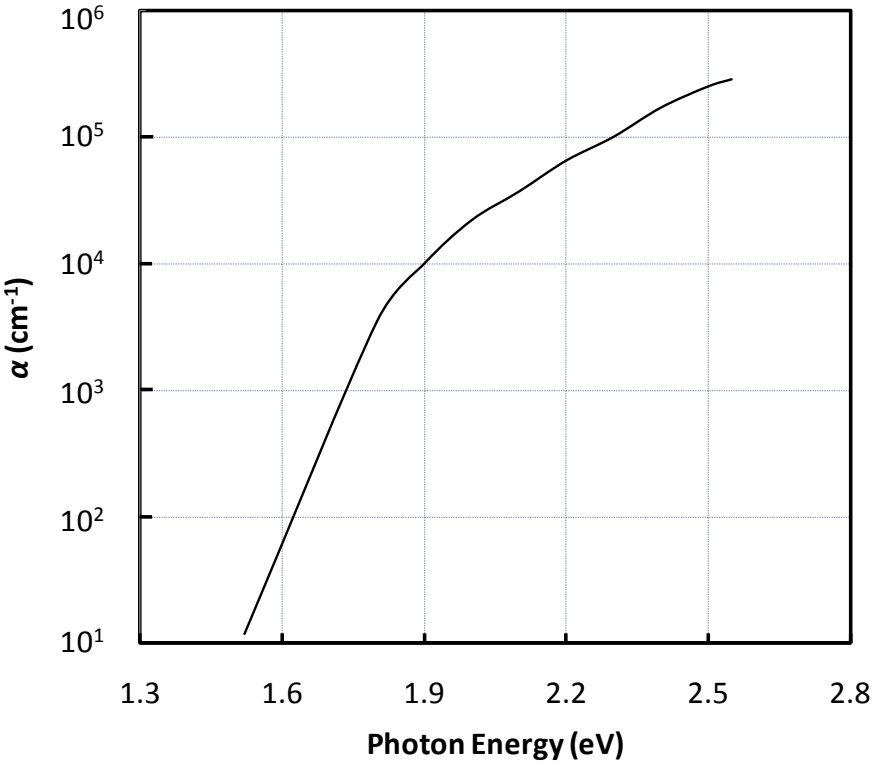


**Figure 2-9: Optical absorption edge of As2Se3 showing an exponential behavior at room temperature. (Data extracted from [17]).**

The last region of Figure 2-7, labeled as region 1, typically has absorption coefficients less than 1 $cm^{-1}$ and is called the absorption tail or shoulder. In this region absorption is due to transitions between defect states in the middle of the energy gap and extended states in the valence or conduction bands. Transitions between defect states require considerably less energy; therefore, the photon energies required to excite these transitions is smaller than the bandgap energy and usually involves wavelengths in the far infrared. The value of the absorption coefficient in this tail can be said to be a measure of the density of defect states present in the material.

The absorption processes in an amorphous semiconductor are a direct result of its disordered structure. In turn, the absorption plays a direct role in the photosensitivity of chalcogenide glasses. The photoinduced properties and behavior of amorphous chalcogenides discussed further in Chapter 3 all depend on the materials ability to absorb light.

### 2.3.3 VAP's and IVAP's

Chalcogenide glasses have two lone pair electrons that do not participate in the bonding structure, making their chemical bonding fundamentally different from all other amorphous semiconductors [26]. That bonding structure, coupled with a lack of measurable density of unpaired spins, are the main reasons that chalcogenides are considered such unique materials. The lack of measurable density of unpaired spins stems from experimental observation of a lack of electron spin resonance. According to Mott that is not the only hurdle to understanding chalcogenide glasses [17], as there is also evidence that the Fermi energy is pinned and there is a finite density of states. As a possible solution to this problem Mott states that one could assume that the density of states is zero at $E_F$; however, this solution does not make sense as the Fermi energy is determined by deep donors near the middle of the gap – refer to Figure 2-4 (d). Anderson [32] proposed a more plausible explanation of the experimental results by postulating that the spin pairing of electrons at the defect states would be energetically more favorable than unpaired spins. As a result the lowest energy state would have no unpaired spins. Anderson further suggests that the lack of unpaired spins is due to a polaron effect involving an electron-phonon interaction that will polarize its surroundings into a lower energy configuration. The result is a negative effective correlation energy for electrons.

The concepts brought forth by Anderson were taken further by Street and Mott [33]. They took Anderson's concept of negative correlation energy for electrons and applied it to specific defects, namely dangling bonds (DB's). They used the notation $D^0$ to designate an unpaired electron or a DB, where the superscript indicates the charged state. In the case of a DB there are two other possibilities for the charge state of the defect. First, it could be an under coordinated atom where the DB would be a negatively charged defect denoted as $D^-$. Second, the state could be that of an over coordinated atom where the DB would be a positively charged defect denoted as $D^+$. The two possible states correspond to an electron being either added or removed, respectively.

The three possible defect states are related by the fact that the following reaction is assumed to take place

$$2D^0 \rightarrow D^+ + D^-$$

The configuration coordinate diagram of the reaction, shown in Figure 2-10, demonstrates that the reaction is exothermic. An exothermic reaction indicates that the total energy of the electrons plus the lattice (a polaron) associated with the two charged defects, $D^-$ and $D^+$, is lower than two neutral defects. Kastner, Alder, and Fritzsche [34] expanded on the model by Street and Mott using chemical bonding arguments to better understand the process. They switched notations in order to account for both the coordination and the charge. The notation became $C_1^0$ for $D^0$, $C_1^-$ for $D^-$, and $C_3^+$ for $D^+$, where the C stands for chalcogen atom, the subscript indicates the coordination number, and the superscript indicates the charge.

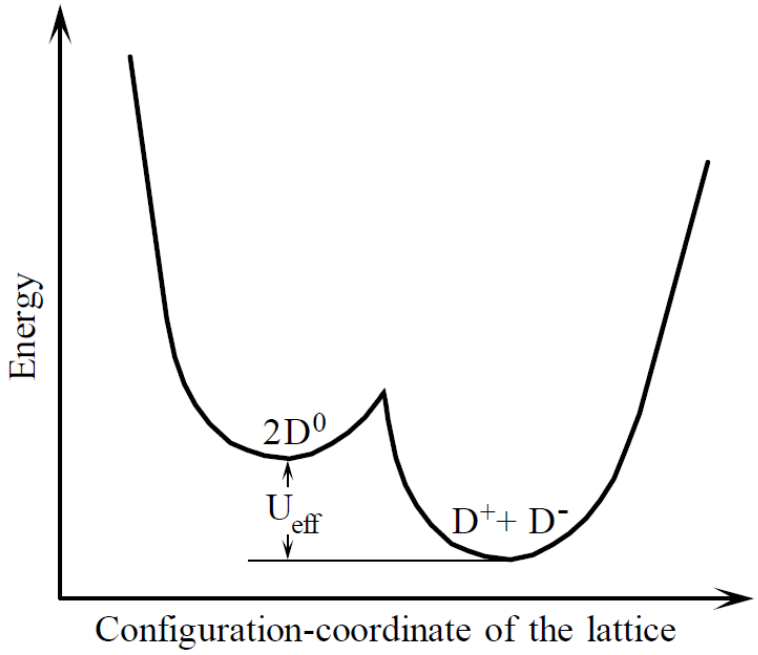


**Figure 2-10: Configuration-coordinate diagram for the formation of a $D^+D^-$ pair through the exchange of an electron between two $D^0$ centers. In the diagram *E* signifies energy and q is a configuration coordinate of the lattice [15].**

The model proposed by Kastner et al. involved a two stage process which results in the lowest energy configuration that does not contain unpaired spins. The two stage reaction begins with the removal of an electron from a neutral DB defect $C_1^0$ to create the charged

defect $C_1^+$. That charged defect interacts with the lone pair of a neighboring chalcogen, $C_2^0$, resulting in a threefold coordinated chalcogen, $C_3^+$. The result is a proper bonding configuration, similar to that of a pnictide atom, and is a lower energy state. The second stage of the process involves an excess electron moving to any of its three nearest neighbors. The bond between the atom and three fold coordinated atom is subsequently broken, and a singly bonded chalcogen atom with an extra electron $C_1^-$ remains. The formation of the $C_1^- C_3^+$ pair ($D^-$ $D^+$ in the model of Street and Mott), shown in Figure 2-11 (a), was termed a valence alternation pair (VAP) by Kastner, Alder, and Fritzsche. If the $C_1^-$ and $C_3^+$ defects are directly connected then the pair were called an intimate valence alternation pair (IVAP), which is shown in Figure 2-11 (b). The two reactions, at their simplest level, can be viewed as a type of bond switching.

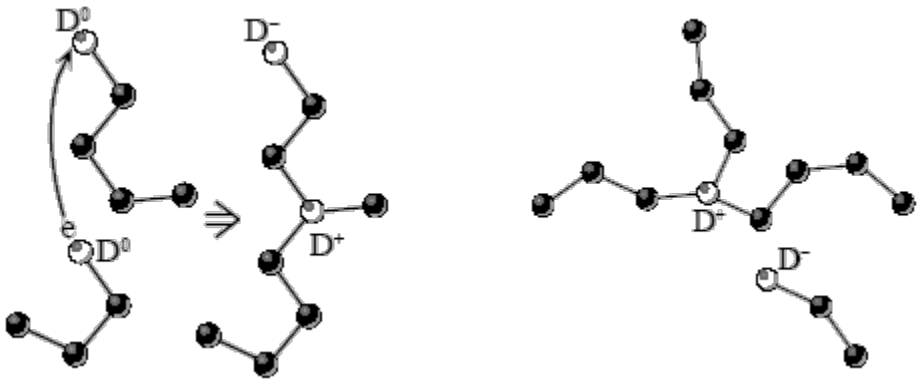


(a) (b)

**Figure 2-11: (a) Valence alternate pair. (b) Intimate valence alternate pair.**

The existence of a negative correlation energy and valence alternation was demonstrated in amorphous selenium by Kolobov et al. in 1997 [35]. In that work the authors combined results from optically induced electron spin resonance (ESR) with extended x-ray absorption fine structure (EXAFS) measurements. The experiments were carried out *in situ* under identical conditions and provide clear evidence for the existence of these two phenomena. All of the above demonstrate that the electronic properties of amorphous semiconductors are controlled by active centers.

## 2.4 Sample Preparation

Chalcogenide glasses can be prepared by a variety of methods. In general, amorphous solids (bulk samples) are prepared from melt or solutions; meanwhile, amorphous layers (thin films) are fabricated from the gaseous phase by condensing the vapors onto suitable substrates. The samples studied in this thesis were all thin films prepared by either thermal evaporation (vacuum deposition) or cathode sputtering. There are other methods of thin film preparation such as glow discharge or chemical vapor deposition which will not be discussed here.

The following sections outline the two preparation procedures used to prepare the films for this work; which are thermal evaporation and cathode sputtering. They also cover the substrate preparation techniques and cleaning procedures.

### 2.4.1 Substrate Preparation

For all samples tested in this thesis the substrate used was Corning 7059 glass. For the ordinary thin films of $As_2Se_3$, as well as samples doped with iodine, a plane substrate was used for deposition. However, for samples where it was necessary to apply an electric field the substrates were first coated with a thin layer of indium-tin-oxide (ITO) prior to sample deposition. The ITO coated substrates are commercially available or can be sputtered, and it is assumed that the cleaning procedure outlined below would be similar before the application of the ITO layer. Therefore, the cleaning procedure described below applies only to the glass substrate itself.

Preparation of the substrate involves a cleaning procedure which removes any impurities that may be on the glass surface. The procedure begins by cleaning the beaker rack which holds the substrates. It is cleaned and rinsed in an ultrasonic cleaner using extran MN-1 powder detergent dissolved in de-ionized water. Once the beaker rack is clean the glass slides are then placed in the rack inside the beaker and washed/rinsed for 4 cycles in the ultrasonic cleaning bath using the extran MN-1 powder detergent in de-ionized water. The

substrates are then removed from the bath and blown dry with high purity filtered air. Complete drying is achieved by baking the substrates overnight in an oven at 105 °C.

### 2.4.2 Thermal Evaporation

There were two types of films that were made by thermal evaporation; a-$As_2Se_3$ and a-$As_2Se_3$ doped with 0.1 atomic % iodine. The source material used for the $As_2Se_3$ thin films was high purity; stoichiometric, electronic grade liquid quenched vitreous $As_2Se_3$, 36.6 wt. % arsenic or 37.5 at. %. The source material for those samples doped with iodine had the same characteristics and preparation except that it contained 36.4 wt. % arsenic and 0.2 wt. % iodine. Both materials were obtained from Noranda Advanced Materials, Saint Leuvent, Quebec, Canada. The supplier used optical emission spectroscopy to verify the chemical content, composition and purity of the amorphous pellets.

The amorphous films were fabricated from the source material, which was initially in the form of pellets, through evaporation using an NRC 3117 thermal vacuum deposition system, illustrated in Figure 2-12. A mechanical vacuum pump was first used to evacuate the chamber followed by a diffusion pump to achieve a high vacuum of ~ $10^{-6}$ Torr. At this level of air pressure, the entire environment inside the deposition chamber has a minimal amount of impurities and the sample is ready for deposition.

The pellets were contained in a molybdenum boat and melted by passing a high ac current of approximately 100 amperes through the boat. The resulting boat temperature was ~ 360°C corresponding to a deposition rate of ~ 28 nm/minute; meanwhile, the substrate temperature was ~ 24 °C. Thermocouples were used to monitor both the boat and substrate temperatures, and quartz crystal was used to monitor the deposition rate, therefore allowing for any thickness to be prepared. Once the desired sample thickness was reached the boat current and diffusion pump were switched off. The system was then slowly cooled under vacuum for about 1 hour at which time the mechanical pump was switched off and the films were allowed to relax.

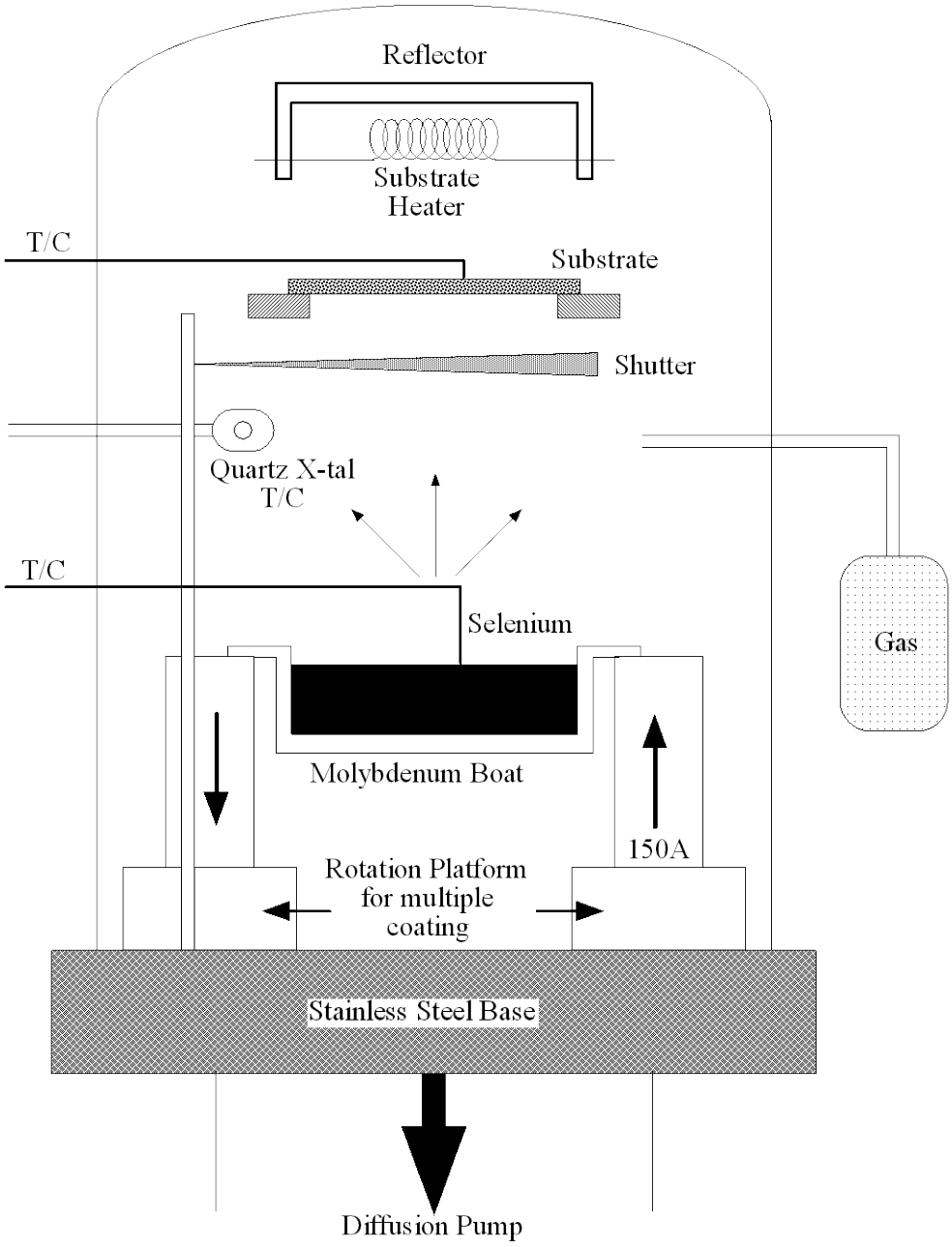


**Figure 2-12: Schematic of a vacuum deposition system.**

Normally thermal evaporation involves a source stream and substrate that are orthogonal to each other. The method by which the substrate is rotated to some angle before deposition is referred to as oblique deposition, shown in Figure 2-13. The result is materials which are macroscopically inhomogeneous due to a so-called shadowing effect [36], which causes a columnar growth structure with alternating dense and less dense regions. The effect has been demonstrated by scanning electron microscopy (SEM) and

transmission electron micrographs (TEM) on various compounds [37]. Several samples of a-$As_2Se_3$ were prepared at various deposition angles; however, at the time of this thesis PDi measurements on these samples had yet to be performed.

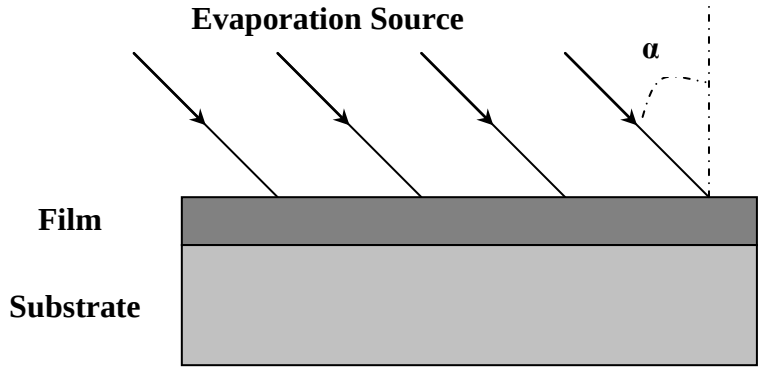


**Figure 2-13: Schematic illustration of oblique deposition by thermal evaporation. The angle α is the angle between the source and the orthogonal direction to the substrate – or the deposition angle.**

## 2.4.3 Magnetron Sputtering System

Amorphous Chalcogenide films can also be made using a sputtering system, which is shown schematically in Figure 2-14. In order to produce high quality films of any material, a reliable target must be used. Targets were made by hot pressing $As_2Se_3$ in the target holder using either a hot plate in atmospheric pressure under a fume hood, or a heating filament in a thermal evaporation chamber under vacuum like the one shown in Figure 2-14. Regardless of the production method of the target, eventually good quality thin films of a-$As_2Se_3$, 36.6 wt. % As, were produced and used for anisotropy measurements.

The procedure for sputtering a thin film of $As_2Se_3$ began with fastening the target to one of the three sputtering guns and placing the substrate on the turning table in the chamber. The system has a base pressure below $5x10^{-6}$ Torr. Once the chamber pressure reached the desired level, approximately 3 mTorr, Argon gas was pumped in at a controlled rate of 15 sccm. The table was then allowed to turn and the shutter to the target was opened.

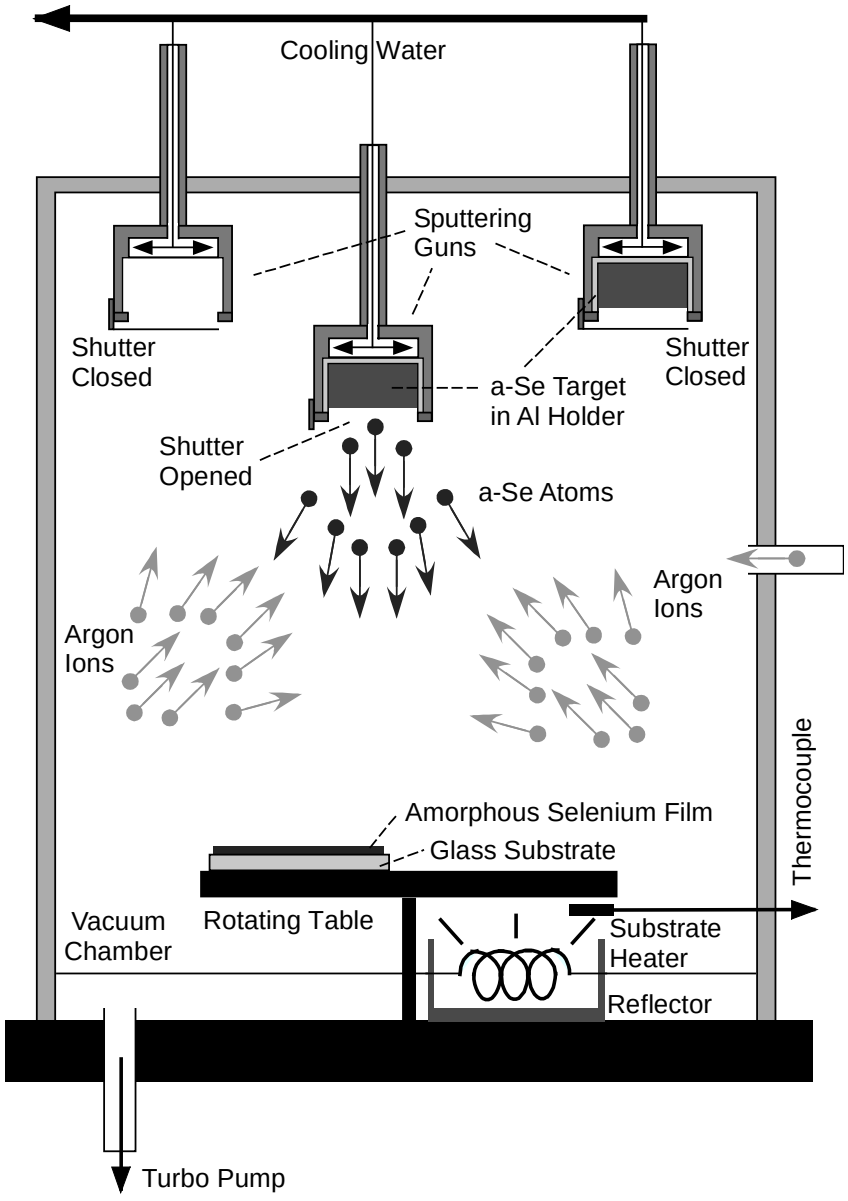


**Figure 2-14: Schematic of a cathode sputtering system.**

Once the shutter was opened RF power was supplied to the sputtering gun. There is a matching coupler that maximizes power to the gun which can be fine tuned in order to deliver maximum power to the load. When there was no longer any reflected power, the sputtering process would begin. Layers of a-$As_2Se_3$ would form on the substrate when the target was bombarded by the Argon plasma. The thickness of the sample was controlled by the flow rate of the Argon gas and the RF power. There is also a quartz crystal that can be used as a thickness monitor. When the desired sample thickness was reached, the RF power was turned off and the sample was allowed to relax. In the case

where electroded samples were required the same procedure for deposition was used; however, it involved two stages, one for the ITO and one for the source material.

## 2.5 Summary

Amorphous semiconductors have become important due to their significance in various applications. Compounds such as hydrogenated amorphous silicon (a-Si:H) are used in solar cells, thin film transistors, image scanners, and various types of sensors. The chalcogenides, although fundamentally different, are used in electrophotography, photolithography, Bragg gratings, optical waveguides, x-ray imaging, and a wide variety of other applications. The previous chapter presented an overview of amorphous semiconductors and chalcogenide glasses, highlighting some of the important properties which directly affect those applications.

# Chapter 3 Photoinduced Changes in Chalcogenide Glasses

## 3.1 Introduction

Non-crystalline chalcogenide semiconductors exhibit changes in composition, phase, electronic structure, and atomic structure [10, 38] when irradiated by light with a photon energy that is comparable to the bandgap. The changes that will be discussed in the following chapter are all photoinduced, meaning they are light induced, and they are all specific to amorphous materials.

The following chapter will introduce and discuss some of the most interesting photoinduced effects that may occur. Of those effects photoinduced anisotropy and photodarkening have been the most thoroughly studied. Photoinduced anisotropy, being the topic of this thesis will be explained in greater detail; however, other effects will also be outlined such as photoinduced crystallization, photoexpansion, photoinduced fluidity, photodiffusion, and photodoping.

The last portion of this chapter deals with the currently existing models attempting to provide a framework for photoinduced effects in amorphous chalcogenides.

## 3.2 Photoinduced Effects

Photoinduced changes in amorphous chalcogenides are due to the generation of electron-hole pairs. The absorption of a photon may result in an electron-hole pair either separating or recombining. If the electron-hole pair separates it will contribute to the electrical response of the material and may give rise to photoconductivity. The recombination can occur in two ways, either radiatively which would give rise to photoluminescence, or non-radiatively. Non-radiative recombination of photoexcited electron-hole pairs results in photostructural and optical changes to the material.

Macroscopic photostructural changes are unique to amorphous chalcogenides and are not observed in their crystalline counterparts. One of the reasons those changes are unique to chalcogenides is the nature of the amorphous structure. Rigid structural periodicity imposes constraints on the positions of atoms in a crystal; however, amorphous semiconductors are characterized by atomic structural disorder which can cause localization of electron and hole states in the forbidden gap [22]. The lack of rigidity to their structure allows amorphous semiconductors more freedom and flexibility for electron-hole creation events. Other reasons for the photostructural changes include low coordination number and lone pair electrons at the top of the valence band, which make it easier to deform the lattice and allow bond switching or extra bond formations to occur.

Typically, the photoinduced changes in chalcogenides are metastable meaning that it may take months or even years for the changes to disappear when the irradiating source is turned off. The changes may also be transient, effects that typically exist for only milliseconds after they are induced, such as photoconductivity, photoluminescence, and light induced Electron Spin Resonance (ESR). We are most concerned with metastable effects as photoinduced anisotropy is included in that category, and all of the effects discussed in this chapter are considered metastable. A further distinction can be made amongst the metastable effects regarding their reversibility. An effect is considered reversible if the initial state of the sample, prior to irradiation, can be restored at temperatures below the glass transition temperature, $T_g$ [16].

Photoinduced changes are also affected by the polarization state of the excitation source. That is to say that they can be either scalar or vectoral. Vectoral effects are directly related to the polarization direction of the excitation source, but scalar effects are completely independent of the source polarization. Often both vectoral and scalar effects are induced simultaneously by the same inducing source [12, 39]. However, they are different effects as demonstrated by the fact that they have different kinetics [40], different annealing temperatures [12, 40, 41], and different spectral excitation dependencies [41, 42]. Specifically, the scalar photoinduced effects require annealing above the glass transition temperature $T_g$ in order to be erased while the vectoral effects

typically relax at much lower temperatures, sometimes even room temperature [39]. Vectoral effects are induced much more efficiently by illumination with sub-bandgap light near the absorption edge. Light with higher photon energy will diminish a vectoral effect. In contrast, the reverse is true of scalar effects, where above bandgap light with high photon energy will increase the effect [41,42]. The most conclusive evidence that scalar and vectoral effects are independent of each other is the discovery of photoinduced dichroism in some chalcogenide compounds which do not exhibit a scalar effect [39, 40].

## 3.3 Photodarkening and Photobleaching

Chalcogenide materials that are exposed to near bandgap light experience a shift in the optical gap. In the case where a reduction of the optical gap occurs the process is referred to as photodarkening (PD). In the case of PD the material will become visibly darker upon illumination as was first observed by Berkes et al. [43] on a 1 μm film of $As_2Se_3$ that was exposed to focused microscope light. The reduction in the optical gap, defined in Section 2.3.2, is seen as a red shift, toward lower photon energies or longer wavelengths, of the absorption edge of the material [44]. The opposite effect, called photobleaching (PB), occurs when there is an increase in the optical gap and a blue shift of the absorption edge toward higher photon energies [45, 46, 47]. Both PD and PB are accompanied by a change in the index of refraction of the material called photorefraction, and all three effects are scalar effects.

PD contains both a reversible and an irreversible component. The absorption edge shift that occurs within an $As_2S_3$ sample is shown in Figure 3-1. In the as-deposited sample the absorption edge is at point 1, upon irradiation the absorption edge shifts to lower photon energies (longer wavelengths) indicated by point 3. Subsequent annealing near the glass transition temperature results in a reduction in the absorption edge back to higher photon energies (shorter wavelengths) indicated by point 2 on the plot. The exposure/annealing process can be repeated multiple times without fatigue; however, the film will never recover to its as-deposited state prior to illumination indicated by point 1.

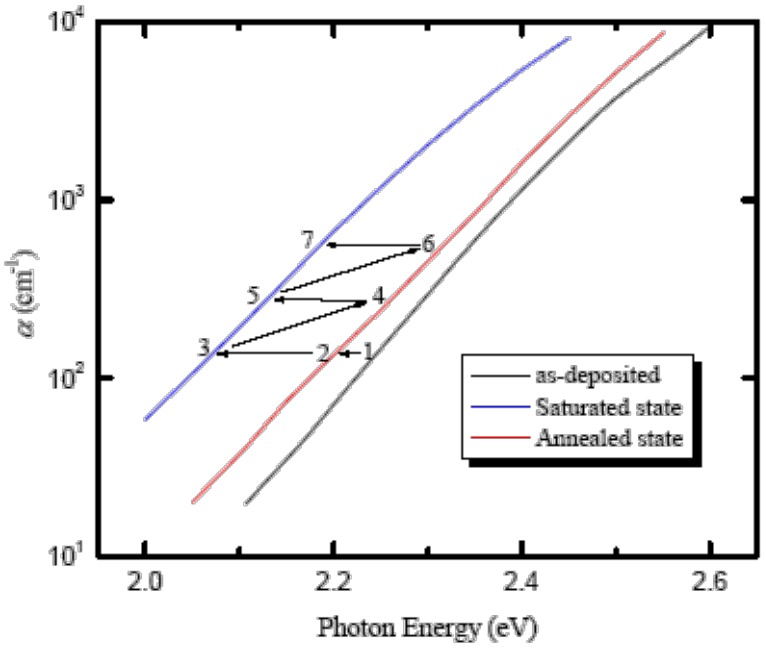


**Figure 3-1: Reversible photodarkening in an amorphous $As_2S_3$ film. The far right line is the as-deposited state, the far left line is the saturated photodarkened state and center line is the annealed state (Data extracted from [48]).**

PD has also been shown to be temperature sensitive in many chalcogenide materials [49]. In [49] Tanaka showed that no PD can be induced if the sample is at the glass transition temperature because the PD inducing rate is less than the annealing rate, and that an inverse relationship exists between temperature and absorption edge shift. The relationship between temperature and the shift in absorption edge is shown for $As_2S_3$ and $As_2Se_3$ in Figure 3-2. Clearly as the sample temperature $T_i$ decreases there is an increase in the magnitude of the shift in the absorption edge.

Tanaka also found that at low temperatures the absorption edge shift is not parallel. This is shown in Figure 3-3. The far right line is the spectral response of the absorption edge for an annealed $As_2S_3$ film at a temperature of 14 K. The far left line shows the spectral response of the absorption edge after PD (for the same sample and temperature) to saturation. The extra shift in the absorption edge (red line) can be annealed out in two ways: (1) by warming the sample to room temperature, (2) by irradiating the sample with sub-bandgap light, i.e. $h\nu < E_g$. What this means is that there are at least two mechanisms responsible for PD. The low temperature part, below room temperature, is

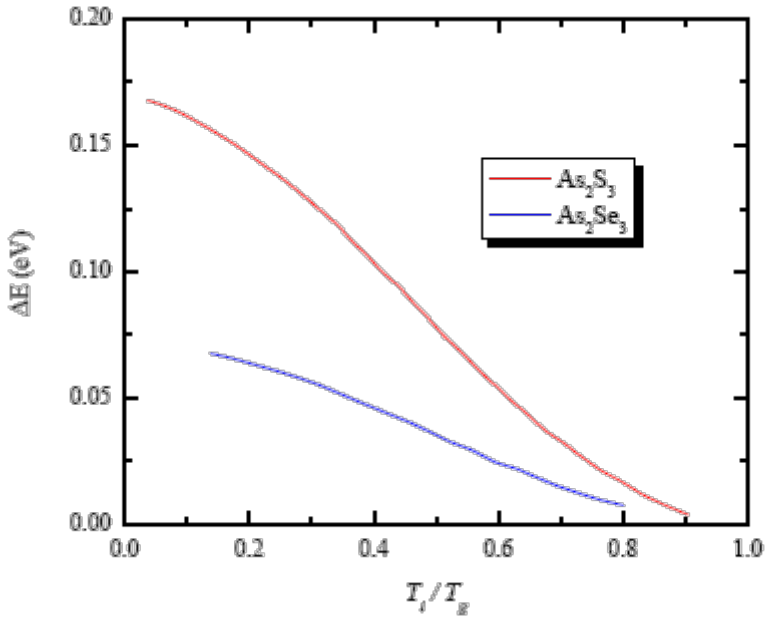


**Figure 3-2:** **Temperature dependence of the photodarkening for $As_2S_3$ and $As_2Se_3$ glasses. The magnitudes, ΔE, of photodarkening versus of the ratio of illumination temperature ($T_i$) to the glass transition temperature ($T_g$) (Data extracted from [49]).**

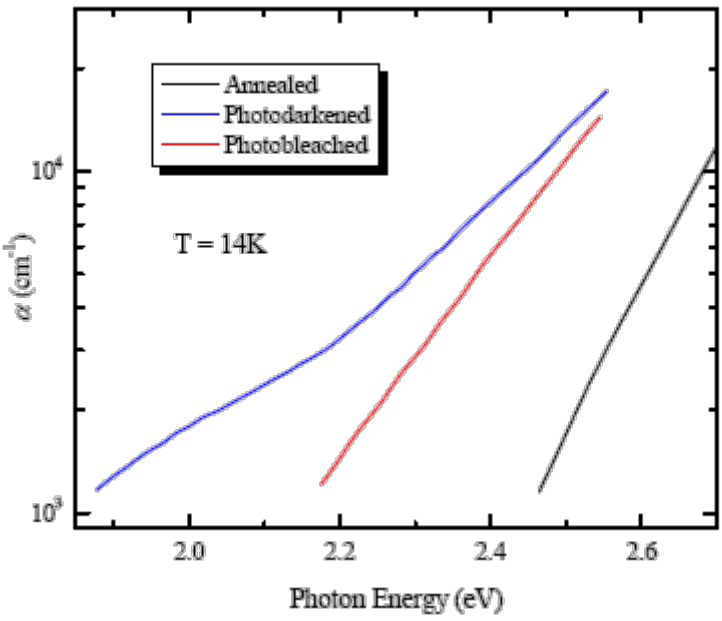


**Figure 3-3:** **Absorption edge spectral response at 14 K for an amorphous $As_2S_3$ film. Far right line is for the well annealed condition and the far left line indicates the photodarkened state induced by bandgap light. The center line indicates the photobleached state reached from the blue line after irradiation with sub-bandgap light ($h\nu < E_g$) (Data extracted from [38]).**

due to the photoinduced creation of charged defects [38]. Meanwhile, above room temperature PD may be caused by bond breaking and/or switching.

PD has been observed in bulk glasses [50] and thin films [51]; however, it is only displayed in amorphous materials and not crystals. Structural disorder cannot be solely responsible for PD as amorphous materials that do not contain a chalcogen do not exhibit the effect. The effect appears to be the result of the lone pair electrons [52]. X-ray Photoemission Spectroscopy (XPS) measurements on an amorphous $As_2Se_3$ film have shown that the shift in the valence band between the annealed and the photodarkened state has the same magnitude as the shift in the optical gap (approximately 0.2 eV). Therefore, the valence band, which is comprised of mostly lone pair electrons, and not the conduction band is responsible for PD.

The PB that occurs in chalcogenides cannot be removed by heat treatment, and appears to result from a different process [45, 46, 47]. Typically PB is found in Ge based chalcogenide compounds [53] but has also been seen in obliquely deposited $As_2S_3$ films [16]. PB is very sensitive to material composition and deposition technique.

## 3.4 Photoinduced Crystallization

Amorphous chalcogenides may be crystallized by short laser pulses, with energy near the bandgap, and then made amorphous again [54, 55, 56, 57]. The effect has been reported in various chalcogenide compounds, and has been confirmed by Raman spectroscopy of the samples [56, 58, 59, 60, 61, 62]. The process may or may not be reversible. The term reversible applies to processes which can be erased below the glass transition temperature, and in the case of photoinduced crystallization that depends on the sample. Some samples will crystallize when heated above $T_g$; however, for samples below $T_g$ crystallization will depend on material properties and the extent to which crystallization was induced.

Photoinduced crystallization is generally considered a scalar effect as it is usually not influenced by the polarization state of the irradiating source. However, investigations of photoinduced dichroism (PDi) at temperatures close to $T_g$ revealed oriented laser crystallization in a-Se films [63]. It was also shown that the polarization state influences the density of crystallites in the crystallization region of the film [64]. Therefore, whether or not the effect is scalar or vectoral depends upon the temperature of the sample during irradiation.

## 3.5 Photoexpansion and Photoinduced Fluidity

The light induced expansion of amorphous chalcogenide films has been observed in $As_2Se_3$ and $As_2S_3$ samples [65, 66, 67, 68, 69, 70, 71]. In [69] it was shown that the effect can be annealed out by heating to $T_g$ and then expansion can be induced again; therefore, the process is reversible. The effect can also be said to be scalar as the sources used were all essentially unpolarized.

The typical photoexpansion phenomenon results in a relative change in thickness of approximately 4-5% when the sample is exposed to above bandgap light [67, 71]. However, investigations of obliquely deposited films, where the angle between the normal to the substrate and the angle of incidence of the evaporated atoms was 80°, resulted in 'giant' photoexpansion of approximately 8% in thickness [65]. It was also found that photoexpansion could be induced in $As_2S_3$ with below bandgap light by as much as 3% [70].

The photoexpansion effect appears to be a scalar effect; however, there appears to be a polarization dependent reversible contraction and dilation in $As_{50}Se_{50}$ films [72]. If the film is irradiated with polarized light then there is a contraction in the direction parallel to the electric field vector of the inducing beam. The contraction is accompanied by dilation in the direction perpendicular to the electric field vector of the inducing beam.

Similar to photoexpansion, illumination of some chalcogenide films can result in permanent deformation. It was found that when a sample of a-$As_2S_3$ was elastically deformed and subsequently irradiated a fluid state was obtained [73]. The process is called photoinduced fluidity. Under illumination a sample can deform viscously with the deformation being restricted to the area of the focused laser spot. The dark viscosity is estimated at $10^{13}$ poise, while under illumination the viscosity may decrease to $5\times10^{12}$ poise [72, 73]. The process is athermal as the photoinduced fluidity increases with decreasing temperature, completely opposite of what would be expected from a thermally induced change in viscosity.

## 3.6 Photodiffusion and Photodoping

Chalcogenide glasses can be photodoped with metals, typically silver and copper. A thin metal film is first deposited on top of the chalcogenide glass and subsequent irradiation with bandgap light causes the metal atoms to diffuse into the glass. The diffusing species will distribute itself uniformly throughout the doped layer, where the concentration of dopant is typically 25 – 30 at. % [74]. The process is most efficiently induced by light with comparable energy to the bandgap of the doped material, and it is only weakly temperature dependent [75].

Interestingly, in the case of silver doped chalcogenide glass, if linearly polarized light is used for the dissolution then the sample will develop a strong dichroism with orientation opposite that of the silver free chalcogenide glass [10]. Therefore, the process can be said to be vectoral in nature. Also of note is that the chemical differences between the doped and undoped glass, as well as the ability to control doping with light have led to investigations of applications in photolithography [74, 76].

## 3.7 Photoinduced Anisotropy

Glasses and amorphous materials are inherently isotropic and chalcogenide compounds are no exception; however, Zhandov et al. [12] was the first to discover that chalcogenide materials can be made anisotropic by irradiating them with polarized light. The material

will then exhibit different properties for different polarizations of incoming light. The most notable of these vectoral effects are referred to as photoinduced dichroism (PDi) and photoinduced birefringence (PBi).

Dichroism refers to the selective absorption of two orthogonal linearly polarized states of a beam light. In these materials there exists what is known as a transmission axis. When incoming light is incident on the material, light polarized in the same direction as the transmission axis will pass through the material; meanwhile, light polarized along the orthogonal direction will be heavily absorbed. A schematic of the process is shown in Figure 3-4.

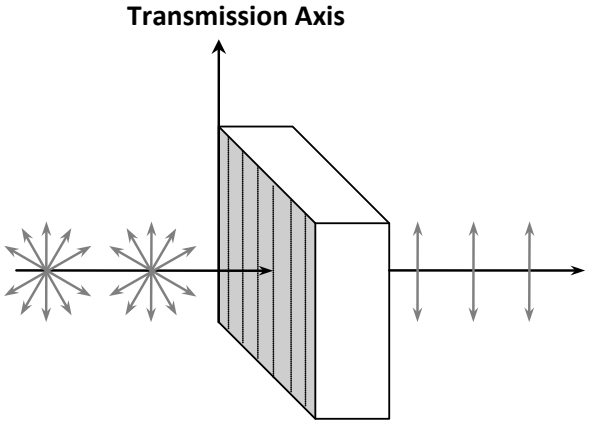


**Figure 3-4: Illustration of the absorption of light when passing through a dichroic material. An unpolarized light source is incident on the material and light polarized along the transmission axis passes through, while light polarized in any other direction is heavily attenuated.**

Birefringent materials have more than one refractive index, each of which depends on the polarization, and direction of propagation, of the incoming light. Birefringence is shown in Figure 3-5, where it is illustrated that any unpolarized light entering the material will be split into two rays. Each ray will have a different polarization and a different propagation velocity resulting in a phase difference between two orthogonal polarizations, as shown in Figure 3-5 (a). Figure 3-5 (b) demonstrates the case where the incoming beam is along the optic axis, in which case there is no phase change and the emerging beam is a replica of the incoming beam.

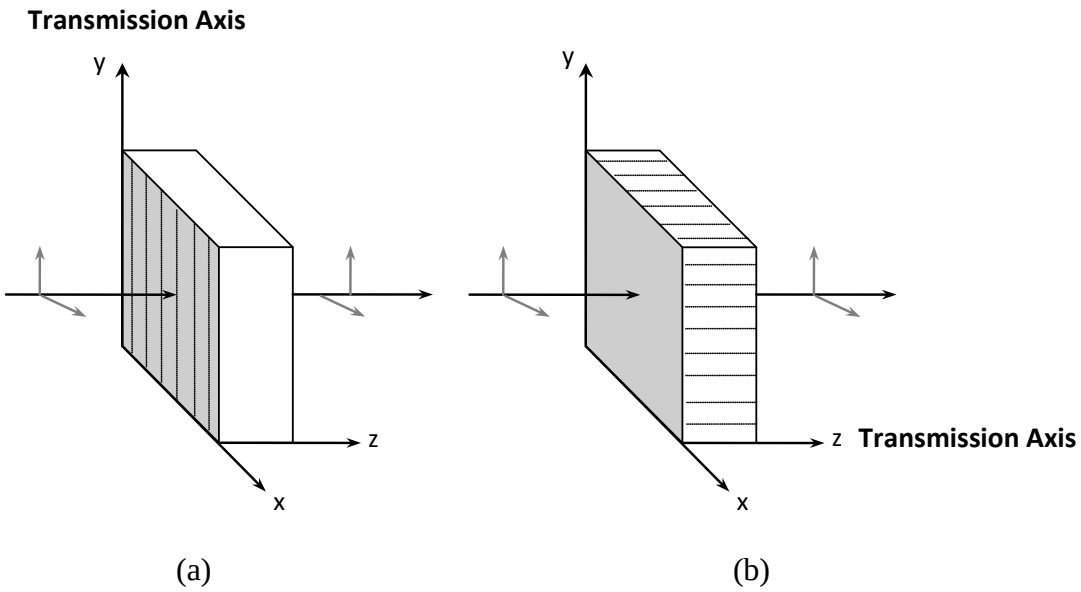


**Figure 3-5: Illustration of the passage of light through a birefringent material. (a) A phase difference between orthogonal polarizations is introduced when transmission is not along the transmission axis. (b) There is no phase difference when propagation is along the transmission axis.**

As stated previously, chalcogenide materials can be made anisotropic by irradiating them with polarized light, the result is reversible PDi and PBi. The dichroism can be induced and subsequently reversed hundreds of times without any sign of fatigue [77]. Similar to PD and photorefraction, PDi and PBi accompany one another and are simultaneously induced with either linearly or circularly polarized light. In the case of circularly polarized light the anisotropy is generally referred to as photoinduced gyrotropy [78]; however, in this thesis we will take PDi to mean photoinduced linear dichroism. Both PDi and PBi are metastable [39] and reversible, because any induced anisotropy can be erased by annealing above $T_g$ [40, 12].

## 3.8 Existing Models

Since the discovery of photoinduced anisotropy by Zhandov et al. [12] over 25 years ago, there has been extensive research into understanding the structural elements responsible for those changes. To date there is no clear consensus between research groups regarding the microscopic mechanisms responsible for the phenomena. The following section

introduces some of the more commonly referred to models which attempt to explain the effects.

Currently all of the models use microscopic mechanisms occurring at the atomic level to describe the measured macroscopic effect. The main reason for the lack of consensus between researchers arises from the fact that there is no way to directly measure the microscopic events. In general, we take a chalcogenide sample and irradiate it with light which is comparable to the bandgap of the sample, an inducing photon is absorbed by the material and generates an electron-hole pair that recombine non-radiatively. The local distortion of the lattice from the absorption of the phonon energy is dependent on the polarization of the inducing photon, along with some asymmetric structural units. The result is a change in the local bonding giving rise to a local anisotropy. Amorphous materials, having an inherently flexible lattice, permit the local anisotropy to spread throughout the network ultimately leading to a macroscopic photoinduced anisotropy effect. The asymmetry of these local structural elements must be sensitive to the electric field of the inducing light, or the polarization. Absorption would also depend on the parallel orientation of the photon polarization and the local element's optical axis. Many researchers agree on the general description given above; however, the disagreement stems from the interpretation of the underlying mechanisms which cause those events.

In most models the local structural elements responsible for the anisotropy are intimate valence alternation pairs (IVAP's). As previously discussed in Chapter 2, these charged defects exist naturally in chalcogenides. The idea of the IVAP being responsible for the photoinduced anisotropy mechanisms was first proposed by Lyubin and Tikhomirov [79]. That model was then further developed by Elliot and Tikhomirov for pnictogen (eg. As) and chalcogen (eg. Se) system [80]. As shown in Figure 3-7, the model consists of a pyramidal structure formed by a pnictogen and three chalcogenide atoms that contain an IVAP. They proposed geminate recombination where an electron is expelled from a $C_1^-$ (or a hole from a $C_3^+$) and is trapped by a $C_3^+$ (or $C_1^-$ respectively) of the same IVAP. The result is a transformation of the IVAP from $C_3^+C_1^-$ into $C_1^-C_3^+$. This progression is

consistent with intensity dependence data that suggests typically a single photon process is involved. Elliot and Tikhomirov propose this to be a two step process. The first step involves the creation of singly and threefold coordinated neutral centers, $C_1^- C_3^+ + h\nu = C_1^0 C_3^0$, via a single photon. In the second step the neutral centers thermally decay back to the stable charged centers $C_1^- C_3^+$, shown in the top of Figure 3-7, or $C_3^+ C_1^-$ shown in the bottom of Figure 3-6. A macroscopic change results in the glass structure where the inducing light polarization is perpendicular to the IVAP lone pair orientation. The model also accounts for photoinduced gyrotropy (circular polarization) since mirror images of the pyramidal structures have opposite magnetic dipole moments for optical transitions.

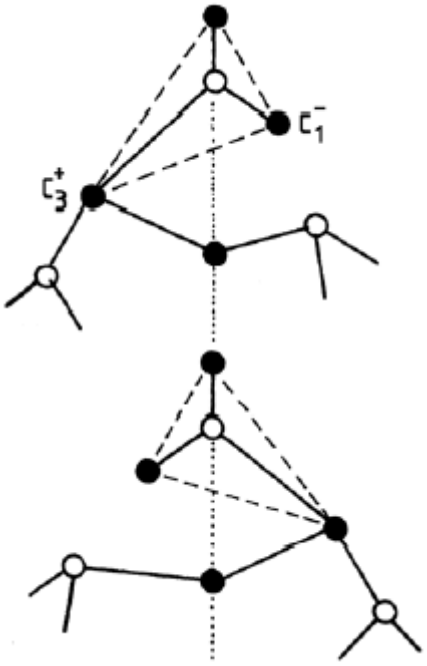


**Figure 3-6: Illustration of the model responsible for photoinduced anisotropy in a pnictogen-chalcogen system, proposed by Elliot and Tikhomirov. The top figure is before excitation and the bottom figure is after. The open circles denote pnictogen atoms and the solid circles represent the chalcogen atoms. Note that they exaggerated the extension of the $C_3^+$ bond for clarity [80].**

To explain the temperature effects of photoinduced anisotropy Tikhomirov, Adriaenssens and Elliot [81] developed a similar model that was also based on VAP's. The model is shown in Figure 3-7, and it uses the bonding structure of an elemental Chalcogenide

material. It can be easily extended to a pnictogen-chalcogen system, such as the compound we used ($As_2Se_3$), by placing an As atom on the $C_2^0$ positions. In order to produce a flip in the pyramidal structure an electron is optically excited from the $C_1^-$ atom and subsequently trapped in an anti-bonding orbital localized around the $C_3^+$ atom. This is shown as a dotted circle around the $C_3^0$ atom in Figure 3-7 (b). The authors go on to say that this produces a flexible transient pyramid state consisting of $C_3^0C_1^0C_2^0C_2^0$ atoms for three reasons: (1) the anti-bonding electron weakens the bonds of the $C_3^0$ atom, (2) the $C_1^0$ atom has only one (weakened) bond and no electrostatic forces like in the $C_3^+C_1^-$ case, and (3) a void should exist near the $C_1^-$ atom before excitation to account for its single fold coordination. From this transient excited state, thermal energy can cause the pyramid to flip resulting in the $C_3^0$ atom to move to the mirror image position $C_{3m}^0$ in Figure 3-7 (b). To maintain the lowest possible energy state the $C_1^0C_{3m}^0$ pair would de-excite to the arrangement shown in Figure 3-7 (c). In order to account for low temperatures the $C_3^0$ atom has the possibility to tunnel through the $C_2^0C_1^0C_2^0$ plane, given by the shaded region in Figure 3-7 (b), to the mirror image position $C_{3m}^0$ and subsequently de-excite to the arrangement shown in Figure 3-7 (c). In that case Figure 3-7 (c) represents an IVAP bond that is orthogonal to the polarization of the inducing light; therefore, minimizing the energy between the IVAP dipole and the electric field of the inducing beam.

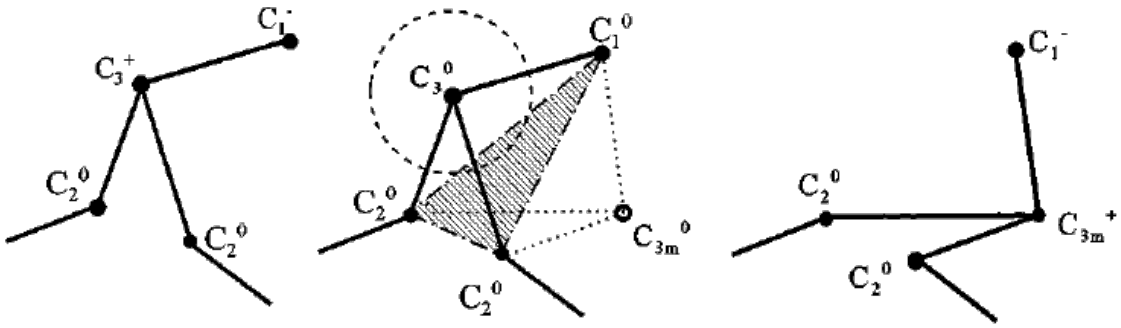


(a) (b) (c)

**Figure 3-7: Proposed anisotropy model with an IVAP centered at $C_3^+$. The configuration is (a) before optical excitation, (b) the transient state after optical excitation and (c) the reoriented metastable IVAP [81].**

In the model that Fritzsche proposes [82, 83, 84], the concept of anisotropic microvolumes is used to explain a variety of photoinduced anisotropic effects. The model not only accounts for the sign of the anisotropy, it also predicted that an unpolarized light beam could cause anisotropy in these materials, a prediction later confirmed by Tikhomirov and Elliot [85]. It should be noted that in the model proposed by Fritzsche the microvolumes are based on IVAP's [82, 83]; however, they are not the only anisotropic entities. He notes that all transitions are polarization dependent including; optical, inter-band, Urbach tail, and defect transitions. He also stresses that there is no lower threshold of light intensity for producing photoinduced anisotropic effects as the action of light is cumulative.

Fritzsche grouped the anisotropic microvolumes into three categories $v_{ix}$, $v_{yj}$, and $v_{kz}$. The reason for the grouping was to represent the three directions *x*, *y*, and *z*, that would have the largest cross sectional absorption for inducing light polarizations. He separately summed the three microvolumes belonging to each category to obtain the average absorption coefficients for each direction.

$$\overline{\alpha_x} \approx \sum_{i=1}^{N_x} \frac{\alpha_{ix} v_{ix}}{V_{tot}}, \overline{\alpha_y} \approx \sum_{i=1}^{N_y} \frac{\alpha_{jy} v_{jy}}{V_{tot}}, \text{ and } \overline{\alpha_z} \approx \sum_{i=1}^{N_z} \frac{\alpha_{kz} v_{kz}}{V_{tot}} \tag{3.1}$$

where $N_x$ is the number of microvolumes of $v_{ix}$ type, $\alpha_{ix}$ is the absorption coefficient for light polarized along the *x*-axis, and $V_{tot}$ is the total volume of the material. The relationships are approximate because some small contributions are neglected, such as $\overline{\alpha_x}$ from the absorption of the $v_{yj}$ and $v_{kz}$ microvolumes. Since the glass is initially isotropic,

$$\overline{\alpha_x} \approx \overline{\alpha_y} \approx \overline{\alpha_z} \tag{3.2}$$

The smaller the anisotropic microvolumes that are chosen, the more accurate Equation 3.1 and Equation 3.2 will be. The initially isotropic material demands that,

$$N_x = N_y = N_z = \frac{1}{3} N \tag{3.3}$$

where *N* is the total number of anisotropic microvolumes.

After the absorption of bandgap light the following processes can take place: (a) there is redistribution with no net change $\Delta N_x + \Delta N_y + \Delta N_z = 0$, (b) bleaching $\Delta N < 0$, (c) creation $\Delta N > 0$, or (d) electron and hole diffusion.

If we assume that a light wave linearly polarized along the *z*-axis is traveling in the *y*-direction as shown in Figure 3-8 (a), then an absorption process will take place in the $v_{kz}$ element. There are two possible outcomes resulting from the local structural change that will take place due to the recombination. Either the anisotropy of the microvolume will change or it will be left intact. The former is the interesting result as it causes a loss of that particular absorption element for the *z* polarization. Now, either bleaching took place or the anisotropy was altered so that only the *x* and *y* polarization are absorbed. The latter instance leads to a redistribution of of the microvolumes such that $-\Delta N_z = \Delta N_x + \Delta N_y$. The collective effect of the redistribution events is the reduced absorption of light polarized parallel to the inducing polarization, and an equally increased absorption of the two orthogonal directions, $-\Delta\alpha_z = \Delta\alpha_x + \Delta\alpha_y$. The dielectric tensor is then an ellipsoid of revolution with the optical axis in the *z* direction, while the absorption coefficients are $\alpha_z < \alpha_x = \alpha_y$ and the refractive indices are $n_z < n_x = n_y$ (see Figure 3-8 (a)).

The prediction that unpolarized light would produce optical anisotropy is illustrated in Figure 3-8 (b). The unpolarized light source is traveling in the *y* direction which yields absorption in the microvolumes corresponding to the *x* and *z* polarizations only. The outcome of the redistribution is then a decrease in the absorption for *x* and *z* polarizations and an increase in absorption for the *y* polarization. In this case the dielectric tensor is an ellipsoid of revolution with the axis in the direction of propagation. For example, it would be the y direction as shown in Figure 3-8 (b), where the absorption coefficients become $\alpha_z = \alpha_x < \alpha_y$ and the refractive indices are $n_z = n_x < n_y$. This was later confirmed experimentally by Tikhomirov and Elliott [85]. Their results demonstrated that the glass appeared to be isotropic for light traveling along the direction of propagation (*y* axis in Figure 3-8 (b)) of the inducing beam, but the anisotropy was

observed for light propagating in either of the two orthogonal directions (*x* or *z* axis in Figure 3-8 (b)).

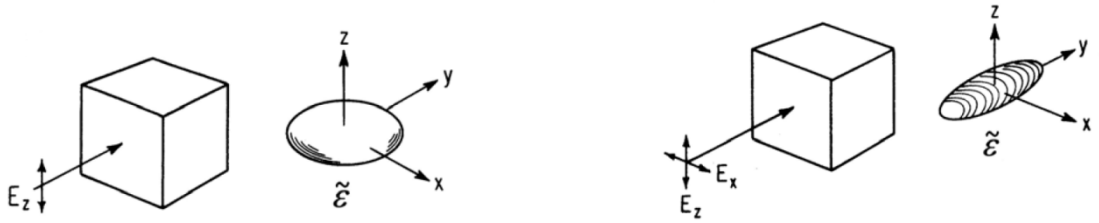


(a) (b)

**Figure 3-8: Schematic illustration of Fritzsche model for photoinduced anisotropy in Chalcogenide glasses. The figure shows the dielectric tensor $\tilde{\varepsilon}$ (a) after irradiation with linearly polarized light, and (b) after irradiation with unpolarized light [84].**

## 3.9 Summary

This chapter presented a discussion of the various photoinduced effects that may occur in chalcogenide materials. The changes discussed in detail were all metastable; however, distinctions were made between reversible and irreversible, as well as scalar and vectoral processes. Each effect was outlined in detail with the focus being on the vectoral photoinduced anisotropy. Finally, the chapter was concluded with brief overview of the currently existing models which attempt to explain the photoinduced changes, specifically photoinduced anisotropy.

# Chapter 4 Experimental Apparatus

## 4.1 Introduction

The following chapter outlines the entire experimental apparatus and highlights each of the components involved in the measurement system. First, a full description of the entire apparatus, how it functions, and the components that are involved is given. Second, the light sources are described in detail. Lastly, the electronics and data acquisition system are described.

## 4.2 Anisotropy Measurement Apparatus

A schematic of the system used to measure photoinduced dichroism is shown Figure 4-1 and an aerial view of the actual apparatus is shown in Figure 4-2. The schematics show anisotropy being induced by a linearly polarized HeNe laser with an inducing wavelength of 632.8 nm; however, a red laser diode with a wavelength of 658 nm was also used to irradiate the thin films. When the laser diode was being used it was placed in front of the HeNe laser, approximately 10 cm closer to the sample, and the convex lens directly in front of the HeNe laser was no longer necessary.

The schematics in Figure 4-1 and Figure 4-2 also demonstrate that there are two light sources incident on the sample. The irradiating source is the HeNe laser which first passes through an ordinary convex lens. The lens is introduced so that the laser beam can be expanded from an initial waist of 1.1 mm (FWHM) to approximately 3.4 mm at the sample. A variable neutral density filter was employed to facilitate pump intensity adjustments. Monitoring the pump intensity was done by placing a glass microscope slide into the path of the laser as a partial reflector. That partially reflected portion of the laser beam was measured using the AUX #2 A/D converter in the lock-in amplifier via the pump power photodetector. The ratio of the reflected (sampled) to inline inducing intensity was measured to be approximately 37%. Next, the inducing beam passed through a calibrated polarizer that could be adjusted to provide laser light at the sample that was either vertically polarized or horizontally polarized.

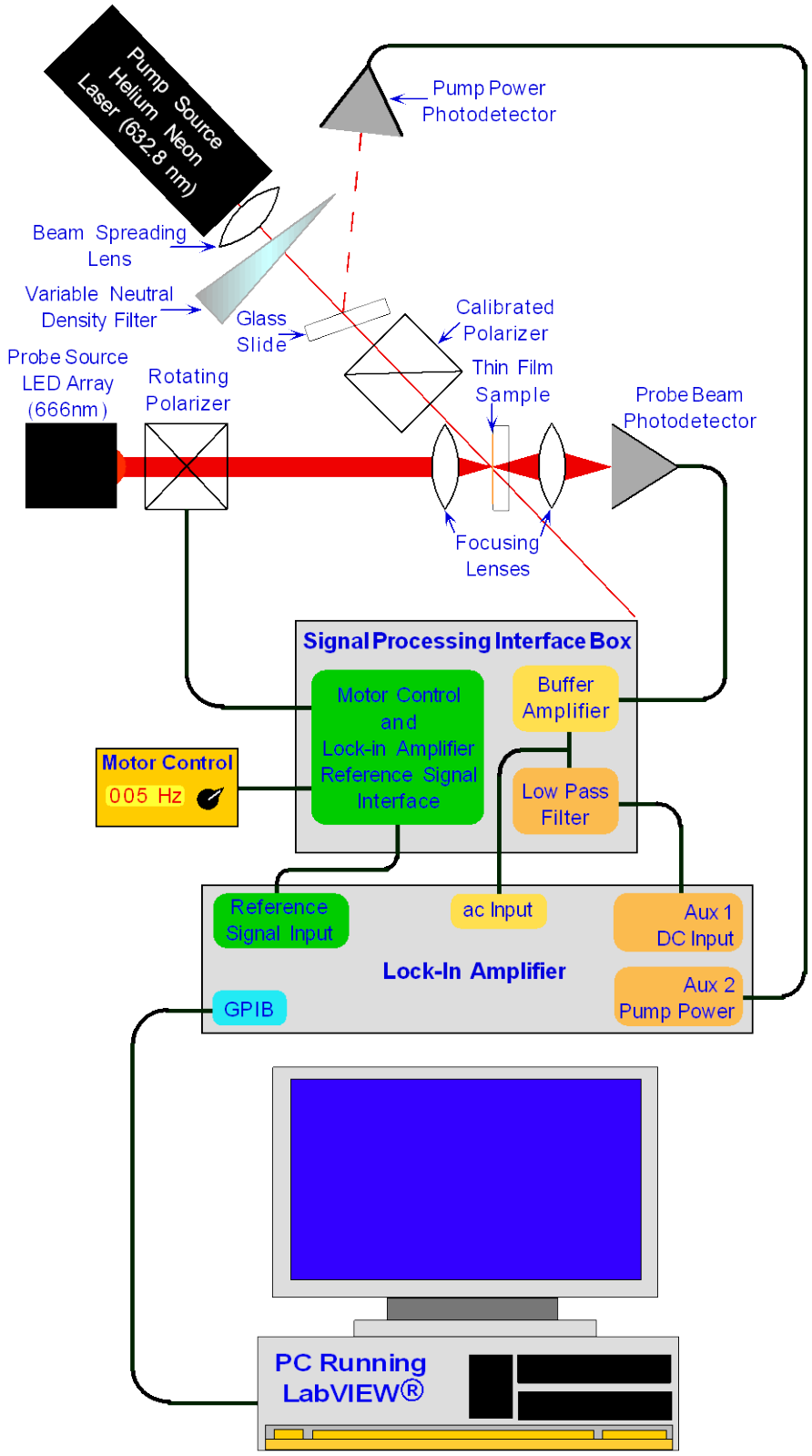


**Figure 4-1:** **Schematic diagram of the experimental measurement system used to measure photoinduced dichroism.**

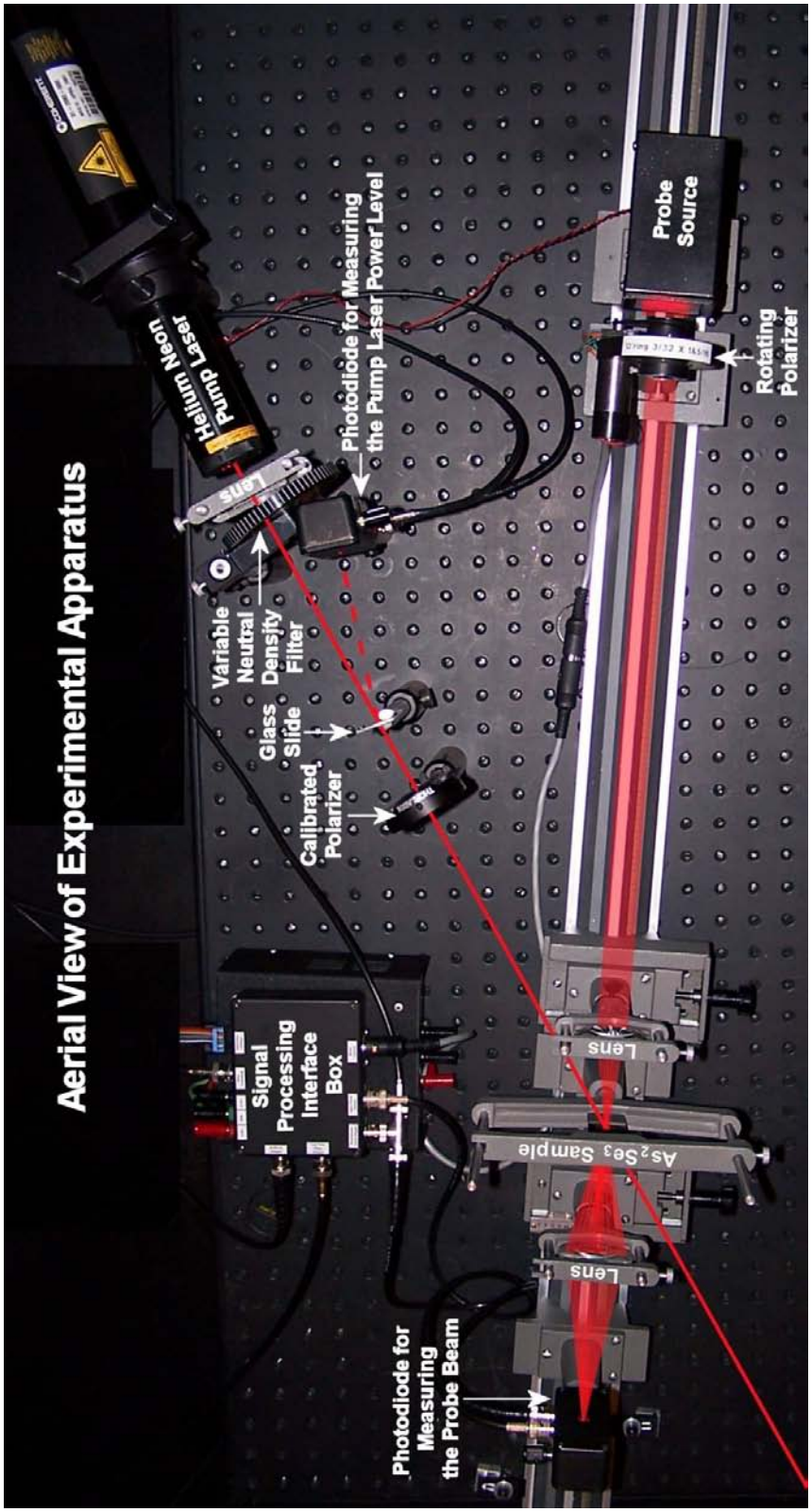


**Figure 4-2:** **Aerial view of the actual experimental apparatus. Beam lines (red) have been added for clarity.**

The other light source that was incident on the sample was the unpolarized probe source. The unpolarized probe beam was created from an array of red LEDs (666 nm) shining through a piece of frosted glass, that was then passed through a rotating polarizer with a frequency of 5 Hz. Light coming out of the rotating polarizer was focused onto the sample by a convex lens to a spot size of approximately 1.70 mm. Essentially the probe beam was a linearly polarized beam with a polarization that rotates at 10 Hz (fundamental frequency 'f').

After the probe beam passed through the sample it was refocused onto a photodiode detector. The resulting electrical signal consisted of two portions, a dc level and a second harmonic component. In order to obtain those two components the signal was sent to the lock-in amplifier via a buffer amplifier to extract the $2^{nd}$ harmonic ($2f$) portion of the signal; meanwhile, the signal was also sent through a low pass filter and then an A/D converter in the lock-in amplifier in order to extract the dc portion. The reference signal at frequency $f$ for the lock-in amplifier was generated by an optical sensor on the rotating analyzer. Finally, a computer running a LabVIEW® program recorded the lock-in amplifier readings every 5 seconds via a GPIB connection.

## 4.3 Light Sources

### 4.3.1 Probe Light Source

The ideal probe beam for this experiment would be from a completely unpolarized light source; however, it is very difficult, if not impossible, to produce completely unpolarized light. There are several types of sources which one would expect to be unpolarized such as; halogen lamps, incandescent light bulbs, various types of LEDs. In fact, all of those sources have at least some small amount of polarization [86]. That means that there is no selection of probe source which will be completely unpolarized. The small amount of polarization present will need to be accounted for and subtracted from the analysis.

The probe source that was used for this study was produced by an array of nineteen red LEDs ($\lambda \cong 666$ nm) shinning through frosted glass to help scatter the light, reducing the

residual polarization, as shown in Figure 4-3. The source of LEDs produced light with approximately 0.95 % polarization, a central wavelength (λ) of approximately 666 nm, and a maximum intensity at the sample of $13.6 \mu W / mm^2$ [86].

(a) (b)

**Figure 4-3: (a) Entire probe light assembly with housing and frosted glass in place. (b) Probe light LED array.**

At that intensity the probe source had a negligible effect on the photoinduced dichroism. Even though the probe beam intensity was sufficiently lower than that of the inducing beam fluctuations in that intensity were not tolerable. It was determined that throughout the course of a measurement the probe beam intensity deviated by as much as five percent. These changes in intensity could be attributed to temperature sensitivity of the LED array and driving electronics as well as aging of the LED's. Any fluctuation in the intensity results in a shift in the measured quantities due to the fact that the both the phase angle and the *2f* signal are directly proportional to the dc level (which essentially represents the intensity of the probe beam).

The fluctuating probe beam intensity was stabilized by introducing the feedback circuit shown in Figure 4-4. The feedback circuit used a Hamamatsu S2386-8K silicon photodiode, selected because of its low temperature sensitivity, to first monitor the output of the LED array. Any changes in the output of the photodiode caused the circuit to adjust the current through the LED array. Fluctuations in intensity were compensated for by current adjustment; therefore, creating an intensity stabilized diode array which had daily variations in intensity of less than 1%.

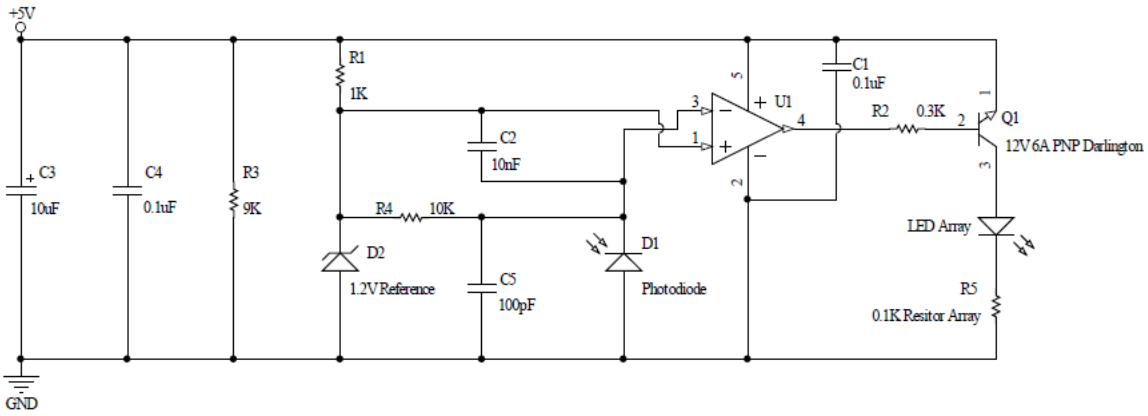


**Figure 4-4: Probe source intensity stabilization circuit.**

## 4.3.2 Helium Neon Laser

Selection of a excitation source was based on three criterions: (1) the intensity of the excitation source must be sufficient to induce dichroism within a reasonable time frame; (2) the excitation intensity must be sufficiently larger than that of the probe beam to ensure the negligible effect of the probe; (3) the excitation wavelength must be such that the pump beam can be sufficiently absorbed. According to those criteria one of the excitation sources chosen for this work was a 30 mW (maximum) linearly polarized Helium Neon (HeNe) laser manufactured by Coherent Inc. (model number 31-2082-000).

The HeNe laser was most attractive because its lasing emission occurs at approximately 632 nm, a wavelength that lies directly on the absorption edge of $As_2Se_3$ (see Figure 4-5). Excitation wavelengths on the absorption edge result in nearly 50% absorption; therefore, providing an excitation source that is sufficiently absorbed to provide more or less uniform PDi throughout the thickness of the sample. The intensity of the laser was sufficient to induce dichroism in anywhere from 15 minutes to 12 hours depending on the thickness of the sample. Any measurements at decreased pump intensities, where a neutral density filter was placed in front of the laser, still involved intensities sufficiently larger than that of the probe beam. The HeNe laser provided enough intensity for the production and measurement of photoinduced dichroism in thin films.

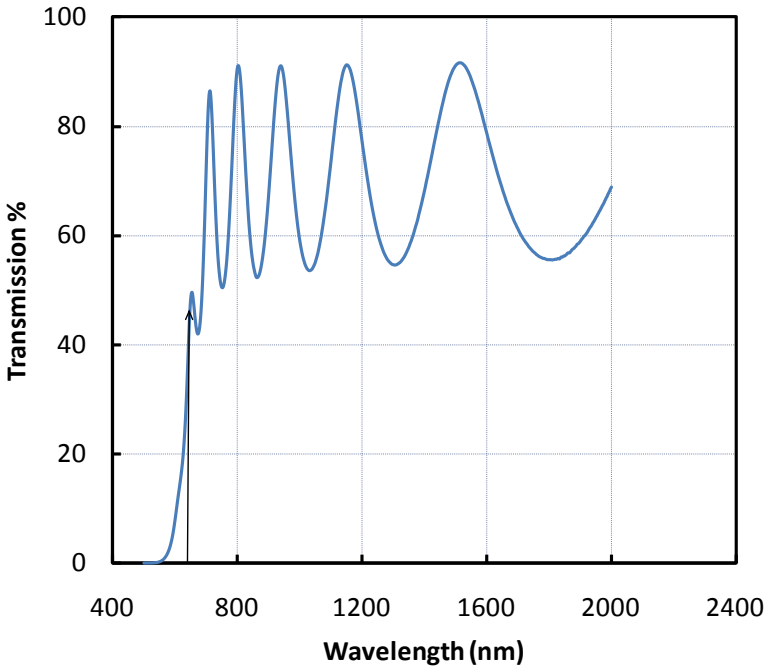


**Figure 4-5: Spectral response of a 0.8 µm thick $As_2Se_3$ thin film as obtained by using the method developed in (87) using the Lamda 800/900 spectrometer.**

The beam profile of HeNe laser, as with most gas lasers, was a Gaussian (see Figure 4-6); however, the angle of incidence and the polarization state of the laser somewhat complicate the profile. The actual beam profile of a HeNe laser has both horizontal and vertical components, and there would be a Gaussian profile in two directions each having a different value of the parameter σ. If we consider the case where the Gaussian is symmetric then the intensity is given by

$$I = I_0 e^{\frac{-\left(x^2+y^2\right)}{2\sigma^2}} \tag{4.1}$$

Mathematically, the power is the area under the curves formed in both the *x* and *y* directions, which is an integral of the form

$$P = I_0 \int_{-\infty}^{\infty}\int_{-\infty}^{\infty} e^{\frac{-\left(x^2+y^2\right)}{2\sigma^2}}\, dxdy \tag{4.2}$$

The average intensity is simply the power per unit area

$$I = \frac{P}{2\pi\sigma^2} \tag{4.3}$$

In order to determine the intensity the power can be easily measured via a photodetector, while the parameter σ is dependent on the polarization state of the laser. It was measured in [86] that for vertical polarization $\sigma = 0.550mm$ and for horizontal polarization $\sigma = 0.535mm$.

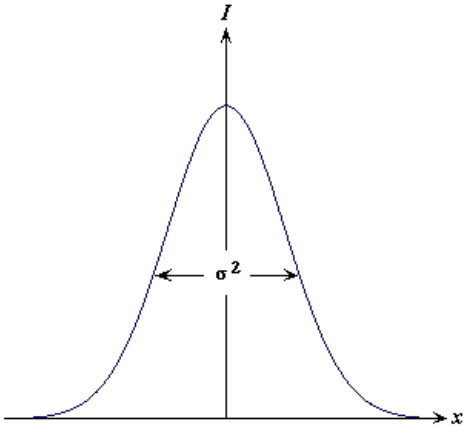


**Figure 4-6: Standard Gaussian profile in one dimension (*x*-direction).**

As shown in Figure 4-7 the laser emission is not orthogonal to the sample, but at an angle of 32.4° (found from the measurements shown in Figure 4-7); therefore, only a fraction of the intensity at the surface of the sample is actually transmitted into the sample. Fresnel's equations [88] must be used to determine the reflectance and transmittance of the sample as a function of the angle of incidence and the refractive index of the material. The equations relate the transmitted and reflected amplitudes of an electromagnetic wave traveling from one medium of refractive index $n_1$ to another medium of refractive index $n_2$. There are separate equations for each polarization state of the electromagnetic wave, which are given by

$$r_{//} = \frac{\sqrt{n^2 - \sin^2(\theta_i)} - n^2 \cos(\theta_i)}{\sqrt{n^2 - \sin^2(\theta_i)} + n^2 \cos(\theta_i)} \tag{4.4}$$

and

$$r_{\perp} = \frac{\cos(\theta_i) - \sqrt{n^2 - \sin^2(\theta_i)}}{\cos(\theta_i) + \sqrt{n^2 - \sin^2(\theta_i)}} \tag{4.5}$$

where

$$n = \frac{n_2}{n_1}$$

The reflectance for each polarization are defined as

$$R_{HP} = \left| r_{//} \right|^2 \tag{4.6}$$

and

$$R_{VP} = \left| r_{\perp} \right|^2 \tag{4.7}$$

Which in turn yield the transmittance of a vertically polarized beam

$$T_{HP} = 1 - R_{HP} = 1 - \left| r_{//} \right|^2 = 1 - \left| \frac{\sqrt{n^2 - \sin^2(\theta_i)} - n^2 \cos(\theta_i)}{\sqrt{n^2 - \sin^2(\theta_i)} + n^2 \cos(\theta_i)} \right|^2 \tag{4.8}$$

and the transmittance of a horizontally polarized beam

$$T_{VP} = 1 - R_{VP} = 1 - \left| r_{\perp} \right|^2 = 1 - \left| \frac{\cos(\theta_i) - \sqrt{n^2 - \sin^2(\theta_i)}}{\cos(\theta_i) + \sqrt{n^2 - \sin^2(\theta_i)}} \right|^2 \tag{4.9}$$

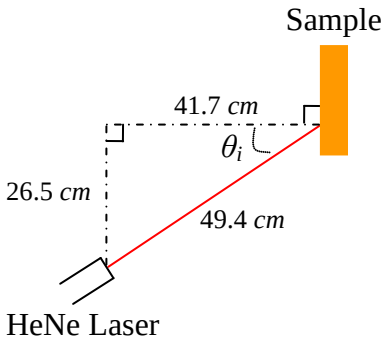


**Figure 4-7: Schematic demonstrating the angel of incidence of the HeNe laser beam with respect to the sample.**

In the case of our experimental setup we have an electromagnetic wave traveling through air ($n_1 = 1$) incident on a sample of refractive index $n_2$. The refractive index of $As_2Se_3$ is wavelength dependent and can vary from sample to sample. It can be determined by employing the method developed in [87] along with spectral data obtained using the Lambda 800/900 spectrometer. The refractive index of $As_2Se_3$ may also be found by the method in [89] which yields,

$$n_{As_2Se_3} \cong 3.016$$

Combined with an angle of incidence of 32.4°, the horizontal and vertical transmittances for $A_2Se_3$ are

$$T_{HP} = 80.42\% \qquad T_{VP} = 68.97\%$$

It is assumed that the addition of small amounts of iodine to the samples would have a negligible effect on the refractive index; therefore, the transmittances shown for $As_2Se_3$ were used when analyzing the iodine doped samples. It is also of note that only the real part of the refractive index was used in the above calculations. The imaginary part of the refractive index can be ignored as it accounts for less than 5% of the total for the wavelengths of interest [9].

The HeNe laser was a very effective excitation source for most sample measurements; however, it had several drawbacks. The power output of the laser was limited, especially due to the fact that an external polarizer was necessary which only served to diminish the number of photons incident at the sample. Its large size proved to be difficult to incorporate into the experiment, and it only produced one wavelength. These problems were eliminated by employing laser diodes which will be described in the next section.

### 4.3.3 Laser Diodes

Laser diodes are relatively inexpensive devices capable of large power output in very compact cases. The small compact nature of the laser diodes allowed for the creation of a laser diode holder which could be computer controlled by LabVIEW® via the parallel port of a PC. That interface allowed for greater flexibility in the measurement cycles as well as conserved laser power by eliminating the necessity of an external polarizer. The large power output of the diodes allowed for a greater range of thicknesses and intensities to be incorporated into the measurement sets.

The laser diode used in this work was a 658 nm UH5-50GC-658 purchased from World Star Tech. The laser had an adjustable circularized output beam with output power up to 50 mW. The 658 nm diode had an output wavelength very close to that of the HeNe laser;

therefore, it could be used to extend previous intensity data to higher incident intensities as well as deliver information on thicker samples.

In order to incorporate the laser diode into the existing experimental setup a holder, shown in Figure 4-8, was fabricated. The holder was capable of not only aligning the laser diode, but also rotating the diode about a specific axis. The ability to rotate the laser diode eliminated the need for an external polarizer because varying the polarization state of the inducing beam was simply accomplished by rotating the laser diode itself.

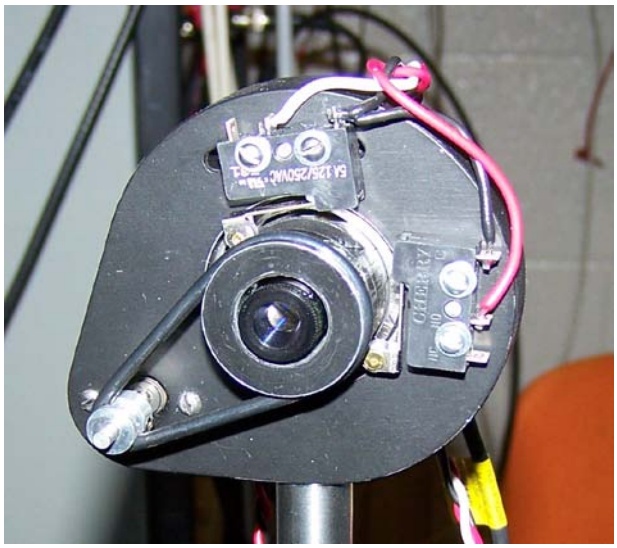

**Figure 4-8: Laser diode holder.**

Rotational control of the laser diode was provided by a LabVIEW® program running on a PC connected to a control circuit via the parallel port. The program allowed for timed control of the measurement intervals as well as the rotation of the laser diode. The control circuit and its associated logic circuit are shown below in Figure 4-9 and Figure 4-10.

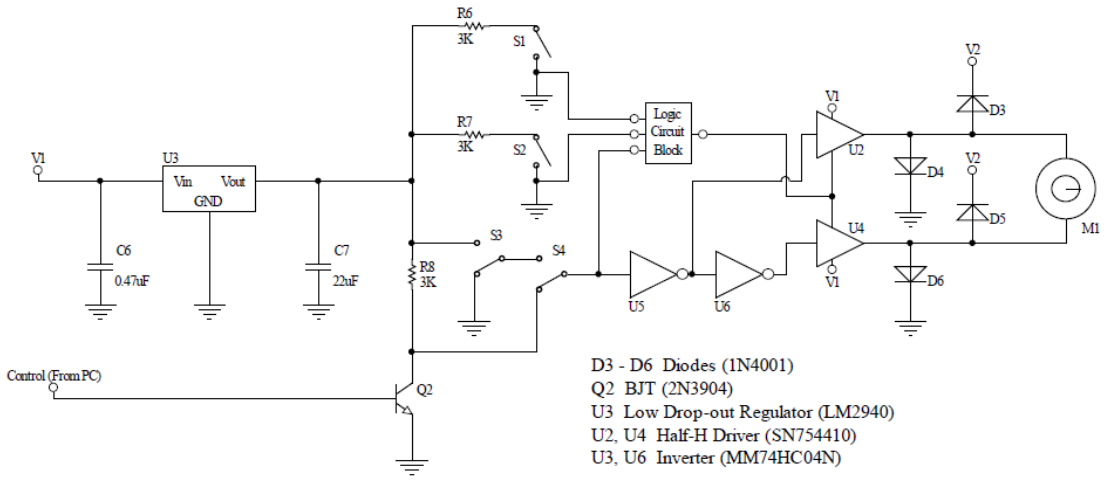


**Figure 4-9: Laser diode holder control circuit.**

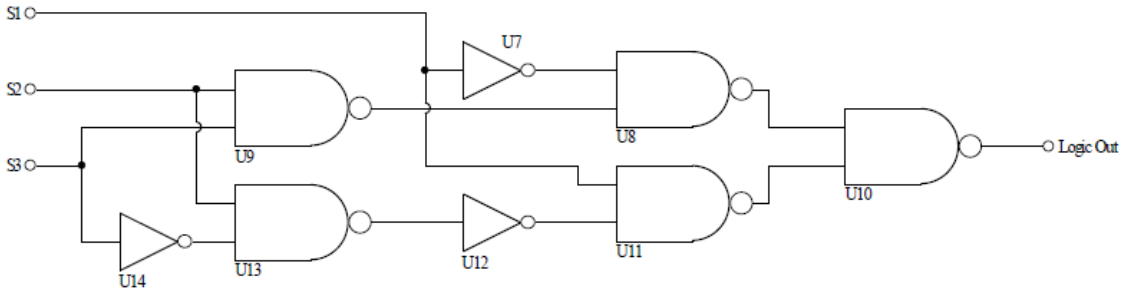


**Figure 4-10: Logic circuit block for the laser diode holder control circuit.**

## 4.4 Electronics and Data Acquisition

### 4.4.1 Rotating Analyzer

The rotating analyzer, shown in Figure 4-11, was an integral part of the experimental setup as it served two main functions; it was the means by which the rotating polarized pump beam was created, and it provided the reference signal for the lock-in amplifier. The rotating analyzer was constructed by the in house machine shop in the College of Engineering, because a unit that rotated fast enough was not commercially available. As shown in Figure 4-11 the analyzer housing is rotated by an O-ring belt driven by a DC motor (made by Escap – model number D21.213E.B2X2). Speed control for the DC motor was provided by an Oriel chopper controller via the signal processing interface box.

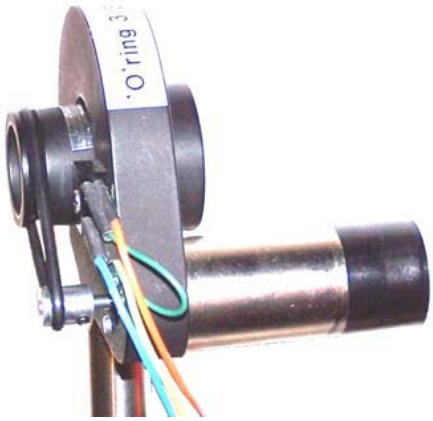


**Figure 4-11: Rotating analyzer side view showing the phototransistor and O-ring belt drive.**

The rotating analyzer is placed in front of the LED array to create a completely polarized beam with a polarization that rotates – this is a good approximation to an unpolarized probe light source. The rotating analyzer can rotate at any speed from 60 RPM to 600 RPM but has a lower limit that is determined by the chopper controller as its lowest frequency displayed is 1 Hz. Rotational feedback to the chopper controller as well as a reference pulse for the lock-in amplifier were provided by an Omron EE-SF5 reflective phototransistor and a piece of silver tape on the rotating cylindrical housing. At rotational speeds greater than 600 RPM the O-ring belt drive begins to slip on the motor pulley and subsequently the lock-in loses its phase lock with the reference signal. A frequency of approximately 5 Hz was selected for the rotating analyzer.

### 4.4.2 Detectors

There were two photodiodes employed in the experimental setup shown in Figure 4-1. One of the photodetectors measures the probe beam signal after it traverses the sample; meanwhile, the other detector monitors the inducing pump beam power level. The probe beam detector is a Hamamatsu S1336-BK silicon photodiode with a borosilicate glass window and an effective area of 33 $mm^2$. Meanwhile, the pump beam detector is a Hamamatsu S1223-01 silicon PIN photodiode with a borosilicate glass window and an effective area of 6.6 $mm^2$. The two detectors are housed in a die cast aluminum case which is spray-painted black to minimize reflections. Both detectors are reversed biased, as

shown in Figure 4-12, by a DC power supply. The photocurrent $I_{ph}$ is measured by way of $V_{OUT}$ across an appropriate selectable sensing resistor. The resistance value of each resistor, shown in Table 4-1, was determined using a GenRad Digibridge (model number 1657-9700) having an accuracy of 0.2%.

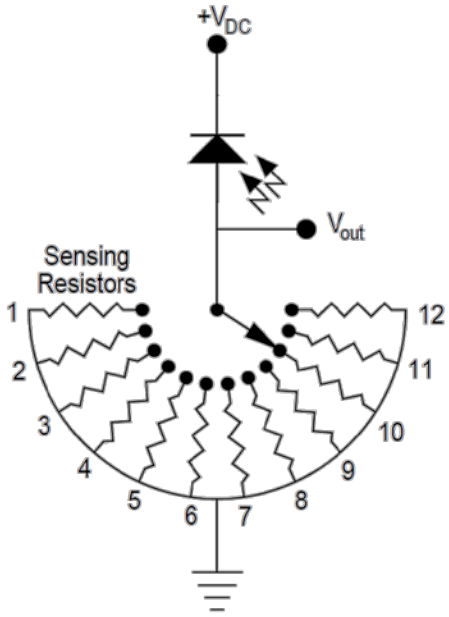


**Figure 4-12: Schematic of the photodetector biasing circuit.**

| Sensing Resistor Number | Detector S1336-8BK Sensing Resistor Value (Ω) | Detector S1223-01 Sensing Resistor Value (Ω) |
|---|---|---|
| 1 | 1003 | 1001 |
| 2 | 1999 | 1998 |
| 3 | 5010 | 5000 |
| 4 | 9980 | 9950 |
| 5 | 19980 | 19980 |
| 6 | 49800 | 49900 |
| 7 | 99900 | 999000 |
| 8 | 199900 | 201000 |
| 9 | 498000 | 502000 |
| 10 | 999000 | 998000 |
| 11 | 1993000 | 2130000 |
| 12 | 4990000 | 4490000 |

**Table 4-1: Sensing resistor values for both photodetectors obtained using a GenRad Digibridge (model number 1657-9700).**

The photodiodes, especially the probe beam detector, are responsible for measuring the changing polarization of light passing through the sample. Therefore, it was necessary to ensure that the detectors themselves were isotropic and not introducing some polarization into the measured signals. As a check the probe beam magnitude and phase were measured before and after a rotation of the detector by 90°. The result was that the two magnitudes and phases agreed within less than 1% indicating that the photodetectors did not introduce a measurable amount of polarization.

Photoinduced anisotropy experiments typically incorporated the effect of intensity on the level of the induced change. Any measurements concerning the effects of intensity on anisotropy require photodiode linearity. In order to perform the linearity check the intensity of the probe beam was varied starting first with an unfiltered beam, and subsequently decreasing the intensity with neutral density filters. A plot of photocurrent versus transmission should be linear, which is shown in Figure 4-13 for one of the detectors used.

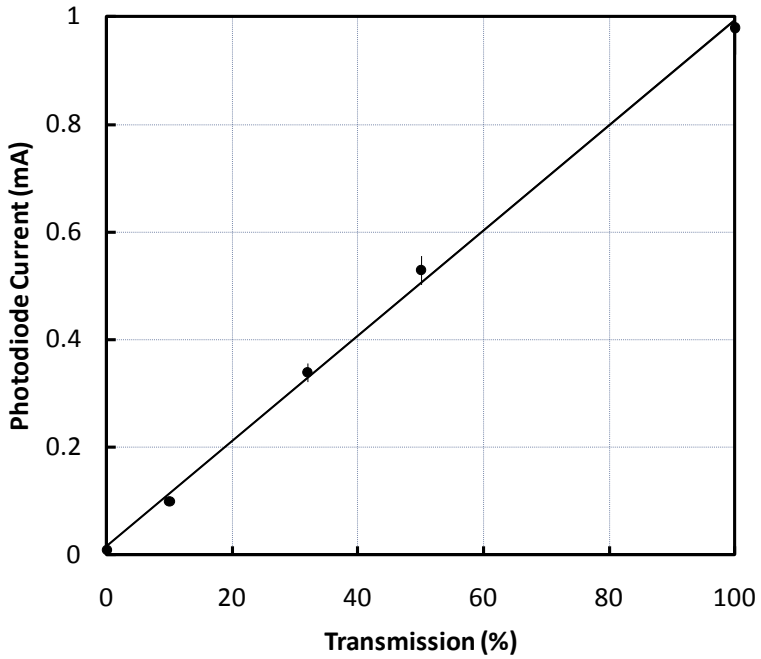


**Figure 4-13: Plot demonstrating the linearity of the Hamamatsu S1223-01 silicon PIN photodiode.**

## 4.4.3 Signal Processing Interface Box

The signal processing interface box houses the electronics that provide some signal routing and signal processing involved in the experimental setup. The box is divided into two sections. One side processes the signal from the probe detector; meanwhile, the other side interfaces the rotating analyzer motor with the chopper control and processes the reference pulse.

The probe detector signal processing circuit is shown in Figure 4-14. The probe beam for this experiment was specifically chosen to have a low intensity, thereby limiting its ability to cause photoinduced effects within the sample. That low probe intensity made signal detection more difficult as the sensing resistor at the detector required high impedance. To avoid the measurement equipment inadvertently loading the detector a buffer amplifier (U1) was placed between the detector and the signal processing circuit.

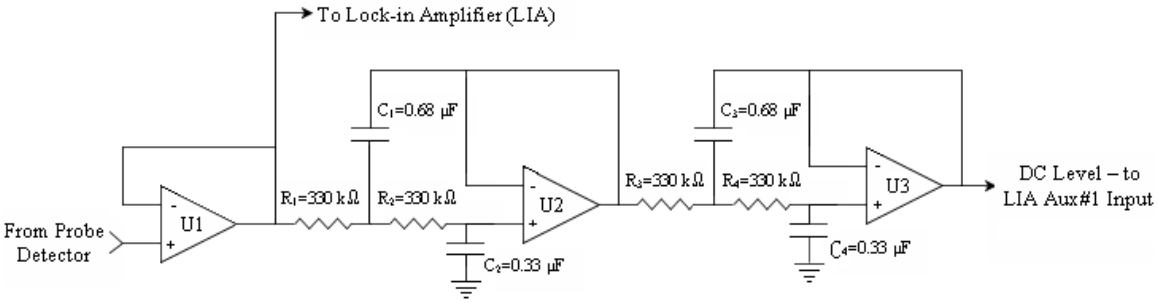


**Figure 4-14: Signal processing circuit for the probe detector signal.**

The output of the buffer amplifier was sent to the lock-in amplifier and to the low pass filter circuit. The portion sent to the lock-in amplifier contained the magnitude and phase of the ac signal measured by the detector and the lock-in amplifier was set to extract the magnitude and phase of the *2f* signal. A Sallen-Key topology low pass filter circuit with unity gain was used to strip off the ac signal in order to obtain the DC level at the detector. The magnitude of the ac signal was much less than that of the DC level, typically greater than 40 dB lower, so a fourth order low pass filter with a cutoff frequency at 1 Hz attenuated the ac signal to greater than 70 dB less than the DC level. The frequency response of the filter, shown in Figure 4-15, demonstrates that there was sufficient

difference between the two signals to ensure the DC level measurement was not disturbed by the ac signal.

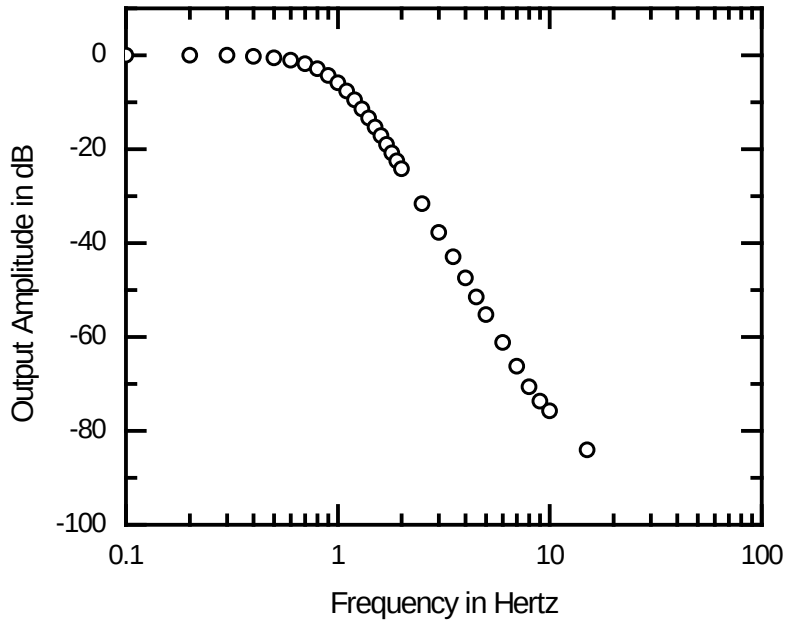


**Figure 4-15: Frequency response of the unity gain low pass filter.**

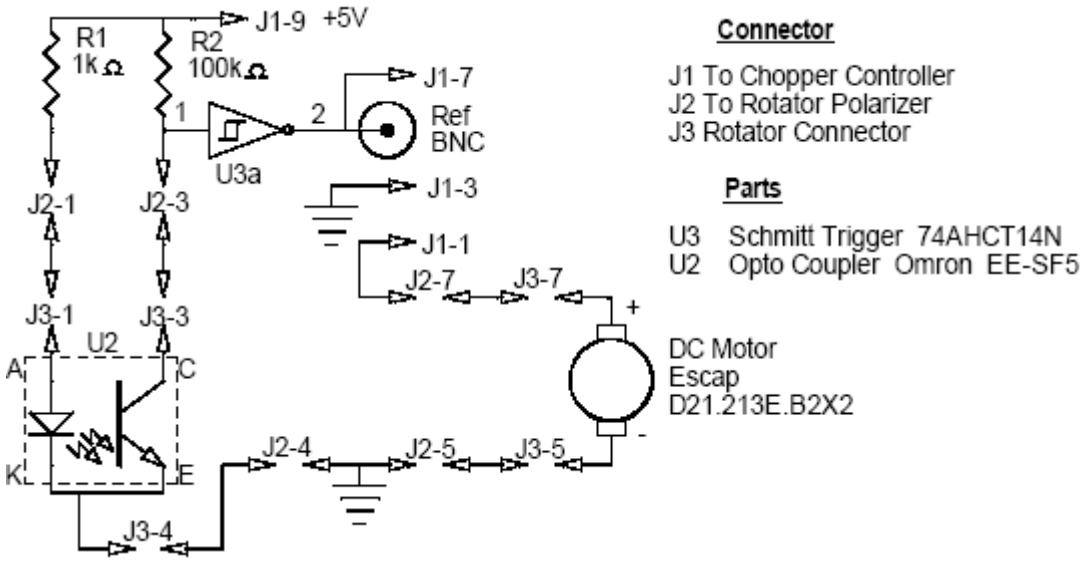


**Figure 4-16: Motor control circuit for the rotating polarizer and reference pulse signal processing circuit.**

The second part of the signal processing interface box contains the rotating polarizer controller circuit and some minor signal processing for the reference signal. The circuit is shown in Figure 4-16, and is necessary to change from the Oriel chopper control connector to the connector used for the rotating analyzer. The Schmitt trigger was incorporated in the reference signal line to guarantee a good pulse edge. This signal was also split to provide a reference pulse for the lock-in amplifier along with a frequency signal for the chopper controller.

### 4.4.4 Lock-In Amplifier (LIA)

To measure dichroism we must measure the changing polarization of light transmitted through a sample, where the changing polarization results in signals on the order of a few millivolts. Those small signals require a measurement system sensitive enough to provide accurate signal measurement amongst varying levels of noise. A Stanford Research Systems SR830 lock-in amplifier capable of measuring ac signals of a few nanovolts was used to measure the very small ac signals produced by the dichroism experiment.

The SR830 lock-in amplifier utilizes phase sensitive detection to single-out a component of a signal based on some reference signal frequency and phase. It essentially eliminates all noise signals at frequencies other than a narrow interval around the reference allowing for the accurate detection of signals that may be either very small or obscured by excessive noise. In order for the lock-in amplifier to perform phase sensitive detection it needs to create a phase-locked loop. The phase locked-loop can be established by generating a sinewave, using the internal oscillator of the lock-in amplifier, which is phase locked to some reference signal. In the case of our experiment the reference signal was provided by the rotating analyzer. A piece of reflective tape was placed on the analyzer's cylindrical housing which reflected light to an Omron EE-SF5 phototransistor. At one point during each rotation of the analyzer the transistor was forward biased; therefore, generating a repetitive pulse controlled by the RPM of the rotating analyzer.

The internally generated lock-in amplifier reference signal is

$$V_L \sin(\omega_L t + \theta_{ref}) \tag{4.10}$$

where $V_L$ is the magnitude, $\omega_L$ is the frequency that is phase locked to the external reference frequency, and $\theta_{ref}$ is the phase difference between the external and internal reference signals. Meanwhile, the input signal that we are attempting to measure is given by

$$V_S \sin(\omega_S t + \theta_S) \tag{4.11}$$

where $V_S$ is the magnitude of the input signal, $\omega_S$ is the frequency of the input signal, and $\theta_S$ is the phase difference between the external reference and the input signals. The two signals are mixed and the resulting output from the phase sensitive detector is the product of two sine waves,

$$(V_{OUT})_1 = V_S V_L \sin(\omega_S t + \theta_S)\sin(\omega_L t + \theta_{ref})$$

$$= \frac{1}{2} V_S V_L \cos([\omega_S - \omega_L]t + \theta_S - \theta_{ref}) - \frac{1}{2} V_S V_L \cos([\omega_S + \omega_L]t + \theta_S + \theta_{ref})$$

Therefore, phase sensitive detection results in two ac signals, one at the sum frequency $(\omega_S + \omega_L)$ and one at the difference frequency $(\omega_S - \omega_L)$.

Following the phase sensitive detection stage, the output signal is passed through a low pass filter. Normally the ac signals would be removed and we would be left without a signal; however, for frequencies where $\omega_S = \omega_L$ the difference frequency component of the output will produce a DC signal. In that case, the filtered output would be

$$(V_{OUT})_1 = \frac{1}{2} V_S V_L \cos(\theta_S - \theta_{ref}) \sim V_S \cos\theta \tag{4.12}$$

The final result is a DC signal that is proportional to the input signal amplitude. Now, if we consider signals for which noise is present we must consider the bandwidth of the low pass filter. Noise signals at frequencies far from the reference are removed by the low pass filter; however, frequencies very close to the reference frequency when $|\omega_{noise} - \omega_L|$ is small, will result in low frequency ac outputs from the phase sensitive detection stage. If the bandwidth of the low pass filter is large those small signals will be allowed to pass, and if the bandwidth is small they will be attenuated. By placing a filter with a very narrow bandwidth after the phase sensitive detection stage we will have a narrow band detector that eliminates all frequencies other than the reference as well as noise.

The lock-in amplifier has two phase sensitive detectors each producing an output signal. The first is exactly as described above; meanwhile, the second detector shifts the internal reference by 90° and then mixes it with the input signal. Shifting the reference oscillator by 90° gives

$$V_L \sin\left(\omega_L t + \theta_{ref} + 90°\right) \tag{4.13}$$

which has a low pass filtered output given by

$$\left(V_{OUT}\right)_2 = \frac{1}{2} V_S V_L \sin\left(\theta_S - \theta_{ref}\right) \sim V_S \sin\theta \tag{4.14}$$

Hence, there are two outputs that are displayed by the lock-in amplifier which can be labeled as $X$ and $Y$, where $X = V_S \cos\theta$ and $Y = V_S \sin\theta$. These two quantities represent the signal as a vector relative to the lock-in amplifier reference oscillator. Ultimately, we are interested in the magnitude and phase of the input signal which can be found from $X$ and $Y$,

$$R = \left(X^2 + Y^2\right)^{1/2} = V_S \tag{4.15}$$

and

$$\theta = \tan^{-1}\left(\frac{Y}{X}\right) \tag{4.16}$$

The above two results in Equation 4.15 and Equation 4.16 are the two quantities of interest as they provide quantities from which the PDi can be calculated.

### 4.4.5 Data Acquisition

Data acquisition for the measurement system was performed by a Pentium personal computer via a GPIB bus connection to a Stanford Systems SR830 lock-in amplifier. The PC used a National Instruments LabVIEW® program to poll the lock-in amplifier. At a measurement intervals specified within the LabVIEW® program the system would record the *2f* signal and the phase, given by Equation 4.15 and Equation 4.16 respectively, as well as the DC level sent directly from the photodetector, as shown in Figure 4-14.

# Chapter 5 Mathematical Description of Measurements

## 5.1 Introduction

The previous chapter established a framework for the measurement system and experimental apparatus used to perform photoinduced anisotropy studies. As was explained in that chapter, the probe beam passes through the sample and is incident on a photodetector. There are three measured quantities; the dc level, the *2f* signal, and the phase. Those three quantities represent the current state of the sample at any measurement time. This chapter deals with the mathematics involved in extracting anisotropy out of those three measured quantities.

The mathematics involves representing the probe beam as an ensemble of photons, where each photon can be described by its respective wave function. That ensemble passes through a rotating polarizer and is then incident on an absorbing sample. The statistical analysis of the ensemble traveling through both the polarizer and the sample yields the state of the photons which are incident on the photodetector. Lastly, the photons are converted into an electrical signal via the photodetector. Mathematically, a correlation between the incident photons and the electrical response of the photodetector is made which represents the photoinduced anisotropy of the sample as a function of the dc level, *2f* signal, and the phase.

## 5.2 Photoinduced Linear Anisotropy

Any sample that will eventually be irradiated is initially isotropic, as all glasses are. Irradiation with a linearly polarized laser beam causes photoinduced anisotropy to build-up in the sample as a function of time. Measurement of the phenomenon of photoinduced anisotropy involves observing the absorption of two orthogonal polarization directions as a function of irradiation time. That can be achieved by rotating the polarization of an inducing beam by 90° while measuring the effect on the sample by passing the probe beam with a rotating polarization through the sample.

From the definition of anisotropy, a material subjected to irradiation will have two absorption coefficients ($\alpha$), which are orthogonal to each other. In the case of our experiment the two absorption coefficients correspond to the two polarization directions of the inducing light. Namely, there is a component parallel to the inducing beam $\alpha_{//}$ and a component orthogonal to the inducing beam $\alpha_{\perp}$. Linear dichroism can then be defined as;

$$\Gamma = \alpha_{\perp} - \alpha_{//} \tag{5.1}$$

However, the experiment involves measuring the amount of light that has passed through the sample. We measure the intensity of the transmitted beam at each polarization of the inducing beam; therefore, we have a parallel and a perpendicular component to the intensity. This can be written as;

$$I_{\perp} = I_0 e^{-\alpha_{\perp} L} \tag{5.2}$$

$$I_{//} = I_0 e^{-\alpha_{//} L} \tag{5.3}$$

where $I_{\perp}$ and $I_{//}$ are the intensities at the respective polarization directions after passing through the sample, $I_0$ is the intensity of the initial unpolarized probe beam, and $L$ is the thickness of the sample.

We can also define the relative amount of anisotropy in the sample;

$$A = \frac{2(I_{//} - I_{\perp})}{I_{//} + I_{\perp}} \tag{5.4}$$

Equation 5.4 can be related to the absorption in the material by utilizing Equations 5.2 and 5.3. It is also true that $A \cong \Gamma L$ for small values of $\alpha_{\|} L$ and $\alpha_{\perp} L$, namely $\alpha_{\|} L << 1$ and $\alpha_{\perp} L << 1$, or [79]

$$A = \frac{I_{//} - I_{\perp}}{(I_{//} + I_{\perp})/2} = (\alpha_{\perp} - \alpha_{//}) L \tag{5.5}$$

The equation above relates the measured quantities $I_{\perp}$ and $I_{//}$ to the definition of dichroism. Considering only the relationship between intensity and anisotropy in Equation 5.4, the numerator is basically an ac quantity and the denominator an average or DC quantity. It should be noted that the influence of reflection anisotropy was not taken into

account in the above equations. It has been previously determined in [79] that the difference in reflection coefficients of the parallel $(r_{//})$, and perpendicular $(r_{\perp})$, beams (i.e. reflection anisotropy) are small and could be ignored.

## 5.3 Quantitative Analysis of Measurement Technique

### 5.3.1 Light through a Polarizer

The light generated by our probe source, which is the LED array, is ideally unpolarized; however the creation of a completely unpolarized light source could not be done. Therefore, we are left with a partially polarized beam of light emanating from the LED array, which can be broken down into a linearly polarized part and an unpolarized part. The following mathematics will demonstrate that any beam of light may be represented as a superposition of a linearly polarized beam and an unpolarized beam.

First, we must represent each photon by its wave function. The wave function of a photon or an ensemble of photons, linearly polarized at angle $\gamma$ with respect to the *x* axis can be written;

$$\left|\psi_{\gamma}\right\rangle = \cos\gamma\left|x\right\rangle + \sin\gamma\left|y\right\rangle \tag{5.6}$$

Where $\left|x\right\rangle$ and $\left|y\right\rangle$ are the eigenfunctions for *x* and *y* linear polarizations respectively, and the probability density of a photon being polarized at angle $\gamma$ be $P(\gamma)$;

$$\int_0^{2\pi} P(\gamma)d\gamma = 1 \tag{5.7}$$

When a photon in the state described by Equation 5.6 is incident on a polarizer, the result is that only the photons polarized at the same angle as the polarizer will be allowed through.

If we consider a polarizer with pass axis $x'$ at angle $\varphi$, then only a $\left|x'\right\rangle$ photon will be allowed through the polarizer. First considering only a single photon, the probability that the photon is in the $\left|x'\right\rangle$ state is;

$$\left|\left\langle x'\middle|\psi_\gamma\right\rangle\right|^2 = \left|\cos\gamma\left\langle x'\middle|x\right\rangle + \sin\gamma\left\langle x'\middle|y\right\rangle\right|^2 \tag{5.8}$$

The amplitudes $\langle x'|x\rangle$ and $\langle x'|y\rangle$ are just two of the components of the rotation matrix that takes $x$ into $x'$.

$$\left\langle x'\middle|x\right\rangle = \cos\varphi \qquad \left\langle x'\middle|y\right\rangle = \sin\varphi$$

So as expected the probability of getting through the analyzer is,

$$\left|\left\langle x'\middle|\psi_\gamma\right\rangle\right|^2 = \left(\cos\gamma\cos\varphi + \sin\gamma\sin\varphi\right)^2 = \cos^2\left(\gamma-\varphi\right) \tag{5.9}$$

If we consider the same polarizer, we have the probability of the photon passing through the polarizer of $\cos^2\left(\gamma-\varphi\right)$, and the average probability of a photon in the ensemble passing through is;

$$P_A\left(\varphi\right) = \int_0^{2\pi} P\left(\gamma\right)\cos^2\left(\gamma-\varphi\right)d\gamma \tag{5.10}$$

This can be simplified down to;

$$P_A\left(\varphi\right) = a\cos^2\left(\varphi\right) + b\sin^2\left(\varphi\right) + c\cos\left(\varphi\right)\sin\left(\varphi\right) \tag{5.11}$$

Where;

$$a = \int_0^{2\pi} P(\gamma)\cos^2(\gamma)d\gamma$$

$$b = \int_0^{2\pi} P(\gamma)\sin^2(\gamma)d\gamma$$

$$c = \int_0^{2\pi} P(\gamma)\cos(\gamma)\sin(\gamma)d\gamma$$

The result in Equation 5.11 is the average probability of a photon in an ensemble with arbitrary polarization to pass through the polarizer.

Now, we will consider another ensemble $A'$ which will be written as a combination of unpolarized light and polarized light. The ensemble consists of a fraction $f_U$ of unpolarized light with $P_U\left(\gamma\right) = \dfrac{1}{2\pi}$, and a fraction $f_P$ of linearly polarized light at angle

$\chi$ with $P_P(\gamma) = \frac{1}{2}\delta(\gamma - \chi) + \frac{1}{2}\delta(\gamma + \pi - \chi)$. The entire ensemble is the superposition of the two portions, $f_U + f_P = 1$ and $P(\gamma) = f_U P_U(\gamma) + f_P P_P(\gamma)$, where $\int_0^{2\pi} P(\gamma)\, d\gamma = 1$. Therefore, the average probability of a photon in the ensemble $A'$ passing through the polarizer with pass axis $x'$ at angle $\varphi$ is;

$$P_{A'}(\varphi) = \int_0^{2\pi} \frac{f_U}{2\pi}\cos^2(\gamma - \varphi)d\gamma + \int_0^{2\pi} \frac{f_P}{2\pi}\delta(\gamma - \chi)\cos^2(\gamma - \varphi)d\gamma$$
$$+ \int_0^{2\pi} \frac{f_P}{2}\delta(\gamma + \pi - \chi)\cos^2(\gamma - \varphi)d\gamma$$

Which yields;

$$P_{A'}(\varphi) = \frac{f_U}{2} + f_P \cos^2(\chi - \varphi) \tag{5.12}$$

We want to show that $P_A(\varphi) = P_{A'}(\varphi)$ and determine the fractions $f_U$, $f_P$ and $\chi$ in terms of the coefficient *a*, *b* and *c* from Equation 5.11. That can be done by some trigonometric manipulation and observing that;

$$P_{A'}(\varphi) = \frac{f_U}{2} + f_P\left[\cos^2(\varphi)\cos^2(\chi) + \sin^2(\varphi)\sin^2(\chi) + \cos(\varphi)\cos(\chi)\sin(\varphi)\sin(\chi)\right] \tag{5.13}$$

Using the trigonometric identity $\sin^2(\varphi) = 1 - \cos^2(\varphi)$ yields;

$$P_{A'}(\varphi) = \left[\frac{f_U}{2} + f_P \sin^2(\chi)\right] + f_P\left[\cos^2(\chi) - \sin^2(\chi)\right]\cos^2(\varphi)$$
$$+ f_P \cos(\varphi)\sin(\varphi)\cos(\chi)\sin(\chi) \tag{5.14}$$

We now have two equations, each representing an ensemble of photons incident on a polarizer. The first is for ensemble $A$ in Equation 5.11 which can be rewritten;

$$P_A(\varphi) = b + (a - b)\cos^2(\varphi) + c\cos(\varphi)\sin(\varphi) \tag{5.15}$$

In order for $P_A(\varphi) = P_{A'}(\varphi)$ we must have;

$$c = f_P \cos(\chi)\sin(\chi) = \tfrac{1}{2} f_P \sin(2\chi) \tag{5.16}$$

$$a - b = f_P\left[\cos^2(\chi) - \sin^2(\chi)\right] = f_P \cos(2\chi) = f_P\left[1 - 2\sin^2(\chi)\right] \tag{5.17}$$

$$b = \tfrac{1}{2} f_U + f_P \sin^2(\chi) \tag{5.18}$$

Solving for $f_U, f_P, \chi$

$$f_U = 2b - 2 f_P \sin^2(\chi)$$

but

$$-2 f_P \sin^2(\chi) = a - b - f_P$$

so

$$f_U = 2b + a - b - f_P = a + b - f_P = a + b - \left[ (a-b)^2 + 4c^2 \right]^{\frac{1}{2}} \tag{5.19}$$

and

$$f_P = \frac{a-b}{\cos(2\chi)} = \frac{a-b}{\cos\left( \tan^{-1}\left( \frac{2c}{a-b} \right) \right)}$$

since,

$$\cos\left( \tan^{-1}(x) \right) = \frac{1}{\left(1 + x^2\right)^{\frac{1}{2}}}$$

$$f_P = [a-b]\left[ 1 + \left( \frac{2c}{a-b} \right)^2 \right]^{\frac{1}{2}} = \left[ (a-b)^2 + 4c^2 \right]^{\frac{1}{2}} \tag{5.20}$$

and

$$\frac{c}{a-b} = \tfrac{1}{2}\tan(2\chi) \Rightarrow \chi = \tfrac{1}{2}\tan^{-1}\left( \frac{2c}{a-b} \right) \tag{5.21}$$

Notice $f_U + f_P = a + b = \int_0^{2\pi} P(\theta)\left[ \cos^2(\varphi) + \sin^2(\varphi) \right] d\theta = 1$ as it should be.

In summary, for an arbitrary ensemble of photons passing through a polarizer the output will be the same as ensemble $A'$ if we choose;

$$f_U = 1 - \left[ (a-b)^2 + 4c^2 \right]^{\frac{1}{2}} \tag{5.19}$$

$$f_P = \left[ (a-b)^2 + 4c^2 \right]^{\frac{1}{2}} \tag{5.20}$$

$$\chi = \tfrac{1}{2}\tan^{-1}\left( \frac{2c}{a-b} \right) \tag{5.21}$$

Therefore, the output from the polarizer will be the same regardless of which ensemble we choose; i.e. $P_A(\varphi) = P_{A'}(\varphi)$. The arbitrary beam of light can be represented by the superposition of an unpolarized beam of light with a linearly polarized beam of light.

## 5.3.2 Light through an Absorbing Sample

We need to determine the effect of an absorbing sample on an incident photon, or ensemble of photons. A dichroic sample has different absorption coefficients depending on the polarization of the light. If we let $\alpha_x$ be the absorption coefficient for a $|x\rangle$ photon and $\alpha_y$ for a $|y\rangle$ photon, then for a sample of thickness $L$ we can write an operator;

$$S_{op} = e^{-\alpha_x L}|x\rangle\langle x| + e^{-\alpha_y L}|y\rangle\langle y| \tag{5.22}$$

The operator in Equation 1.22 ignores reflections from boundaries and neglects the fact that there is a change in refractive index accompanying the dichroism.

Once again we will establish a wave function that represents an incoming photon, then we will use the sample operator to determine the effect of the sample on that photon. Therefore, we once again describe a photon polarized at angle $\gamma$ by Equation 5.6 as follows;

$$|\psi_\gamma\rangle = \cos(\gamma)|x\rangle + \sin(\gamma)|y\rangle \tag{5.6}$$

The sample produces;

$$S_{op}|\psi_\gamma\rangle = e^{-\alpha_x L}\cos(\gamma)|x\rangle + e^{-\alpha_y L}\sin(\gamma)|y\rangle \tag{5.23}$$

The expectation value or probability that the photon is not absorbed is;

$$e^{-\alpha_x L}\cos^2(\gamma) + e^{-\alpha_y L}\sin^2(\gamma) \tag{5.24}$$

Then for an ensemble of photons $A$, the average probability for a photon to pass through the sample is;

$$P_A = \int_0^{2\pi} P(\gamma)[e^{-\alpha_x L}\cos^2(\gamma) + e^{-\alpha_y L}\sin^2(\gamma)]d\gamma \tag{5.25}$$

Or using the notation of the previous section;

$$P_A = e^{-\alpha_x L}\int_0^{2\pi} P(\gamma)\cos^2(\gamma) + e^{-\alpha_y L}\int_0^{2\pi} P(\gamma)\sin^2(\gamma)d\gamma \tag{5.26}$$

$$P_A = ae^{-2\alpha_x L} + be^{-2\alpha_y L} \tag{5.27}$$

Similar to the previous section, we want to demonstrate that we can obtain the same result for $P_A$ if we start with the special distribution;

$$P(\gamma) = \frac{f_U}{2\pi} + f_P\left[\frac{1}{2}\delta(\gamma-\chi)+\frac{1}{2}\delta(\gamma+\pi-\chi)\right] \tag{5.28}$$

The special distribution above is the superposition of an unpolarized beam of light and a beam of light linearly polarized at angle $\chi$. The quantities $f_U$, $f_P$, and $\chi$ are related to *a*, *b*, and *c* exactly the same as in the previous section in Equations 5.19, 5.20, and 5.21. For this ensemble of photons $A'$, the average probability that a photon will not be absorbed is;

$$P_{A'} = \frac{f_U}{2\pi}\int_0^{2\pi} e^{-2\alpha_x L}\cos^2(\gamma)+e^{-2\alpha_y L}\sin^2(\gamma)d\gamma + f_P[e^{-2\alpha_x L}\cos^2(\chi)+e^{-2\alpha_y L}\sin^2(\chi)] \tag{5.29}$$

$$P_{A'} = \frac{1}{2}f_U[e^{-2\alpha_x L}+e^{-2\alpha_y L}]+ f_P[e^{-2\alpha_x L}\cos^2(\chi)+e^{-2\alpha_y L}\sin^2(\chi)] \tag{5.30}$$

Utilizing Equations 5.19, 5.20 and 5.21, and the following trigonometric identities;

$$\cos\left(\tfrac{1}{2}\tan^{-1}(x)\right) = \pm\left(\frac{1}{2}\left[1+\frac{1}{\left(1+x^2\right)^{\frac{1}{2}}}\right]\right)^{\frac{1}{2}}$$

$$\sin\left(\tfrac{1}{2}\tan^{-1}(x)\right) = \pm\left(\frac{1}{2}\left[1-\frac{1}{\left(1+x^2\right)^{\frac{1}{2}}}\right]\right)^{\frac{1}{2}}$$

the probability that a photon will not be absorbed can be rewritten in terms of the absorption coefficients as well as the coefficients *a*, *b*, and *c*. The result is the following;

$$P_{A'} = \frac{1}{2}\left(1-\left[(a-b)^2+4c^2\right]^{\frac{1}{2}}\right)\left(e^{-2\alpha_x L}+e^{-2\alpha_y L}\right)$$

$$+\left[(a-b)^2+4c^2\right]^{\frac{1}{2}}\left[\frac{1}{2}\left(1+\frac{a-b}{\left[(a-b)^2+4c^2\right]^{\frac{1}{2}}}\right)e^{-2\alpha_x L}+\frac{1}{2}\left(1-\frac{a-b}{\left[(a-b)^2+4c^2\right]^{\frac{1}{2}}}\right)e^{-2\alpha_y L}\right]$$

$$=\frac{1}{2}\left(1-\left[(a-b)^2+4c^2\right]^{\frac{1}{2}}\right)\left(e^{-2\alpha_x L}+e^{-2\alpha_y L}\right)$$

$$+\frac{1}{2}\left[\left(\left[(a-b)^2+4c^2\right]^{\frac{1}{2}}+(a-b)\right)e^{-2\alpha_x L}+\left(\left[(a-b)^2+4c^2\right]^{\frac{1}{2}}-(a-b)\right)e^{-2\alpha_y L}\right]$$

$$P_{A'}=\frac{1}{2}\left[(1+a-b)e^{-2\alpha_x L}+(1-a+b)e^{-2\alpha_y L}\right] \tag{5.31}$$

We also have $a+b=1, 1+a-b=2a$, and $1-a+b=2b$ which yields;

$$P_A = ae^{-2\alpha_x L}+be^{-2\alpha_y L}=P_{A'} \tag{5.32}$$

The result in Equation 5.32 demonstrates that when light passes through an absorbing sample the resulting output can be represented in two ways. The first is as an arbitrary beam of light linearly polarized at angle $\chi$. The second is the superposition of an unpolarized beam of light with a beam of light linearly polarized at angle $\chi$.

### 5.3.3 Light Incident on a Detector

The actual experimental measurements that were made involved the passage of light first through a polarizer, or rotating analyzer, then through an absorbing $As_2Se_3$ thin film. The light that passed through the sample was incident on the photodetector, and converted into an electrical signal consisting of a dc level, a *2f* signal, and a phase. In order to determine how that incident light is related to the measured quantities we need to know the amount of light that is being generated by the source and how much of that light is getting through to the detector.

In our experiment we have the case where the light generated by the source must first pass through the rotating analyzer. The intensity of the light that passes through the analyzer is directly related to the average probability of a photon passing through a polarizer. Namely, given a photon flux from the source $F\left(photons/area/sec\right)$, then;

$$I_A = h\nu F P_A(\varphi) \tag{5.33}$$

In the case where the analyzer precedes the sample as in our experimental apparatus, we have a simpler arrangement because all of the photons after the analyzer are in the same state.

The light source produces an ensemble of photons with a distribution of polarizations that we take to be;

$$P(\gamma) = \frac{f_U}{2\pi} + \tfrac{1}{2} f_P \left[ \delta(\gamma - \chi) + \delta(\gamma + \pi - \chi) \right] \tag{5.28}$$

We are assuming that the light source is the special distribution consisting of the superposition of an unpolarized beam and a polarized beam. If we let the analyzer's pass axis be at angle $\varphi$, then after the analyzer all photons will be in the same state, because only the photons polarized at angle $\varphi$ will pass through;

$$\left|\psi_\varphi\right\rangle = \cos(\varphi)\left|x\right\rangle + \sin(\varphi)\left|y\right\rangle \tag{5.34}$$

Now, we have the average probability density of a photon passing through the analyzer;

$$P_A(\varphi) = \frac{f_U}{2} + f_P \cos^2(\chi - \varphi) \tag{5.35}$$

Similarly, this new ensemble of photons passes through the sample with an average probability density per photon of;

$$P_S = e^{-2\alpha_x L} \cos^2(\varphi) + e^{-2\alpha_y L} \sin^2(\varphi) \tag{5.36}$$

The intensity of light either after the analyzer or the sample is proportional to the average probability of a photon passing through either medium. Therefore, the intensity of light that passes through the analyzer and the sample, and is subsequently incident on the detector, can be written;

$$I = h\nu F P_A P_S \tag{5.37}$$

$$I = h\nu F \left[ \frac{f_U}{2} + f_P \cos^2(\chi - \varphi) \right] \left[ e^{-2\alpha_x L} \cos^2(\varphi) + e^{-2\alpha_y L} \sin^2(\varphi) \right] \tag{5.38}$$

In order to make a few simplifications we note that $f_U + f_P = 1$ and we make the following substitutions $\Delta = \frac{1}{2}\left[e^{-2\alpha_x L} - e^{-2\alpha_y L}\right]$ and $\Sigma = \frac{1}{2}\left[e^{-2\alpha_x L} + e^{-2\alpha_y L}\right]$. The result is that the first and second terms of Equation 1.38 can be simplified to reveal the following;

$$I = hvF\left[\frac{1}{2}\left(f_U + f_P + f_P\cos[2(\chi-\varphi)]\right)\right]\left[\Delta\cos(2\varphi)+\Sigma\right]$$

$$I = hvF\left[\frac{1}{2}\left(1 + f_P\cos[2(\chi-\varphi)]\right)\right]\left[\Delta\cos(2\varphi)+\Sigma\right]$$

$$I = \frac{1}{2}hvF\left[1 + f_P\cos[2(\chi-\varphi)]\right]\left[\Delta\cos(2\varphi)+\Sigma\right] \tag{5.39}$$

Here it is convenient to switch to complex exponentials and utilize Euler's formula $\cos(x) = \frac{1}{2}\left[e^{ix} + e^{-ix}\right]$. Therefore;

$$I = \frac{hvF}{2}\left[1 + \frac{1}{2}f_P\left(e^{2i(\chi-\varphi)} + e^{-2i(\chi-\varphi)}\right)\right]\left[\Delta\frac{1}{2}\left(e^{2i\varphi} + e^{-2i\varphi}\right) + \Sigma\right] \tag{5.40}$$

Multiplying all this out and grouping terms gives;

(DC) $$I = \frac{hvF}{2}[\Sigma + \tfrac{1}{2}f_P\Delta\cos(2\chi)$$

(*2f*) $$+\Delta\cos(2\varphi) + f_P\Sigma\cos 2(\chi-\varphi)$$

(*4f*) $$+\tfrac{1}{2}f_P\Delta\cos 2(\chi-2\varphi)] \tag{5.41}$$

As mentioned previously, our setup involves a rotating analyzer for which $\varphi = 2\pi ft$. Then the first term above in Equation 1.43 is the DC part, the second term the *2f* (2nd harmonic) part and the third term is the 4f (4th harmonic) part. For the purpose of our experiment we are mainly interested in the *2f* term.

$$I_{2f} = \frac{hvF}{2}\left[\Delta\cos(2\varphi) + f_P\Sigma\cos 2(\chi-\varphi)\right] \tag{5.42}$$

Once again it is more convenient to use complex notation and to make the argument of the second cosine term $\cos 2(\chi-\varphi)$, to provide the following result;

$$I_{2f} = \frac{hvF}{2}\mathrm{Re}\left[\left(\Delta + f_P\Sigma e^{-2i\chi}\right)e^{2i\varphi}\right] \tag{5.43}$$

The phasors in the parenthesis determine the magnitude and phase of the *2f* signal which is what the lock-in amplifier measures.

Magnitude $$\left|I_{2f}\right| = \frac{h\nu F}{2}\left[\left(\Delta + f_P \Sigma \cos\left(2\chi\right)\right)^2 + \left(f_P \Sigma \sin\left(2\chi\right)\right)^2\right]^{\frac{1}{2}}$$

$$\left|I_{2f}\right| = \frac{h\nu F}{2}\left[\Delta^2 + {f_P}^2\Sigma^2 + 2\Delta\Sigma f_P \cos\left(2\chi\right)\right]^{\frac{1}{2}} \tag{5.44}$$

Phase $$\theta = \tan^{-1}\left(\frac{-f_P \Sigma \sin\left(2\chi\right)}{\Delta + f_P \Sigma \cos\left(2\chi\right)}\right) \tag{5.45}$$

DC Level $$I_{DC} = \frac{h\nu F}{2}\left[\Sigma + \tfrac{1}{2} f_P \Delta \cos\left(2\chi\right)\right] \tag{5.46}$$

The three equations above represent the measured experimental quantities.

## 5.3.4 Determining Anisotropy from Measured Quantities

The goal of creating a mathematical description of the measurement system was to develop a quantitative relationship between the amount of anisotropy induced in a given sample and the electrical measurements made by the measurement system. This section demonstrates that relationship between Equations 5.44, 5.45, and 5.46.

The basic equation for anisotropy was given in section 5.2 as;

$$A = \left(\alpha_x - \alpha_y\right)L \tag{5.5}$$

Equation 5.5 relates the absorption coefficients in two orthogonal directions to the anisotropy of the sample. In the previous section we also chose $\Delta = \frac{1}{2}\left[e^{-2\alpha_x L} - e^{-2\alpha_y L}\right]$ and $\Sigma = \frac{1}{2}\left[e^{-2\alpha_x L} + e^{-2\alpha_y L}\right]$, which can be combined with Equation 5.5 to provide the desired relationship. First, we will make the substitutions $x = 2\alpha_x L$ and $y = 2\alpha_y L$, to yield;

$$\Delta = \frac{e^{-x} - e^{-y}}{2}, \qquad \Sigma = \frac{e^{-x} + e^{-y}}{2}$$

Therefore, we can manipulate $\Sigma$ and $\Delta$ to obtain;

$$\Sigma + \Delta = \frac{e^{-x}}{2} + \frac{\cancel{e^{-y}}}{\cancel{2}} + \frac{e^{-x}}{2} - \frac{\cancel{e^{-y}}}{\cancel{2}} = e^{-x}$$

$$\Sigma - \Delta = \frac{\cancel{e^{-x}}}{\cancel{2}} + \frac{e^{-y}}{2} - \frac{\cancel{e^{-x}}}{\cancel{2}} + \frac{e^{-y}}{2} = e^{-y}$$

We can then write $x$ and $y$ in terms of $\Sigma$ and;

$$-x = \ln(\Sigma + \Delta)$$

$$-y = \ln(\Sigma - \Delta)$$

Or;

$$-2\alpha_x L = \ln(\Sigma + \Delta)$$

$$-2\alpha_y L = \ln(\Sigma - \Delta)$$

Which can also be written;

$$\alpha_x L = -\frac{1}{2}\ln(\Sigma + \Delta)$$

$$\alpha_y L = -\frac{1}{2}\ln(\Sigma - \Delta)$$

Therefore the anisotropy in terms of $\Delta$ and $\Sigma$ is;

$$A = (\alpha_x - \alpha_y)L = \frac{1}{2}\ln(\Sigma - \Delta) - \frac{1}{2}\ln(\Sigma + \Delta)$$

$$A = \frac{1}{2}\ln\left(\frac{\Sigma - \Delta}{\Sigma + \Delta}\right) \tag{5.47}$$

The result in Equation 5.47 is verified by the fact that for an isotropic sample $\Delta = 0$ and $\Sigma = 1$, due to the lack of difference between absorption coefficients for orthogonal directions, which results in $A = \frac{1}{2}\ln\left(\frac{1-0}{1+0}\right) = \frac{1}{2}\ln(1) = 0$ which is exactly the correct result for a truly isotropic sample. The method for determining the anisotropy of a sample from measured quantities now becomes one of determining $\Sigma$ and $\Delta$ from the measurements and then determining the anisotropy. The variables were solved from measured data using a Matlab program.

## 5.4 System Calibration

The photodetector measures the *2f* signal, the dc level, and the phase of the light that is transmitted through the sample. Those three measured quantities are represented by Equations 5.44, 5.45, and 5.46. In order to use those equations to accurately determine the anisotropy of the sample the absolute polarization $2\chi$ and the intensity $I_0 = \frac{hvF}{2}$ of the probe source must be determined. That involved a system calibration prior to sample measurements.

The system calibration was first done for the absolute polarization of the probe. In order to do that a reference plane had to be established. The simplest choice was to take a horizontal plane with respect to the experimental apparatus and then measure the polarization with respect to that plane. The next step was to record three measurements; the phase of the probe source alone, the phase of the probe source passing through a vertical polarizer, and the phase of the probe source passing through a horizontal polarizer. Those three measurements will yield the absolute polarization of the probe source, as shown in Figure 5-1 below.

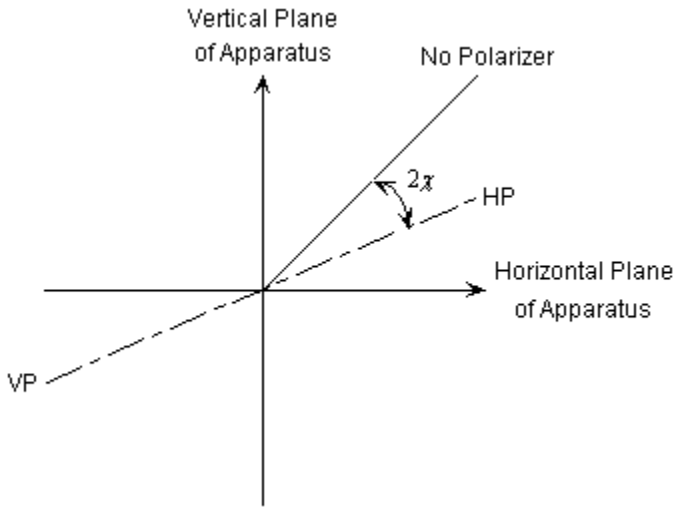


**Figure 5-1: Diagram of method to determine the absolute polarization of the probe source. The labels HP and VP represent the angles measured when the probe source passed through a horizontal polarizer and a vertical polarizer, respectively.**

The probe source polarization was measured before any anisotropy measurement set was to be recorded. It was also done periodically to check whether or not the angle drifts with time. We found that the absolute polarization of the probe source remained fairly constant over long periods of time. There were normal fluctuations due to variation in temperature of the room containing the apparatus. However, there were no long term changes in the value of the angle $2\chi$.

The second portion of any system calibration involved determining the dc level of the probe source. Before an anisotropy run was recorded, a measurement of the system with no sample in place was done. When there is no sample in place $\Sigma = 1$ and $\Delta = 0$, therefore the recorded dc level at the photodiode represents the dc level of the probe source. Mathematically, this is given by;

$$I_{DC} = \frac{h\nu F}{2} = I_O \tag{5.48}$$

It was found that there were small fluctuations in the dc level of the probe, also most likely due to temperature variation. However, over long periods of time the dc level stayed essentially constant.

# Chapter 6 Results and Discussion

## 6.1 Introduction

This chapter presents the experimental results obtained from measurements and mathematical analysis performed using the measurement system and analysis method outlined in the previous two chapters. Photoinduced dichroism (PDi) was measured in thin films of amorphous $As_2Se_3$ (a-$As_2Se_3$) using both excitation sources. The time dependence of induced dichroism was fit to an exponential function of the form $\exp(-(t/\tau)^{\beta})$. Of interest from the fitting function are three parameters: the saturation level ($A_{sat}$), time constant ($\tau$), and stretching exponent ($\beta$). Those three parameters represent the kinetics of PDi and the following sections present them as a function of pump beam intensity, sample thickness, and external electric field. Results were also obtained for those samples doped with small quantities of iodine (0.1%).

Measurements of PDi were performed using the experimental setup described in Chapter 4 of this work and is similar to that used by other researchers [90]. Depending on the measurement the HeNe laser or the 658 nm laser diode supplies the pump beam inducing the dichroism. In the case of the HeNe laser, the beam passes through a polarizer which can be rotated by 90°; however, for the laser diode the holder itself can be rotated so the polarizer is no longer included in the setup. The spot on the sample is approximately 5 mm in diameter and has a maximum intensity of 3.5 mW/mm$^2$ when using the 658 nm laser diode and 1.5 mW/mm$^2$ when using the HeNe laser.

The probe beam used to monitor the PDi buildup within the sample was derived from an array of nineteen red LEDs with a peak wavelength of 635 nm. The use of LEDs eliminates the interference patterns that can occur when using lasers, and provides very close to unpolarized light. The probe beam was passed through a polarizer rotating at frequency $f$ and is then focused onto the sample with a spot size of about 1 mm in diameter. Once the probe beam traverses the sample it is refocused onto the Hamamatsu number S1336 pin photodetector. A lock-in amplifier extracts the $2f$ signal which is proportional to the dichroism induced in the sample. The description of the probe source

given in Chapter 4 stated that the probe light source was not completely unpolarized; therefore, it was necessary to account for any residual polarization introduced by the probe beam and remove it during the analysis.

An experimental run consists of first photodarkening (PD) the sample to prevent any possible interference that may arise from scalar effects; then, exposing the sample to the pump beam while the 2*f* signal is recorded. The entire measurement process requires that a measurement without the sample in place be done first to provide a reference point for a completely isotropic system. Prior to PD a measurement involving only the probe beam and the sample is recorded to determine if the sample has any initial anisotropy. It is of note that the PD prior to PDi measurements is not necessary as it is thought the two processes are completely independent of each other [79, 83].

Once the PDi saturates, the polarization of the pump beam is rotated by 90°, and the 2*f* signal is once again recorded until saturation of the PDi. The process is repeated four or more times and the analysis method outlined in Chapter 5 is used to extract the anisotropy factor *A* from the data. The calculated anisotropy can then be plotted as a function of time and the resulting plot for an arbitrary experimental run is shown in Figure 6-1.

To extract the kinetics of PDi from an experimental run the data were separated into individual measurement cycles, each consisting of data starting from zero anisotropy and proceeding to full saturation for one polarization state. For each cycle the time dependence of *A* can be fit to a stretched exponential function of the form

$$A(t) = A_{sat} + (A_{init} - A_{sat})e^{-(t/\tau)^{\beta}} \tag{6.1}$$

where $A_{init} = A(0)$ (any change to the pump beam defines $t = 0$), and the three fitting parameters are $A_{sat} = A(\infty)$ the saturated anisotropy, $\tau$ the time constant, and $\beta$ the stretching exponent. The time-dependence of PDi requires a stretched exponential, as was demonstrated in other works [9, 16, 81], and is shown in Figure 6-2 where it can be seen that simple exponential does not fit well to the data.

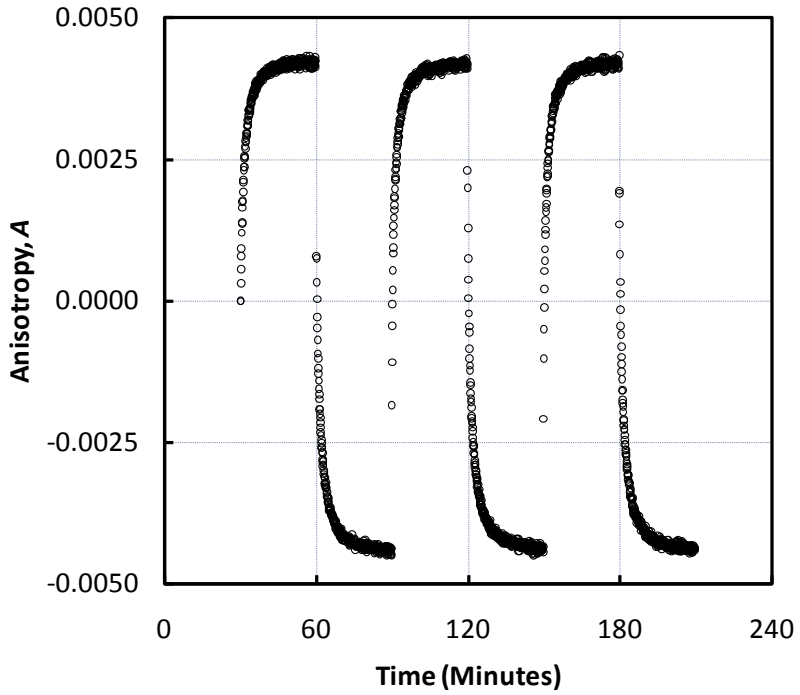


**Figure 6-1:** **Typical experimental measurement of PDi in a-$As_2Se_3$. In the plot there are 6 measurement cycles, 3 at each polarization.**

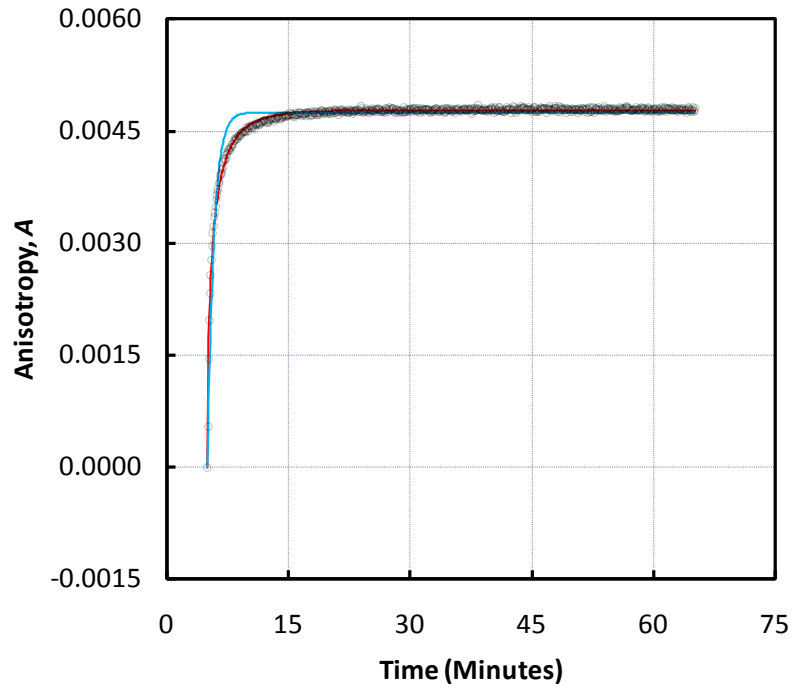


**Figure 6-2:** **Typical time dependence of the anisotropy factor *A*. The stretched exponential function (red line) provides a very good fit to the data (faded circles). The best possible fit to the data using a simple exponential function (blue line) demonstrates that its significant deviation from the data.**

For each polarization state, or measurement cycle, we obtained a set of three fitting parameters. To provide some measure of error in the three parameters statistics over all the cycles were determined from standard statistical formulae. The mean value

$$\bar{x} = \frac{\sum_{i=1}^{N} x_i}{N} \tag{6.2}$$

where $\bar{x}$ is the average or mean value, $x_i$ is the $i$-th data point, and $N$ is the number of data points in the measurement set. The standard deviation

$$s = \sqrt{\frac{\sum_{i=1}^{N} \left(x_i - \bar{x}\right)^2}{N-1}} \tag{6.3}$$

where $s$ is the standard deviation and the other parameters remain as above. The standard error

$$s_e = \frac{s}{\sqrt{N}} \tag{6.4}$$

where $s_e$ is the standard error.

In order to understand the kinetics of PDi determined from the experimental results we will refer to the model proposed by Fritzsche [84]. In [84] it was noted that although a glass is initially isotropic, small regions called micro-volumes can be highly anisotropic. This is especially true for glasses that are composed of rings or chains of atoms such as the chalcogenide glasses. The micro-volumes can preferentially absorb light with a certain polarization causing a local structural change within the material. In the event that the resulting structure preferentially absorbs light with a different polarization we have what is referred to as dichroism. The process is a sort of optical pumping where the micro-volumes are altered toward states that weakly absorb the applied polarization. In order for the aforementioned process to occur three conditions must be met by the material: there must be sufficient freedom to allow the micro-volumes to change to a different yet stable structure, the electron-hole recombination must occur within the absorbing micro-volume with a high probability, and a low-energy pathway must exist between stable configurations. Chalcogenide glasses fulfill these conditions, and the

material which is the focus of this thesis, a-$As_2Se_3$ has been a paradigm for these effects. The following sections will present the results of PDi experiments performed on a-$As_2Se_3$ and attempt to place those results within the framework put forward in [84].

## 6.2 Photoinduced Anisotropy Measurements

### 6.2.1 Intensity Dependence

The effect of pump light intensity ($I_{pump}$) on the three fitting parameters is discussed in this section. All PDi measurements were made at room temperature, on the same spot, starting with the lowest intensity and proceeding to maximum intensity. Inducing light intensity ranged from 0.1 mW/mm$^2$ to 3.5 mW/mm$^2$, depending on the selection of the inducing source. The intensity of the pump beam was varied by placing the appropriate neutral density filter(s) in the path of the pump beam. As was discussed previously care was also taken to fully photodarken the spot prior to PDi measurements. It is of note that all samples used for intensity dependence measurements were prepared by thermal evaporation.

We will first discuss the variability of the saturation level $A_{sat}$ with $I_{pump}$. Figure 6-3 and Figure 6-4 show the dependence of $A_{sat}$ on $I_{pump}$ for 0.78 μm and 1.9 μm thick samples respectively. In both cases the linear regression indicates a very weak or non-existent relationship between saturation level and pump light intensity which agrees with previous reports [91]. Other researchers have found a small negative slope to the data [92, 42]; however, there have been reports of large decreases in saturation level with increasing pump intensity [16]. The disparity in the results seems to suggest experimental discrepancies rather than any actual trend.

If $A_{sat}$ does indeed fail to vary with $I_{pump}$ then the results would fit nicely within the framework put forth in [84]. The lack of dependence on $I_{pump}$ would suggest that structural relaxation is much slower than the inducing process. The model indicates that

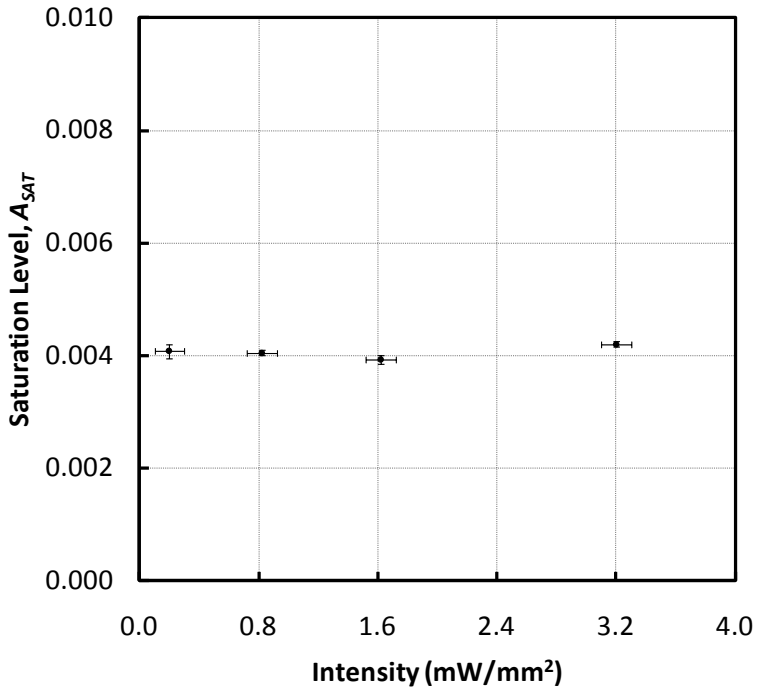


**Figure 6-3: PDi saturation level ($A_{sat}$) as a function of pump light intensity for a 0.78 µm sample of a-$As_2Se_3$.**

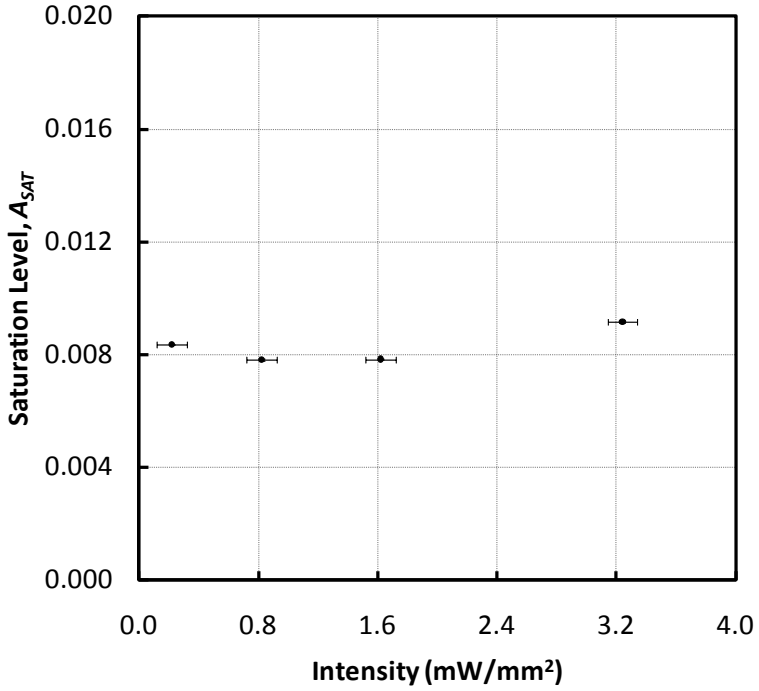


**Figure 6-4: PDi saturation level ($A_{sat}$) as a function of pump light intensity for a 1.9 µm sample of a-$As_2Se_3$.**

the level of dichroism is determined by an equilibrium with thermally driven structural changes which tend to randomize the micro-volumes. In the case where the rate of thermal relaxation was comparable or larger than the inducing rate, then increasing $I_{pump}$ would subsequently increase the level of dichroism. The failure to observe such a dependence on $I_{pump}$ implies that $A_{sat}$ is instead limited by the total number of suitable micro-volumes.

Figure 6-5 and Figure 6-6 demonstrate the inverse relationship between $I_{pump}$ and the time constant, where it can be seen that the rate ($1/\tau$) depends linearly on $I_{pump}$. These results are not surprising as they agree with other works [16, 86]. The results allow us to infer that the structural changes produced by the recombination events are independent of each other. It is of note that the maximum $I_{pump}$ is not very large and non-linear effects might occur for larger values of $I_{pump}$.

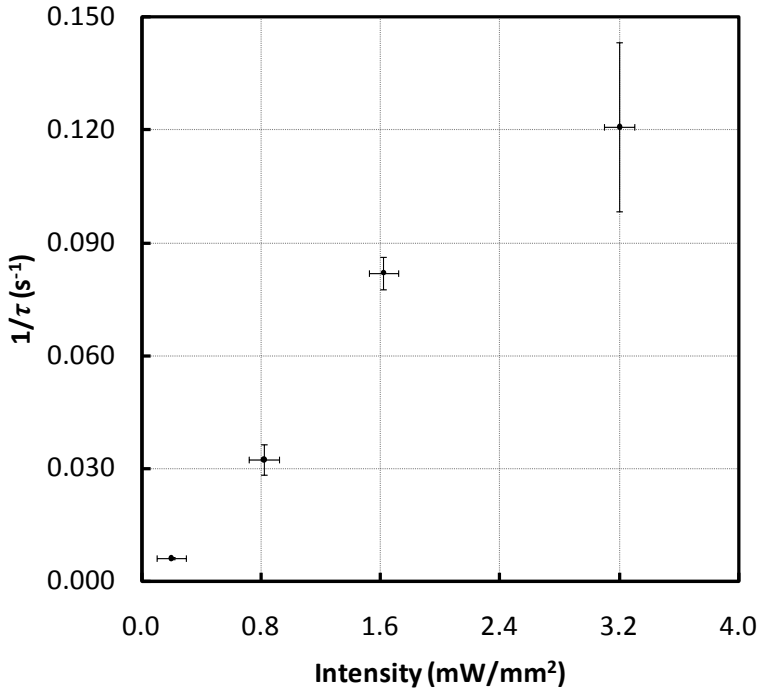


**Figure 6-5: The dependence of the rate ($1/\tau$) for inducing PDi on pump light intensity for a 0.78 µm sample of a-$As_2Se_3$.**

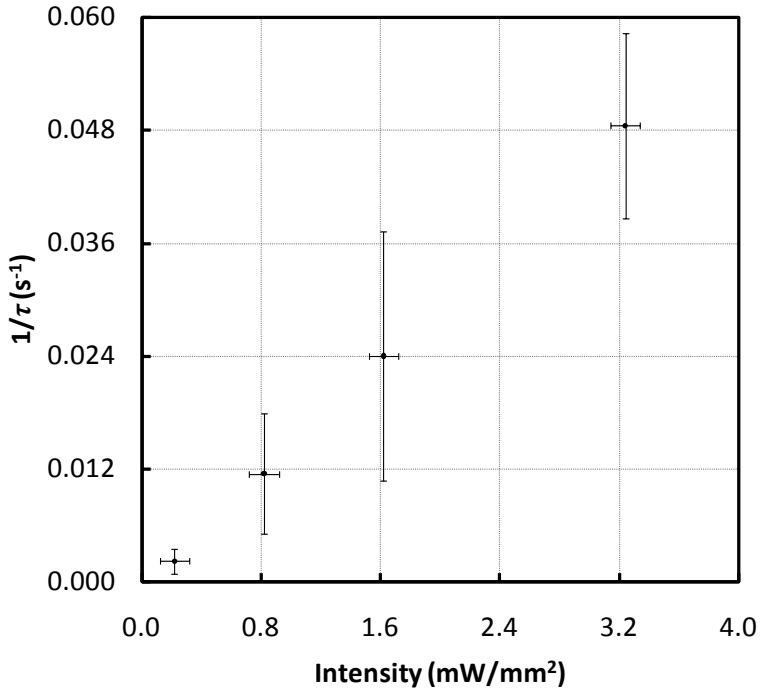


**Figure 6-6: The dependence of the rate (1/τ) for inducing PDi on pump light intensity for a 1.93 µm sample of a-$As_2Se_3$.**

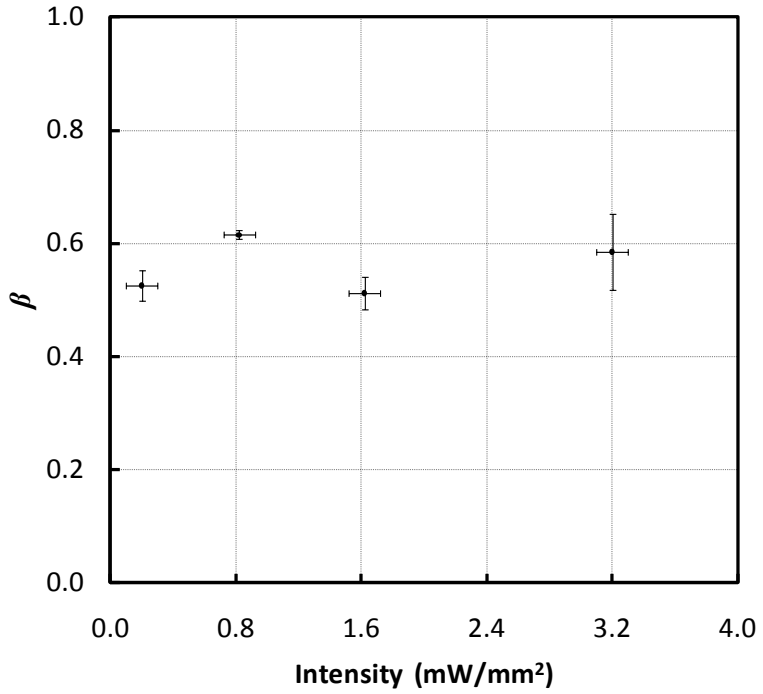


**Figure 6-7: The dependence of the stretching exponent $\beta$ on pump light intensity for a 0.78 µm sample of a-$As_2Se_3$.**

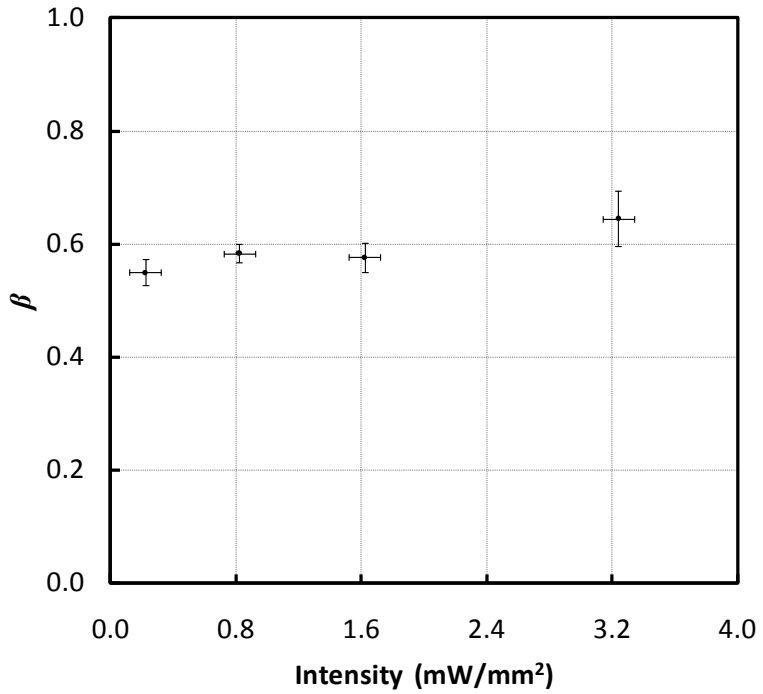


**Figure 6-8: The dependence of the stretching exponent $\beta$ on pump light intensity for a 1.93 µm sample of a-$As_2Se_3$.**

The last parameter $\beta$, is shown to have no functional dependence on $I_{pump}$ (Figure 6-7 and Figure 6-8). In both figures we see $\beta$ vary by as much as 20% which is normal from run to run on the same spot, on the same sample, with the same value of $I_{pump}$. The significance of $\beta$ for a microscopic model is not obvious. It could be the measure of the distribution of energy barriers for structural reconfiguration whereby a single energy barrier would produce a simple exponential time dependence [91]. If that assumption is correct then $\beta$ would be determined by the materials structure and should not depend on $I_{pump}$. It is of note that the values reported here are in some cases comparable to [86] and in some cases slightly less [93] than those found by other researchers.

## 6.2.2 Effect of Film Thickness

In this section we will discuss variations on the kinetics of PDi as a function of film thickness. All PDi measurements were made at room temperature with an exctiation source intensity of approximately 1.2 mW/mm$^2$. Care was also taken to fully

photodarken the spot prior to PDi measurements. All samples measured in this section were prepared by thermal evaporation.

In Section 5.2 of this thesis we defined the amount of relative anisotropy in a sample as a function of absorption coefficient and thickness of that sample;

$$A = \frac{I_{//} - I_{\perp}}{(I_{//} + I_{\perp})/2} = (\alpha_{\perp} - \alpha_{//})L \tag{6.1}$$

Equation 5.5 suggests that the anisotropy factor for a fully saturated sample should be linearly proportional to sample thickness. Figure 6-9 demonstrates that this is in fact the case as we see a linear dependence of saturation level on thickness, with a slope of $(\alpha_{\perp} - \alpha_{//}) \approx 48$ cm$^{-1}$. At the pump wavelength $1/\alpha \sim$ 0.5μm; therefore, the maximum relative change in absorption coefficient amounts to approximately $2.5 \times 10^{-3}$.

Figure 6-10 shows a decrease in the rate ($1/\tau$) with increasing sample thickness. The rate decreases because the light intensity of the pump beam falls off with increasing depth in the material; therefore, the rate would also decrease with increasing depth in the material. The observed rate is essentially an average over the thickness of the sample; so, the thicker the sample, the lower the average.

The stretching exponent $\beta$ as a function of sample thickness is shown in Figure 6-11. The parameter $\beta$ appears mostly independent of sample thickness; however, there does appear to be some downward trend with increasing sample thickness. The downward trend cannot be explained by the same mechanism as the rate as $\beta$ was previously shown to be independent of intensity; however, the downward trend is in agreement with previously reported results [91] and those reported by other researchers [86]. It is of note that we also see a slight increase in $\beta$ at approximately the penetration depth of the a-$As_2Se_3$ as was reported in [86].

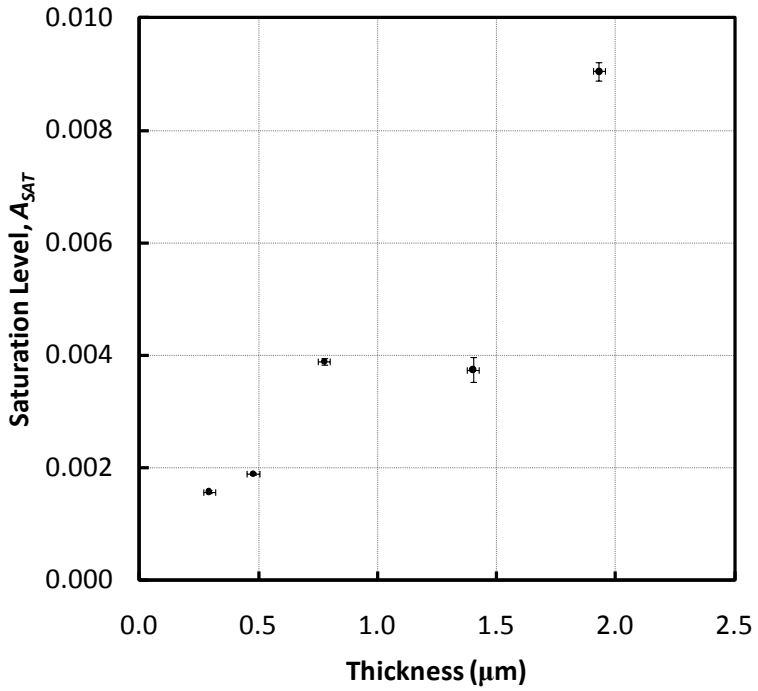


**Figure 6-9: PDi saturation level ($A_{sat}$) as a function of film thickness in a-$As_2Se_3$.**

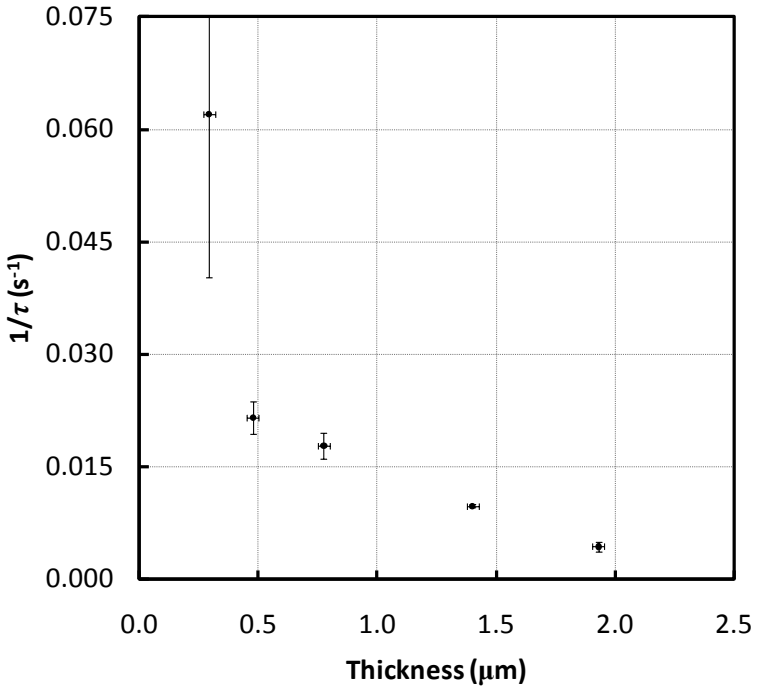


**Figure 6-10: The dependence of the rate (1/τ) for inducing PDi on sample thickness for a-$As_2Se_3$.**

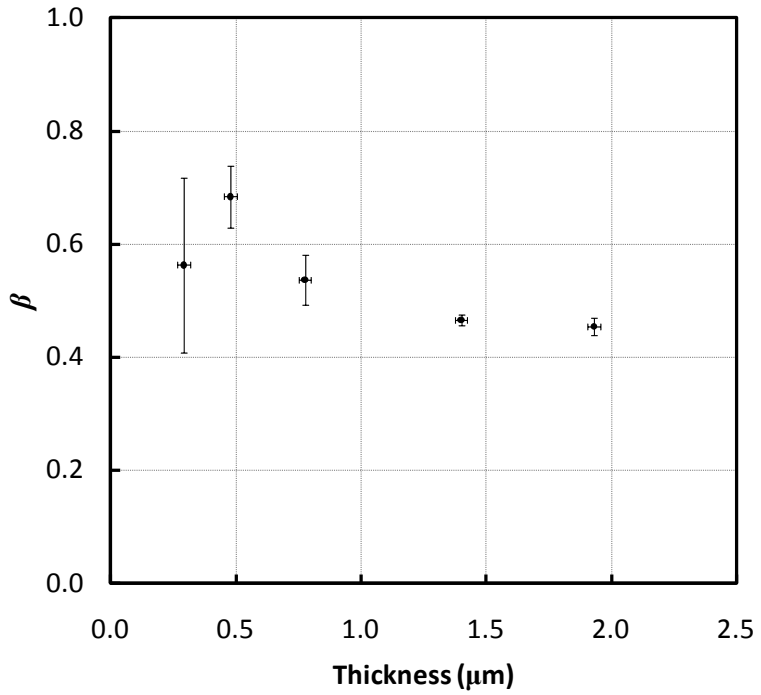


**Figure 6-11: The dependence of the stretching exponent $\beta$ on sample thickness for a-$As_2Se_3$.**

The results obtained by measurement of various sample thicknesses are not particularly illuminating as all of the results are well expected; however, the stretched exponential parameters are of use in validating previous results [91] and comparing trends with other researchers [16, 86]. The results can also be used to compare samples of similar thicknesses used for other studies within this work.

### 6.2.3 Effect of Doping

Studies were conducted on samples of a-$As_2Se_3$ doped with small quantities of iodine – approximately 0.1%. The effect of iodine on the structure of a chalcogenide is not known; however, iodine is a halogen and forms a single bond which should reduce the average coordination number and make it easier for structural rearrangements in the material. Adding iodine also affects the charge transport in a-$As_2Se_3$; specifically, an increase in the hole mobility has been observed [94]. An increase in the hole mobility may cause a hole to be more likely to diffuse away from an absorbing micro-volume when an electron-hole pair separate. Overall this would lead to a decrease in the rate ($1/\tau$). All samples measured in this section were prepared by thermal evaporation.

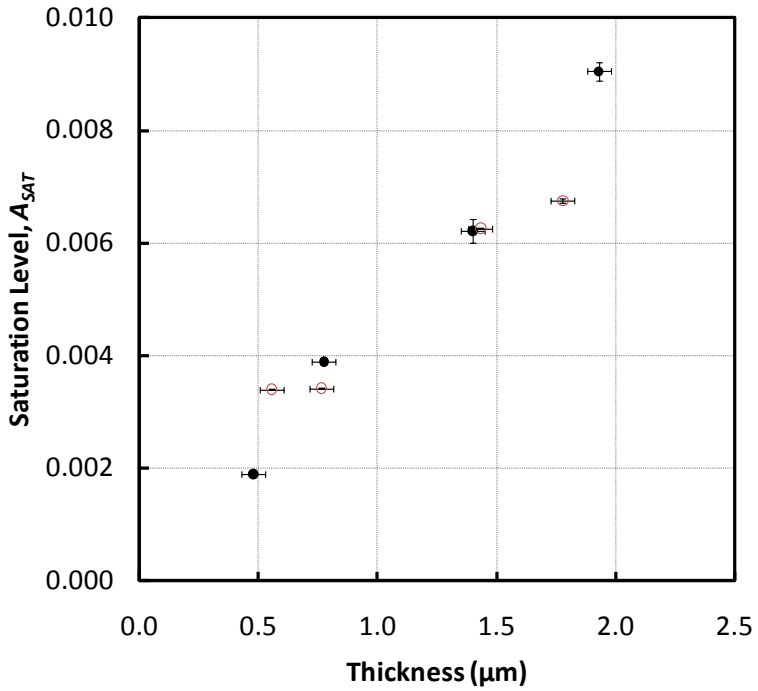


**Figure 6-12:** **PDi saturation level ($A_{sat}$) as a function of film thickness for a-$As_2Se_3$ (closed circles) and a-$As_2Se_3$ doped with 0.1% iodine (open circles).**

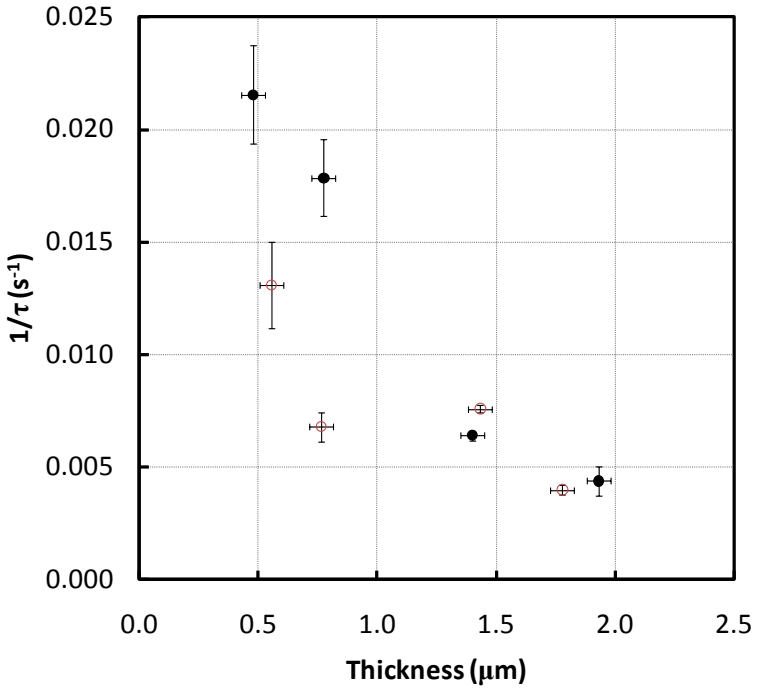


**Figure 6-13:** **The dependence of the rate ($1/\tau$) for inducing PDi on sample thickness for a-$As_2Se_3$ (closed circles) and a-$As_2Se_3$ doped with 0.1% iodine (open circles).**

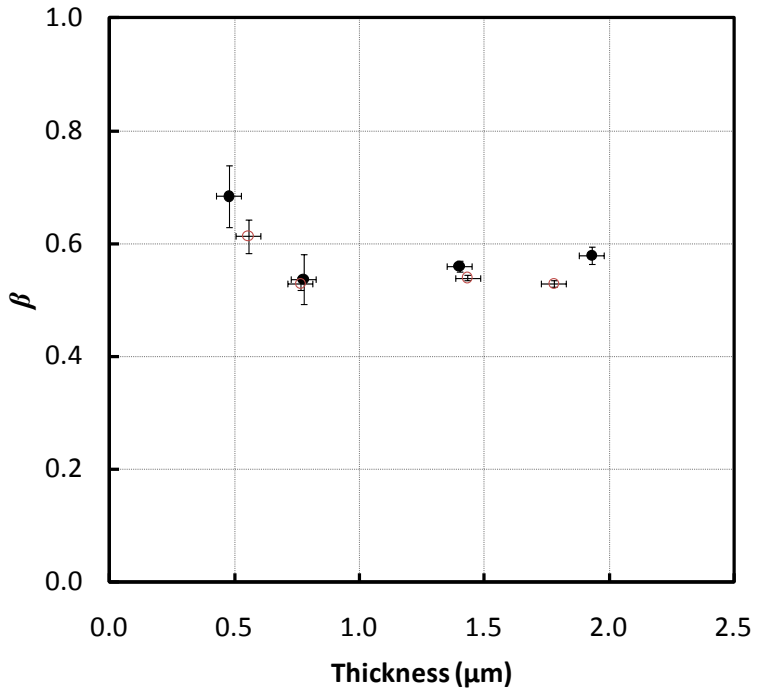


**Figure 6-14: The dependence of the stretching exponent $\beta$ on sample thickness for a-$As_2Se_3$ (closed circles) and a-$As_2Se_3$ doped with 0.1% iodine (open circles).**

A comparison of PDi kinetics for various thicknesses of a-$As_2Se_3$ with those samples doped with iodine are shown in Figure 6-12, Figure 6-13, and Figure 6-14. The results in Figure 6-13 for the rate show that adding 0.1% iodine decreased the rate for two of the four samples. This would seem to validate theory for most of the samples; however, it is not known why the abnormality of the one sample exists. The results for the other two fitting parameters were shown for completeness and do in fact demonstrate that adding 0.1% iodine has no substantial effect on $A_{sat}$ or $\beta$.

## 6.2.4 Electric Field Dependence

In this section the application of a DC electric field to samples of a-$As_2Se_3$ and its effects on the PDi are discussed. Samples with transparent electrodes allow a DC electric field to be applied while the pump beam induces dichroism. In this case the field is referred to as transverse with respect to the inducing beam propagation direction. Previous studies have been conducted on chalcogenide glasses where the electric field is both transverse

and longitudinal to the inducing beam [16, 93]. The samples used for the DC electric field dependence measurements were all prepared by sputtering.

Samples consisted of a thin film (0.21 μm) of sputtered a-$As_2Se_3$ preceded and followed by a thin layer of transparent Indium-Tin-Oxide (ITO). Small wires were bonded to both layers of ITO allowing for the application of a voltage from 0 – 10 V/μm. Increasing the field strength any higher would not be advantageous as it approaches the breakdown strength of a-$As_2Se_3$. Exceeding the breakdown strength of the material could possibly compromise the sample and lead to ambiguous measurement results.

The results of PDi measurements at various field strengths are shown in Figure 6-15, Figure 6-16, and Figure 6-17.

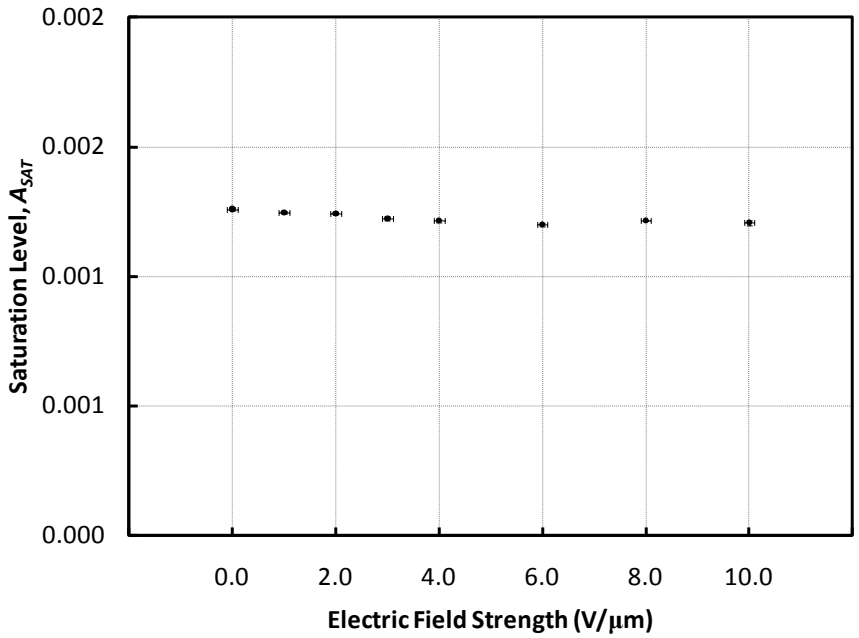


**Figure 6-15: PDi saturation level ($A_{sat}$) as a function of electric field strength for a 0.21 μm film of a-$As_2Se_3$.**

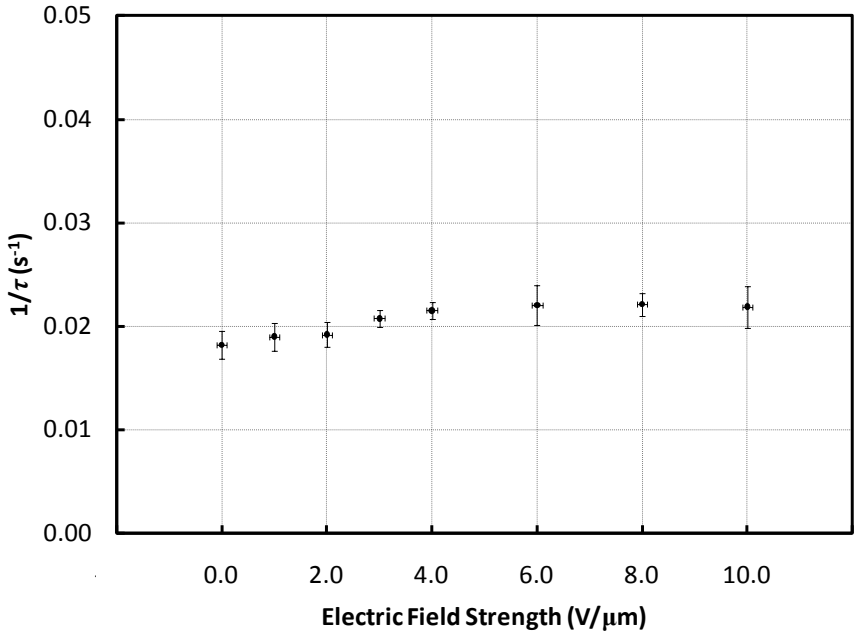


**Figure 6-16: The dependence of the rate (1/τ) for inducing PDi as a function of electric field strength for a 0.21 µm film of a-$As_2Se_3$.**

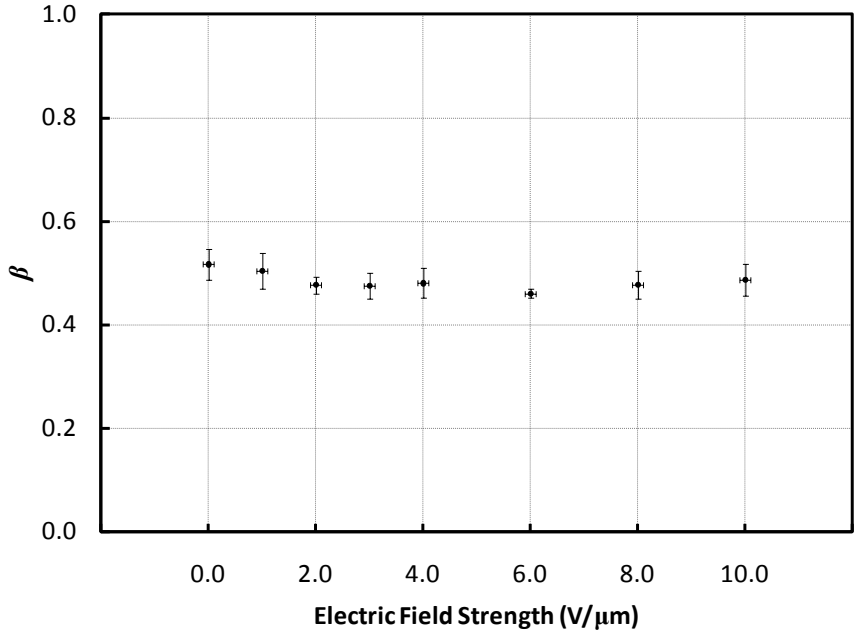


**Figure 6-17: The dependence of the stretching exponent $\beta$ as a function of electric field strength for a 0.21 µm film of a-$As_2Se_3$.**

In the model put forth by Fritzsche, polarized light is only effective in inducing anisotropy if the recombination of the electron and hole takes place in the same micro-

volume responsible for absorbing the photon. If the electron or hole recombines in a different micro-volume then the resulting changes to the structure are uncorrelated with the particular structure that preferentially absorbs the incident polarization. A sufficiently strong electric field should break the exciton and drift either electron or hole or both away from the absorbing site and hence reduce the efficiency of producing the dichroism. We expect $\tau$ to increase with electric field and perhaps $\beta$ to decrease stretching out the curve. Our results do not agree with expectations. Other studies have also demonstrated no detectable influence of a transverse electric field on PDi [16, 93]; meanwhile, the same studies have shown an acceleration in PD with the application of a longitudinal field. Research would suggest that a modification to the model is necessary to fully account for the lack of dependence on the field.

## 6.3 Summary

The kinetics of PDi were measured in as-deposited films of a-$As_2Se_3$. Measurements were made with various inducing beam intensities, for various sample thicknesses, during the application of a transverse DC electric field, and for samples doped with small quantities of iodine (0.1%). Results were placed within currently accepted theoretical models for amorphous materials, and compared to previously reported results.

The time dependence of induced dichroism was fit to an exponential function of the form $\exp(-(t/\tau)^{\beta})$. Of interest from the fitting function are three parameters: the saturation level, time constant, and stretching exponent. The first series of results presented those parameters as a function of inducing beam intensity, and the second as a function of thickness. It was demonstrated that $A_{sat}$ does not vary with $I_{pump}$, but varies linearly with sample thickness. Meanhwile, the rate ($1/\tau$) depends linearly on $I_{pump}$ and decreases with increasing sample thickness. Lastly, the stretching exponent $\beta$ was found to be relatively independent of both $I_{pump}$ and sample thickness. These results are in agreement with the theoretical model put forth by Fritzsche [85] and results reported by other researchers [16, 86, 93].

The PDi was measured in samples doped with small quantities of iodine (0.1%). Results indicated that the addition of iodine had no effect on either $A_{sat}$ or $\beta$; meanwhile, the rate decreased substantially in several samples. This appears to agree with theoretical findings in [94]; however, as of yet there is no other research to compare with.

The last set of results focused on the fitting parameters when PDi is measured in the presence of a transverse electric field. The field was applied across the sample transverse to the direction of the inducing beam. The theoretical model put forth by Fritzsche [84] suggests that $\tau$ should increase, and perhaps $\beta$ should decrease, with increasing electric field strength. The results do not agree with theoretical predictions. In fact, the electric field was shown to have no effect on any of the three fitting parameters. Other researchers have published similar results [16] and have been unable to explain the disparity between experimental results and the theoretical predictions.

# Chapter 7 Conclusions and Recommendations

## 7.1 Introduction

The purpose of this research was to measure the kinetics of photoinduced dichroism in thin films of a-$As_2Se_3$. The time dependence of dichroism follows a stretched exponential of the form $\exp(-(t/\tau)^{\beta})$. Careful measurement of the PDi and extraction of the stretched exponential parameters can provide insight into microscopic models for photoinduced effects in Chalcogenide glasses.

## 7.2 Photoinduced Dichroism

Glasses are usually isotropic and lack any long-range order, resulting in a random averaging over all orientations of the possible microstructure. The isotropic nature of a glass indicates that they should not exhibit either birefringence or dichroism; however, anisotropy can be induced in certain glasses by polarized light with a photon energy near the bandgap [12, 90, 95]. Upon irradiation the material will experience a shift in the absorption coefficient for light polarized in the same direction as the inducing beam – the result is dichroism. Accompanying what is referred to as photoinduced dichroism (PDi) is also photoinduced birefringence (PBi); however, it was only the former that was the subject of this work.

A useful framework for these photoinduced effects was put forward by Fritzsche [84]. In [85] it was noted that although a glass is initially overall isotropic, small regions called micro-volumes can be highly anisotropic. The effect is especially true for glasses composed of rings or chains of atoms. The micro-volumes can preferentially absorb light with a certain polarization causing a local structural change within the material. In the event that the resulting structure preferentially absorbs light with a different polarization we have what is referred to as dichroism. The process is a sort of optical pumping where the micro-volumes are altered toward states that weakly absorb the applied polarization. In order for the aforementioned process to occur three conditions must be met by the material: there must be sufficient freedom to allow the micro-volumes to change to a

different yet stable structure, the electron-hole recombination must occur within the absorbing micro-volume with a high probability, and a low-energy pathway must exist between stable configurations. Chalcogenide glasses fulfill these conditions, and the material which is the focus of this thesis, a-$As_2Se_3$ has been a paradigm for these effects.

The purpose of this thesis was to carefully measure the kinetics of photoinduced dichroism in a-$As_2Se_3$ and place those results within the framework of the currently accepted theoretical models. The time dependence of dichroism follows a stretched exponential of the form $\exp(-(t/\tau)^{\beta})$ [9, 16, 81]. In order to properly measure the dichroism we used an apparatus similar to those used by other researchers [90]. Depending on the measurement the HeNe laser or the 658 nm laser diode supplies the pump beam inducing the dichroism. In the case of the HeNe laser, the beam passes through a polarizer which can be rotated by 90°; however, for the laser diode the holder itself can be rotated so the polarizer is no longer included in the setup. The spot on the sample is approximately 5 mm in diameter and has a maximum intensity of 3.5 mW/mm$^2$ when using the 658 nm laser diode and 1.5 mW/mm$^2$ when using the HeNe laser. The probe beam used to monitor the PDi buildup within the sample was derived from an array of nineteen red LEDs with a peak wavelength of 635 nm. The use of LEDs eliminates the interference patterns that can occur when using lasers, and provides very close to unpolarized light. The probe beam passes through a polarizer rotating at a frequency $f$ and is then focused onto the sample producing a spot of about 1 mm in diameter. After the sample, the beam is focused onto a pin diode photodetector, and a lock-in amplifier extracts the $2f$ signal; the $2f$ signal is proportional to the dichroism of the sample. Any residual polarization of the probe beam (which also produces a $2f$ signal) is measured and removed during analysis. An experimental run consists of first photodarkening (PD) the sample to prevent any possible interference that may arise from scalar effects; then, exposing the sample to the pump beam while the $2f$ signal is recorded. Once the PDi saturates, the polarization of the pump beam is rotated by 90°, and the $2f$ signal is once again recorded until saturation of the PDi. The process is repeated four or more times.

To extract the kinetics of PDi from an experimental run the data were separated into individual measurement cycles, each consisting of data starting from zero anisotropy and proceeding to full saturation for one polarization state. For each cycle the time dependence of $A$ can be fit to a stretched exponential function of the form

$$A(t) = A_{sat} + (A_{init} - A_{sat})e^{-(t/\tau)^{\beta}} \tag{6.1}$$

where $A_{init} = A(0)$ (any change to the pump beam defines $t = 0$), and the three fitting parameters are $A_{sat} = A(\infty)$ the saturated anisotropy, $\tau$ the time constant, and $\beta$ the stretching exponent. Of interest from the fitting function are three parameters: the saturation level ($A_{sat}$), time constant ($\tau$), and stretching exponent ($\beta$). Those three parameters represent the kinetics of PDi and this thesis presented them as a function of pump beam intensity, sample thickness, and external electric field. Results were also obtained for those samples doped with small quantities of iodine (0.1%).

The first series of results presented the fitting parameters as a function of inducing beam intensity, and the second as a function of thickness. It was demonstrated that $A_{\text{sat}}$ does not vary with $I_{\text{pump}}$, but varies linearly with sample thickness. The maximum relative change in the absorption coefficient was found to be approximately $2.5 \times 10^{-3}$. Such a small change may limit the ability of this material to be used in commercial applications. Meanhwile, the rate ($1/\tau$) depends linearly on $I_{\text{pump}}$ and decreases with increasing sample thickness. Lastly, the stretching exponent $\beta$ was found to be relatively independent of both $I_{\text{pump}}$ and sample thickness. These results are in agreement with the theoretical model put forth by Fritzsche [85] and results reported by other researchers [16, 86, 93]. The PDi was measured in samples doped with small quantities of iodine (0.1%). Results indicated that the addition of iodine had no effect on either $A_{\text{sat}}$ or $\beta$; meanwhile, the rate decreased substantially in several samples. This appears to agree with theoretical findings in [94]; however, as of yet there is no other research to compare with. The last set of results focused on the fitting parameters when PDi is measured in the presence of a transverse electric field. The field was applied across the sample transverse to the direction of the inducing beam. The theoretical model put forth by Fritzsche [84] suggests that $\tau$ should increase, and perhaps $\beta$ should decrease, with increasing electric

field strength. The results do not agree with theoretical predictions. In fact, the electric field was shown to have no effect on any of the three fitting parameters. Other researchers have published similar results [16] and have been unable to explain the disparity between experimental results and the theoretical predictions.

## 7.3 Suggestions for Future Work

Careful measurement of the PDi and extraction of the stretched exponential parameters can provide insight into microscopic models for photoinduced effects in chalcogenide glasses. Any model must account for the stretched exponential time dependence and why $\beta$ is in the range 0.5 to 0.65. Further investigation of the dependence of the parameter $\beta$ under various conditions will better describe its functional dependencies. The results showed no effect of an external electric field; measurements at larger fields, or perhaps with other electrodes, will test the importance of geminate recombination for photo-induced dichroism.

# References


1 N.A. Goryunova and B.T. Kolomiets, Journal of Technical Physics (USSR), Vol. 25, pg. 984, 1955.

2 http://www.xerox.com/innovation/Storyofxerography.pdf

3 S.O. Kasap and J.A. Rowlands, "Direct-conversion Flat-panel X-ray Image Sensors for Digital Radiography", Proceedings of the IEEE, Vol. 90, pp 591 − 604, 2002.

4 L.C. Kimerling, "Silicon Microphotonics," Applied Surface Science, Vol. 159 160, pp 8 − 13, 2000.

5 R.G. DeCorby, M.M. Pai, H.T. Nguyen, P.K. Dwivedi, T.J. Clement, C.J. Haugen, J.N. McMullin, and S.O. Kasap, "High Index Contrast Waveguides in Chalcogenide Glass and Polymer," IEEE Journal of Selected Topics in Quantum Electronics, Vol. 11, no. 2, pp 539 – 546, 2005.

6 J.F. Viens, C. Meneghini, A. Villeneuve, T.V. Galstian, E.J. Knystautas, M.A. Duguay, K.A. Richardson, and T. Cardinal, "Fabrication and Characterization of Integrated Optical Waveguides in Sulfide Chalcogenide Glasses," Journal of Lightwave Technology, Vol. 17, no. 7, pp 1184 – 1191, 1999.

7 H. Hisakuni, K. Shiramine, and K. Tanaka, "Photoinduced Bragg Reflector in $As_2S_3$ Glass," Applied Physics Letter, Vol. 64, no. 14, pp 1771 – 1773, 1994.

8 V. Lyubin, M. Kelbanov, A. Feigel, and B. Sfez, "Films of Chalcogenide glassy Semiconductors: New Phenomena and New Applications," Thin Films, Vol. 459, pp 183 – 186, 2004.

9 J.P. De Neufville, S.C. Moss and S.R. Ovshinsky, "Photostructural Transformations in Amorphous $As_2Se_3$ and $As_2S_3$ Films," Journal of Non-Crystalline Solids, Vol. 13, no. 2, pp 191 – 223, 1974.

10 A.V. Kolobov, "Photo-Induced Metastability in Amorphous Semiconductors" Wiley-VCH GmbH & Co. KGaA, Weinheim, Copyright 2003.

11 P. Krecmer, A.M. Moulin, R.J. Stephenson, T. Rayment, M.E. Welland, and S.R. Elliott, "Reversible Nanocontraction and Dilatation in a Solid Induced by Polarized Light," Science, Vol. 277, pp 1799 – 1802, 1997.

12 V.G. Zhdanov, B.T. Kolomiets, V.M. Lyubin, and V.K. Malinovbskii, "Photoinduced Optical Anisotropy in Chalcogenide Vitreous Semiconducting Films," Physica Status Solidi A, Vol. 52, pp 621 – 626, 1979.

13 D. DeForrest, R.E. Johanson, and S.O. Kasap, "Photoinduced Dichroism in Thin Films of Amorphous $As_2Se_3$," IEEE CCECE 2005, pp 1493 – 1495, 2005.

14 S.O. Kasap, Optoelectronics chapter in "The Encyclopedia of Optics" Wiley-VCH, 2003.

15 S. Ramachandran and S.G. Bishop, "Low Loss Photoinduced Waveguides on Rapid Thermally Annealed Films of Chalcogenide Glasses," Applied Physics Letter, Vol. 74, no. 1, pp 13 – 15, 1999.

16 P. Hertogen, "Photoinduced Anisotropies in Chalcogenide Semiconductors," Ph. D. Thesis, Katholieke Universiteit Leuven, Copyright 2000.

17 N.F. Mott and E.A. Davis, "Electronic Processes in Non-crystalline Materials 2nd Edition," Oxford University Press, Copyright 1979.

18 S.R. Elliott, "Physics of Amorphous Materials," Longman Scientific & Technical, Copublished in the US with John Wiley & Sons, Copyright 1983.

19 W.H. Zachariasen, "The Atomic Arrangement in Glass," Journal of American Chemical Society, Vol. 54, no. 10, pp. 3841 – 3851, 1932.

20 S.O. Kasap, "Principle of Electronic Materials and Devices, 2nd Edition,"McGraw-Hill, Copyright 2002.

21 P.W. Anderson, "Absence of Diffusion in Certain Random Lattices," Physical Review, Vol. 109, pp. 1492 – 1505, 1958.

22 N.F. Mott, "Electrons in Disordered Structures," Advances in Physics, Vol. 16, pp 49 − 145, 1967.

23 M.H Cohen, H. Fritzsche, and S.R. Ovshinski, "Simple Band Model for Amorphous Semiconductor Alloys", Physical Review Letters, Vol. 22, no. 20, pp. 1065-1068, 1969.

24 J.M. Marshall and A.E. Owen, "Drift Mobility Studies in Vitreous Arsenic Triselenide", Philosophical Magazine, Vol. 24, pp. 1281-1290, 1971.

25 J. Tauc , "Amorphous and Liquid Semiconductors," Plenum Press, Copyright 1974.

26 M. Kastner, "Bonding Bands, Lone-Pair Bands, and Impurity States in Chalcogenide Semiconductors," Physical Review Letters, Vol. 28, no. 6, pp. 355 – 357, 1972.

27 A. Madan and M.P. Shaw, “The Physics and Applications of Amorphous Semiconductors,” Academic Press, Inc. Copyright 1988.

28 K. Tanaka, E. Maruyama, T. Shimada, and H. Okamoto, “Amorphous Silicon,” John Wily & Sons Ltd. Copyright 1999.

29 H. Tichá, L. Tichý, and V. Smrcka, “The Temperature Dependence of the Optical Gap in Quasibinary Chalcogenide Glasses and their Far Infrared Spectra,” Materials Letters, Vol. 20, no. 3 – 4, pp. 189 – 193, 1994.

30 K. Weiser and M. H. Brodsky, “DC Conductivity, Optical Absorption, and Photoconductivity of Amorphous Arsenic Telluride Films,” Physical Review B, Vol. 1, no. 2, pp. 791 – 799, 1970.

31 N.F. Mott, “Conduction in Non-crystalline Materials III. Localized States in a Pseudogap and Near Extremities of Conduction and Valence Bands,” Philosophical Magazine, Vol.19, Series 5, pp 835 − 852, 1969.

32 P.W. Anderson, “Model for the Electronic Structure of Amorphous Semiconductors,” Physical Review Letters, Vol. 34, no. 15, pp 953 – 955, 1975.

33 R.A. Street and N.F Mott, “States in the Gap in Glassy Semiconductors,” Physical Review Letters, Vol. 35, no. 19, pp 1293 – 1295, 1975.

34 M. Kastner, D. Adler, and H. Fritzsche, “Valence-Alternation Model for Localized Gap States in Lone-Pair Semiconductors,” Physical Review Letters, Vol. 37, no. 22, pp 1504 – 1507, 1976.

35 A.V. Kolobov, M. Kondo, H. Oyanagi, R. Durny, A. Matsuda, and K. Tanaka, “Experimental Evidence for Negative Correlation Energy and Valence Alternation in Amorphous Selenium,” Physical Review B, Vol. 56, no. 2, pp R485 – R488, 1997.

36 L. Dong, R. W. Smith, and D. J. Srolovitz, “A Two-dimensional Molecular Dynamics Simulation of Thin Film Growth by Oblique Deposition,” Journal of Applied Physics, Vol. 80, no. 10, pp. 5682 – 5690, 1996.

37 K. Starbova, J. Dikova, and N. Starbov, “Structure Related Properties of Obliquely Deposited Amorphous a-As2S3 Thin Films,” Journal of Non-crystalline Solids, Vol. 210, no. 2 – 3, pp. 261 – 266, 1997.

38 K. Shimakawa, A. Kolobov and S.R. Elliott, “Photoinduced Effects and Metastability in Amorphous Semiconductors and Insulators,” Advances in Physics, Vol. 44, no. 6, pp 475 – 588, 1995.

39 V.K. Tikhomirov and S.R. Elliot, “Model for Photoinduced Anisotropy and Its Dark Relaxation in Chalcogenide Glasses,” Physical Review B, Vol. 51, no. 8, pp 5539 – 5541, 1995.

40 V. M. Lyubin and V. K. Tikhomirov, “Photodarkening and Photoinduced Anisotropy in Chalcogenide Vitreous Semiconductor Films,” Journal of Non-Crystalline Solids, Vol. 114, pp 133 − 135, 1989.

41 V.M. Lyubin and V.K. Tikhomirov, “Spectra of Natural and Photoinduced Linear Dichroism in Chalcogenide Glasses,” Journal of Non-Crystalline Solids, Vol. 171, pp 87 – 93, 1994.

42 K. Kimura, K. Murayama and T. Ninomiya, “Change in Optical Anisotropy of Localized States Associated with Reversible Photostructural Change in a-$As_2S_3$ Films,” Journal of Non-Crystalline Solids, Vol. 77 & 78, pp 1203 − 1206, 1985.

43 J.S. Berkes, S.W. Ing, Jr. and W. J. Hillegas, “Photodecomposition of Amorphous $As_2Se_3$ and $As_2S_3$,” Journal of Applied Physics, Vol. 42, no. 12, pp 4908 – 4916, 1971.

44 L. Tichy, H. Ticha, P. Nagels, and R. Callaerts, “Photoinduced optical changes in amorphous Se and Ge-Se films,” Journal of Non-Crystalline Solids, Vol. 240, pp. 177-181, 1998.

45 S. Rajagopalan, B. Singh, P. K. Bhat, D. K. Pandya, and K. L. Chopra, “Photoinduced optical effects in obliquely deposited amorphous Se-Ge films,” Journal of Applied Physics, Vol. 50, no. 1, pp. 489 – 492, 1979.

46 M. Okuda, T. T. Nang, and T. Matsushita, “Photo-induced absorption changes in selenium-based chalcogenide glass films,” Thin Solid Films, Vol. 58, no. 2, pp. 403 – 406, 1979.

47 E. Márquez, A. M. Bernal-Oliva, J. M. González-Leal, T. Prieto-Alcón, and R. Jiménez-Garay, “On the irreversible photo-bleaching phenomenon in obliquely evaporated $GeS_2$ glass films,” Journal of Non-Crystalline Solids, Vol. 222, pp. 250 – 257, 1997.

48 C.Y. Yang, M.A. Paesler and D.E. Sayers, “Measurement of Local Structural Configurations Associated with Reversible Photostructural Changes in Arsenic Trisulfide Films,” Physical Review B, Vol. 36, pp 9160 – 9167, 1987.

49 K. Tanaka, “Mechanisms of Photodarkening in Amorphous Chalcogenides,” Journal of Non-Crystalline Solids, Vol. 59 & 60, pp 925 − 928, 1983.

50 V. M. Lyubin and V. K. Tikhomirov, “Novel photo-induced effects in chalcogenide glasses,” Journal of Non-Crystalline Solids, Vol. 135, pp. 37 – 48, 1991.

51 K. Oe, Y. Toyoshima, and H. Nagai, “A reversible optical transistion in Se-Ge and P-Se-Ge glasses,” Journal of Non-Crystalline Solids, Vol. 20, pp. 405 – 411, 1976.

52 A.V. Kolobov, Yu.P. Kostikov, S.S.Lantratova, and V.M. Lyubin, “Photoelectron Spectroscopic Investigation of Photostructural Transformations in Glassy Chalcogenide Semiconductor Films,” Soviet Physics - Solid State, Vol. 33, no. 3, pp 444 – 447, 1991.

53 R.A. Street, J. Kakalios, C.C. Tsai and T.M. Hayes, “Thermal-equilibrium Processes in Amorphous Silicon,” Physical Review B, Vol. 35, pp 1316− 1333, 1987.

54 J. Feinleib, J. deNeufville, S.C. Moss and S.R. Ovshinsky, “Rapid Reversible Light-Induced Crystallization of Amorphous Semiconductors,” Applied Physics Letters, Vol. 18, pp 254 - 257, 1971.

55 H. Hamanaka, Japanese Journal of Applied Physics, “Reversible Phase Transformations in the Selenium Films Due to Laser Light Irradiation,” Vol. 13, pp 1171 - 1172, 1974.

56 J. E. Griffiths, G. P. Espinosa, J. P. Remeika, and J. C. Phillips, “Reversible reconstruction and crystallization of GeSe2 glass,” Solid State Communications, Vol. 40, no. 12, pp. 1077 – 1080, 1981.

57 S.R. Elliott and A.V. Kolobov, “Athermal Light-Induced Vitrification of $As_{50}Se_{50}$ Films,” Journal of Non-Crystalline Solids, Vol. 128, pp 216 – 220, 1991.

58 J. E. Griffiths, G. P. Espinosa, J. P. Remeika, and J. C. Phillips, “Reversible quasicrystallization in $GeSe_2$ glass,” Physical Review B, Vol. 25, no. 2, pp. 1272 – 1286, 1982.

59 J. E. Griffiths, G. P. Espinosa, J. C. Phillips, and J. P. Remeika, “Raman spectra and athermal laser annealing of $Ge(S_xSe_{1-x})_2$ glasses,” Physical Review B, Vol. 28, no. 8, pp. 4444 – 4453, 1983.

60 E. Haro, Z. S. Xu, J. F. Morhange, M. Balkanski, G. P. Espinosa, and J. C. Phillips, “Laser-induced glass-crystallization phenomena of $GeSe_2$ investigated by light scattering,” Physical Review B, Vol. 32, no. 2, pp. 969 – 979, 1985.

61 S. Sugai, “Stochastic random network model in Ge and Si chalcogenide glasses,” Physical Review B, Vol. 35, no. 3, pp. 1345 – 1361, 1987.

62 S. Sugai, “Two-directional photinduced crystallization in GeSe2 and SiSe2 glasses,” Physical Review Letters, Vol. 57, no. 4, pp. 456 – 459, 1986.

63 V.K. Tikhomirov, P. Hertogen, C. Glorieux, and G.J. Adriaenssens, “Oriented Crystallization of Amorphous Se Induced by Linearly Polarized Light,” Physica Status Solidi A, Vol. 162, no. 2, pp. R1 – R2, 1997.

64 V.K. Tikhomirov, P. Hertogen, G.J. Adriaenssens, C. Glorieux, and R. Ottenburgs, “Anisotropic laser crystallization of a-Se,” Journal of Non-Crystalline Solids, Vol. 227-230, pp. 732 – 738, 1998.

65 Y. Kuzukawa, A. Ganjoo, K. Shimakawa, and Y. Ikeda, “Photo-induced structural changes in obliquely deposited arsenic-based amorphous chalcogenides: a model for photostructural changes,” Philosophical Magazine B, Vol. 79, no. 2, pp. 249 – 256(8), 1999.

66 S. Rajagopalan, K.S. Harshavardhan, L.K. Malhorta, and K.L. Chopra, “Photo-optical changes in Ge-chalcogenide films,” Journal of Non-Crystalline Solids, Vol. 50, pp. 29 – 38, 1982.

67 H. Hamanaka, K. Tanaka, and S. Iizima, “Reversible photostructural change in melt-quenched $As_2S_3$ glass,” Solid State Communications, Vol. 23, no. 1, pp. 63 – 65, 1977.

68 A. Ganjoo, Y. Ikeda, and K. Shimakawa, “*In situ* photoexpansion measurements of amorphous $As_2S_3$ films: Role of photocarriers,” Applied Physics Letters, Vol. 74, no. 15, pp. 2119 – 2121, 1999.

69 H. Hisakuni and K. Tanaka, “Giant photoexpansion in $As_2S_3$ glass,” Applied Physics Letters, Vol. 65, no. 23, pp. 2925 – 2927,1994.

70 K. Tanaka and H. Hisakuni, “Photoinduced phenomena in $As_2S_3$ glass under subbandgap excitation,” Journal of Non-Crystalline Solids, Vol. 198-200, pp. 714 – 718, 1996.

71 H. Hamanaka, K. Tanaka, and S. Iizima, “Reversible photostructural change in melt-quenched $GeS_2$ glass,” Solid State Communications, Vol. 33, no. 3, pp. 355 – 357, 1980.

72 P. Krecmer, A. M. Moulin, R. J. Stephenson, T. Rayment, M. E. Welland, and S. R. Elliott, “Reversible noncontraction and dilation in a solid induced by polarized light,” Science, Vol. 277, pp. 1799 – 1802, 1997.

73 H. Hisakuni and K. Tanaka, “Optical microfabrication of chalcogenide glasses,” Science, Vol. 270, pp. 974 – 975, 1995.

74 K. Tanaka, “Physics and applications of photodoping in chalcogenide glass,” Journal of Non-Crystalline Solids, Vol. 137&138, pp. 1021 – 1026, 1991.

75 S. R. Elliott, “Photodissolution fo metals in chalcogenide glasses: a unified mechanism,” Journal of Non-Crystalline Solids, Vol. 137&138, pp. 1031 – 1034, 1991.

76 A. V. Kolobov, “Photo-induced atomic processes in vitreous chalcogenides,” Journal of Non-Crystalline Solids, Vol. 164-166, pp. 1159 – 1164, 1993.

77 T. Kósa and I. Jánossy, “Kinetics of Optical Reorientation in Amorphous $GeSe_2$ Films,” Philosophical Magazine B, Vol. 64, no. 3, pp 355 – 366, 1991.

78 V.M. Lyubin and V.K. Tikhomirov, “Photoinduced Gyrotropy and Photoinduced Light Scattering in the Chalcogenide Glass $As_2S_3$,” JETP Letters, Vol. 52, no. 2, pp 78 – 81, 1990.

79 V.M. Lyubin and V.K. Tikhomirov, “Photoinduced Dichroism in Glassy Chalcogenide Semiconductor Films,” Soviet Physics Solid State, Vol. 32, no. 6, pp 1069 – 1074, 1990.

80 S.R. Elliott and V.K. Tikhomirov, “Vectoral and Scalar Photoinduced Effects in Chalcogenide Glasses,” Journal of Non-Crystalline Solids, Vol. 198 – 200, pp 669 − 674, 1996.

81 V. K. Tikhomirov, G. J. Adriaenssens and S. R. Elliott, “Temperature Dependence of the Photoinduced Anisotropy in Chalcogenide Glasses: Activation Energies and Their Interpretation,” Physical Review B, Vol. 55, no. 2, pp R660 − R663, 1997.

82 H. Fritzsche, “The Origin of Reversible and Irreversible Photostructural Changes in Chalcogenide Glasses,” Philosophical Magazine B, Vol. 68, no. 4, pp 561 – 572, 1993.

83 H. Fritzsche, “The Origin of Photo-Induced Optical Anisotropies in Chalcogenide Glasses,” Journal of Non-Crystalline Solids, Vol. 164 – 166, pp 1169 – 1172, 1993.

84 H. Fritzsche, “Optical Anisotropies in Chalcogenide Glasses Induced by Band-Gap Light,” Physical Review B, Vol. 52, no. 22, pp 15845 – 15861, 1995.

85 V.K. Tikhomirov and S.R. Elliott, “Metastable Optical Anisotropy in Chalcogenide Glasses Induced by Unpolarized Light,” Physical Review B, Vol. 49, no. 24, pp 17476 – 17479, 1994.

86 D. DeForrest, “Photoinduced Dichroism in Amorphous As2Se3 Thin Film,” M. Sc. Thesis, University of Saskatchewan, Copyright 2005.

87 W.C. Tan, “Optical Properties of Amorphous Selenium Films,” M. Sc. Thesis, University of Saskatchewan, Copyright 2006.

88 S.O. Kasap, “Optoelectronics and Photonics Principles and Practices,” Prentice-Hall, Copyright 2001.

89 A.C. van Popta, R.G. DeCorby, C.J. Haugen, T. Robinson, J.N. McMullin, D. Tonchev, and S.O. Kasap, “Photoinduced Refractive Index Change in As2Se3 by 633nm Illumination,” Optics Express, Vol. 10, no. 15, pp. 639 – 644, 2002.

90 K. Tanaka, Chapter 4 in “Handbook of Advanced Electronics and Photonic Materials and Devices,” Vol. 5, ed. by H.S. Nalwa, Academic Press, 2001.

91 Robert E. Johanson, Matthew Kowalyshen, Daniel DeForrest, K. Shimakawa and S. O. Kasap, “The Kinetics of Photo-induced Dichroism in Thin Films of Amorphous Arsenic Triselenide,” Journal of Materials Science: Materials in Electronics, Vol. 18, no. 1, pp. 127 – 130, 2007.

92 J. Hajtó, I. Jánossy and G. Forgás, “Laser-induced Optical Anisotropy in Self-supporting Amorphous GeSe2 Films,” Journal of Physics C: Solid State Physics, Vol. 15, pp. 6293 – 6303, 1982.

93 P. Hertogen, V.K. Tikhomirov, G. J. Adriaenssens, “Photoinduced Dichroism in Chalcogenides: Influence of Temperature and Light Intensity,” Journal of Non-Crystalline Solids, Vol. 256 – 257, pp. 343 – 347, 1999.

94 G. Pfister, A.R. Melnyk, M.E. Scharfe, “Enhancemnet of Hole Drift Velocity in Amorphous $As_2Se_3$ by Iodine Doping,” Solid State Communications, Vol. 21, pp. 907 – 910, 1977.

95 V.M. Lyubin, M.L. Klebanov, Chapter 6 in “Photo-induced Metastability in Amorphous Semiconductors,” ed. by A.V. Kolobov, Wiley-VCH Verlag & Co., 2003.